NOVA SCHOOL OF SCIENCE & TECHNOLOGY

DEPARTMENT OF CHEMISTRY

Maria Teresa Falcão Barbosa Pereira Rosa

BSc in Biochemistry

Calcium-Stabilised Zirconia Nanoparticles for Tissue Engineering Applications

MASTER IN Biotechnology

NOVA University Lisbon

September, 2024

NOVA SCHOOL OF SCIENCE & TECHNOLOGY

DEPARTMENT OF CHEMISTRY

Calcium-Stabilised Zirconia Nanoparticles for Tissue Engineering Applications

Maria Teresa Falcão Barbosa Pereira Rosa

BSc in Biochemistry

Adviser: Henrique Vazão de Almeida
Researcher at CENIMAT|i3N, FCT NOVA

Co-advisers: Daniela Nunes Gomes
Assistant Professor, FCT NOVA

Examination Committee:

Chair: Maria Filomena Andrade de Freitas,
Auxiliar professor, FCT-NOVA

Rapporteurs: Paula Isabel Pereira Soares,
Principal researcher at CENIMAT, FCT-NOVA
Name of another rapporteur,
Assistant Professor, Another University

Adviser: Henrique Vazão de Almeida
Researcher at CENIMAT|i3N, FCT NOVA

Members: Daniela Nunes Gomes
Assistant Professor, FCT NOVA

MASTER IN BIOTECNHOLOGY

NOVA University Lisbon
September, 2024

Calcium-Stabilised Zirconia Nanoparticles for Tissue Engineering Applications

Funding: This work was financed by national funds from FCT - Fundação para a Ciência e a Tecnologia, I.P., in the scope of the projects LA/P/0037/2020, UIDP/50025/2020 and UIDB/50025/2020 of the Associate Laboratory Institute of Nanostructures, Nanomodelling and Nanofabrication – i3N)

Para os meus pais.

Acknowledgements

Primeiramente, gostaria de expressar os meus agradecimentos aos meus orientadores Dr. Henrique Almeida e Drª Daniela Gomes por me terem aceite no CENIMAT|i3N, por toda ajuda, disponibilidade, confiança depositada e, acima de tudo, pela constante esperança e positividade que me inspirou a desenvolver da melhor forma este projeto.

Em seguida, gostaria de agradecer à Drª Isabel Barahona pelo acesso às instalações laboratoriais da Egas Moniz School of Health and Science, assim como, todo o conhecimento transmitido e pela constante disponibilidade em tudo o que fosse preciso. Aproveito de igual forma para agradecer ao Dr. João Carlos Silva, ao Frederico e à Mafalda pelo acesso ao iBB, por toda a prontidão e importante partilha de ideias. Aproveito também para agradecer ao Carlos por toda a paciência na aquisição de imagens e por todas as dicas preciosas.

Quero também agradecer às futuras doutoras Leonor e Maria por toda a compreensão e conhecimentos transmitidos, mas acima de tudo por me ajudarem e guiarem na direção correta quando me sentia mais perdida, a vossa ajuda e acolhimento fez toda a diferença. Não podia também deixar de agradecer à minha colega de bancada Carolina por toda a companhia e ajuda mútua desde o começo, assim como por todos os desabafos e gargalhadas, mas também por me mostrar que existem sempre soluções.

Às minhas amigas do mestrado, Inês e Madalena obrigada por todos os momentos ao longo desta jornada, por estarem sempre tão perdidas como eu, por terem tornado os meus dias mais divertidos e pela companhia em momentos de stress. Sem a vossa amizade e ajuda teria sido impossível.

Às grandes amigas que a licenciatura em Bioquímica me deu, Madalena, Rita, Maria, Matilde e Mariana. É notável como sempre nos apoiamos. Obrigada por termos crescido juntas nestes anos e por estarem sempre lá. Obrigada por todas as conversas tardias, pelos ataques de riso na biblioteca e por todas as férias memoráveis. Todos estes (e outros) são momentos que levo comigo e que guardo com muito carinho.

Aos meus amigos Tomás, Maria, Lúcia, Bia, Sofia e Diogo, devo-vos um enorme agradecimento pela constante presença e companhia. Obrigada por todos os planos de última hora, por ouvirem sempre as minhas queixas, e sempre me puxarem para cima. Obrigada por serem quem são, tenho muita sorte em ter-vos na minha vida.

Às minhas melhores amigas Raquel e Inês, obrigada pelo privilégio de partilhar a vida convosco há tantos anos, pela presença em todas as etapas mais importantes do meu percurso e por me darem sempre força e incentivarem que seria capaz de chegar onde quisesse.

Por fim, não podia deixar de agradecer à minha família em especial aos meus pais, avó e irmão por nunca me proporcionarem nada menos que o melhor. Obrigada por toda a paciência e compreensão nos piores dias, em especial neste último ano.

A todos, o meu mais sincero e genuíno obrigada!

Abstract

Effective regeneration of osteochondral and periodontal bone tissues remains challenging. Tissue engineering (TE) strives to develop strategies for this regeneration, often using natural polymers such as alginate. Nevertheless, the materials often lack the desired properties to correctly mimic bone tissues

It was reported for the first time the stabilisation of cubic zirconia (c-ZrO_2) nanoparticles using calcium (Ca) as a stabiliser. This was achieved through a one-step hydrothermal microwave process without any pre-or post-treatment, resulting in a more sustainable and cost-effective synthesis taking advantage of Ca abundance, biocompatibility and bioactivity. This phase stabilisation was demonstrated through Raman spectroscopy and scanning transmission electron microscopy (STEM) analysis. Moreover, the c-ZrO_2 nanoparticles presented an average size of 6.24 ± 0.96 nm and an enhanced specific surface area. Nanotechnology approaches have proven useful in improving scaffold overall suitability in mechanically challenging environments. Thus, the c-ZrO_2 nanoparticles were incorporated into alginate scaffolds by soaking. The obtained nanocomposite scaffolds presented no significant difference in terms of morphology and degradation when compared to pristine ones. The incorporation of the nanoparticles resulted in a significant decrease in the scaffolds' water uptake. Surprisingly, the nanoparticle-functionalised scaffolds exhibited only a slight increase in Young's modulus. Moreover, preliminary *in vitro* cytotoxicity results indicated that incorporating the c-ZrO_2 nanoparticles did not elicit any cytotoxic effect. Notably, after a 7-day cell culture period with human bone marrow mesenchymal stem cells (BM-MSCs), the group functionalised with c-ZrO_2 nanoparticles exhibited more elongated cell aggregates with a higher aspect ratio (2.26 ± 0.57) compared to the unmodified one (1.17± 0.14). These findings suggest that the incorporation of c-ZrO_2 nanoparticles may provide a more favourable environment for osteogenic differentiation, paramount for bone regeneration.

This study presents a more eco-friendly process using Ca to stabilise c-ZrO_2 nanoparticles and demonstrates how their incorporation into alginate scaffolds produces promising osteoinductive properties.

Keywords: Tissue engineering, calcium, cubic ZrO_2 stabilisation, osteochondral tissue, periodontal tissue, osteoinductive scaffolds.

Resumo

A regeneração efetiva da componente óssea do tecido osteocondral e periodontal continua um desafio. A engenharia de tecidos (TE) tem-se dedicado a desenvolver estratégias para esta regeneração, utilizando frequentemente polímeros naturais como o alginato. Contudo, estes materiais carecem das propriedades adequadas para suportar a regeneração óssea.

Foi reportada pela primeira vez a estabilização de nanopartículas cúbicas de zircónia (c-ZrO_2) utilizando o cálcio (Ca) como um elemento estabilizador. Isto foi alcançado através de um processo hidrotermal assistido por micro-ondas sem qualquer pré ou pós tratamento, resultando numa síntese mais sustentável e económica, tirando partido da abundância do Ca, da sua biocompatibilidade e bioatividade. A estabilização da fase cúbica foi demonstrada através de espetroscopia de Raman e microscopia eletrónica de transmissão de varrimento (STEM). As nanopartículas de c-ZrO_2 sintetizadas apresentaram um tamanho médio de 6.24 ± 0.96 nm e uma maior área superficial especifica. A nanotecnologia apresenta-se uma mais valia para a melhoria das propriedades de *scaffolds* em ambientes de elevada exigência mecânica. Posto isto, as nanopartículas de c-ZrO_2 foram incorporadas em *scaffolds* de alginato por um método de encharcamento. Os nanocompósitos obtidos não apresentaram diferenças significativas em termos de morfologia e degradação quando comparados com os *scaffolds* originais. A incorporação das nanopartículas resultou num decréscimo significativo na capacidade de inchamento dos *scaffolds.* Surpreendentemente, os *scaffolds* funcionalizados com nanopartículas exibiram apenas um ligeiro aumento do módulo de Young. Estudos preliminares de citotoxicidade *in vitro* indicaram que a incorporação das nanopartículas não produziu qualquer tipo de citotoxicidade. Notavelmente, após um período de cultura celular de 7 dias com células estaminais mesenquimais da medula óssea humana (BM-MSCs), o grupo funcionalizado com nanopartículas de c-ZrO_2 exibiu agregados celulares mais alongados com um maior rácio de aspeto (2.26 ± 0.57), comparado o grupo em que não foi feita esta modificação (1.17± 0.14). Estes resultados sugerem que a incorporação destas nanopartículas pode proporcionar um ambiente mais favorável à diferenciação osteogénica, essencial para a regeneração de tecido ósseo.

Este estudo apresenta um processo mais ecológico utilizando o Ca para estabilizar nanopartículas de c-ZrO_2 e demonstra como a sua adição em *scaffolds* de alginato oferece características osteoindutoras promissoras.

Palavras chave: Engenharia de tecidos, estabilização de ZrO_2 cúbica, tecido osteocondral, tecido periodontal, *scaffolds* osteoindutores.

List of Contents

List of Figures

List of Tables

List of Equations

Abbreviations

3D	Three dimensional
ALP	Alkaline phosphatase
a.u	Arbitrary unit
BET	Brunaeur-Emmet-Teller
BM-MSCs	Bone marrow mesenchymal stem cells
Ca	Calcium
COO^-	Sodium alginate (carboxylate group)
c-ZrO_2	Cubic zirconia
DMEM	Dulbecco's modified Eagle Medium
ECM	Extracellular matrix
EDAC	1-ethyl-3-dimethyl aminopropyl carbodiimide
EDS	Energy dispersive x-Ray spectroscopy
ESCs	Embryonic stem cells
FA	Focal adhesion
FBS	Fetal bovine serum
FFT	Fast Fourier transform
HAADF	High-angle annular dark-field
ICDD	International Centre for Diffraction Data
iPSCs	Induced pluripotent stem cells
ISO	International Standard Organization
MSCs	Mesenchymal stem cells
MTT	3-(4,5-Dimethylthiazol-2-yl)-2,5-diphenyltetrazolium bromide
m-ZrO_2	Monoclinic zirconia

NHS	N-Hydroxy-succinimide
PBS	Phosphate buffered saline
PDL	Periodontal ligament
PDLSCs	Periodontal ligament stem cells
PEG	Polyethylene glycol
ROCK	RhoA/Rho-associated kinase
RT	Room temperature
S.D	Standard deviation
SE	Secondary electron
SEM	Scanning electron microscopy
STEM	Scanning transmission electron microscopy
TE	Tissue engineering
t-ZrO_2	Tetragonal zirconia
W_0	Pre-weighted freeze-dried scaffolds
W_f	Re-weighted scaffolds after air drying
W_S	Re-weighted scaffolds after PBS submersion
XRD	X-ray diffraction
Zr	Zirconium

List of symbols

2Θ	Angle between the incident and the diffracted beam
$\mathbf{d_{hkl}}$	Interplanar distance
E	Young's modulus
p	Level of probability
p	Equilibrium pressure
$\boldsymbol{p_0}$	Saturation pressure
α	Significance level
ε	Strain
λ	Wavelength
ρ	Density
σ	Stress
º	Degrees
ºC	Degrees Celsius

Chapter 1: Introduction and Hypothesis and Aims

1.1 Introduction

1.1.1 TE

Currently, tissue loss and organ failure resulting from disease or injury represent significant healthcare challenges, due to the scarcity of transplantable tissues or organs, primarily because of the shortage of compatible donors.[1,2] Given the limited self-regenerative capacity of human tissues, the urge to heal damaged tissues has resulted in a clinical demand for TE solutions. Nevertheless, the available medical tools are not capable of completely and efficiently restoring tissues and therefore overcoming the necessity of donors and prosthetics.[3,4]

TE represents a rapidly evolving interdisciplinary field that integrates numerous areas including materials science, genetics, biology, mechanical engineering, and clinical medicine, converging the knowledge and methodologies from both engineering and life sciences. Despite the TE term being only officially coined in 1988, the concept and the need to restore tissues have deep historical roots.[5] Therefore, TE's main aim is to develop novel tissues that closely mimic the function and properties of natural tissues. These engineered tissues serve as biological substitutes, intended for implantation into the body to replace, restore, or augment organ function.[6]

Commonly, TE approaches involve the utilisation of living cells with natural, synthetic or bioartificial support, typically referred to as a scaffold and signal cues to produce a biological substitute or 3D bio-constructs that closely mimics the structure, function and mechanical environment of the native tissue[7], as illustrated in **Figure 1.1.**

Several cell sources are employed in TE for different target tissues. Primary cells are mature cells derived from a particular tissue directly extracted from a specific tissue through surgical procedures. Despite showing favourable immunological compatibility, their proliferation is diminished due to their post-mitotic and differentiated status. Furthermore, isolating cells from a specific tissue is not always feasible.[8] Stem cells have provided a new paradigm in TE, due to their self-renewal potential and capacity to differentiate into multiple cellular types. [9,10] They can be classified into adult stem cells and embryonic stem cells (ESCs). Despite having a superior regenerative potential (pluripotency), and plasticity than adult stem cells, ESCs utilisation is more limited due to ethical and moral concerns.[11] Adult stem cells are multipotent and also present a high degree of plasticity.[11,12] Regarding those, mesenchymal stem cells (MSCs) stand out as the most promising and widely used because of their ease of isolation and manipulation. MSCs are prevalent in various tissues, such as bone marrow, dental and adipose tissues, offering multiple extraction options and, thereby reducing the need for invasive harvesting procedures.[13] Lastly, induced pluripotent stem cells (iPSCs) have emerged also as a promising cell source. Unlike ESCs, which raise ethical concerns due to their derivation from early-stage embryos, iPSCs are generated by reprogramming mature somatic cells back to a pluripotent state. Nevertheless, the current methods for iPSCs generation may institute undesired genetic abnormalities or tumorigenicity, challenging their current application in TE.[13,14]

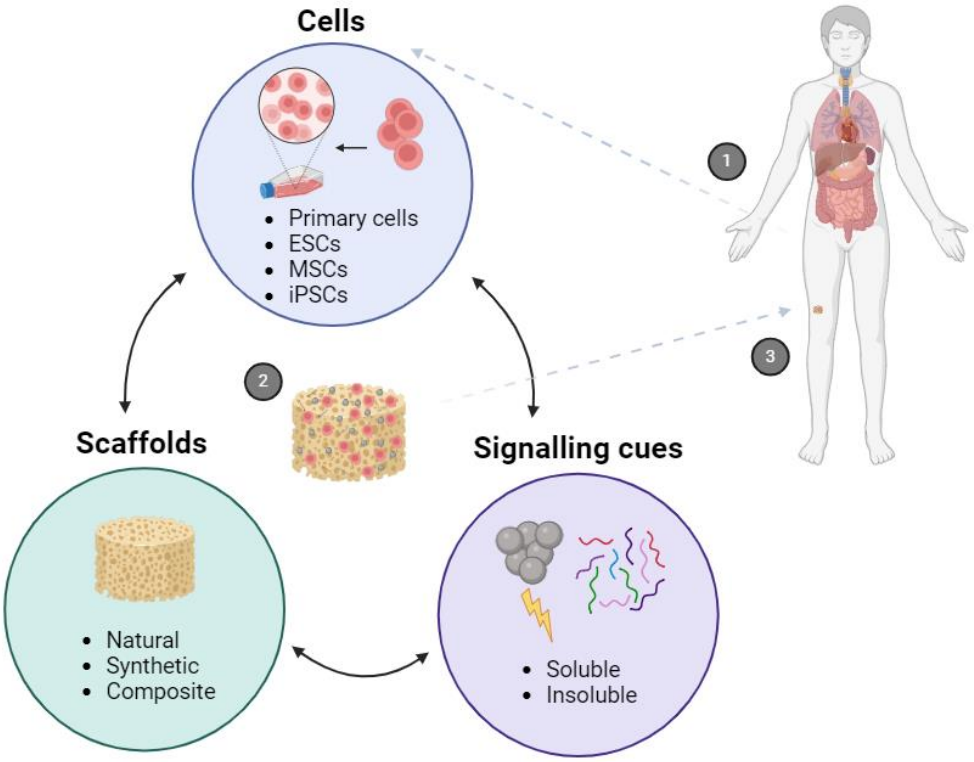

Figure 1.1: TE Triad. The interplay of cell sources, scaffold types and signalling cues in final construct development and implantation. Image created using BioRender (https://www.biorender.com/)

Scaffolds provide a three-dimensional (3D) template for tissue reconstruction designed to closely mimic the native tissue environment providing morphological, chemical and biomechanical cues to guide cell fate until the production of extracellular matrix (ECM) takes over.[15] Scaffolds must provide an adequate environment for cell attachment, migration and proliferation, consequently, microarchitecture features such as morphology, porosity and pore size are paramount for ensuring effective nutrient supply and supporting the scaffolds' water uptake.[16,17] Moreover, scaffolds also must exhibit biocompatibility to support cell growth and elicit a minimal immunological response after implantation. Additionally, given their role as a transient matrix for tissue development, their biodegradability should complement neo-tissue formation. Importantly, scaffolds' mechanical properties should be similar to the intrinsic properties of the anatomical site of implantation to ensure correct support and guide cell behaviour.[18,19]

Biomaterials used to design 3D scaffolds are categorised primarily based on their chemical composition into metals, ceramics and glass-ceramics, natural and synthetic polymers and composites. Recently, there has been a shift in focus towards biodegradable biomaterials that do not necessitate removal from the organism after implantation .[20] Polymeric biomaterials are predominantly selected for the design and fabrication of scaffolds due to their versatility, accessibility and affordability.[21] Natural polymers, such as chitosan, alginate and collagen are extremely biocompatible, non-toxic, biodegradable and can undergo chemical modifications. However, they often show poor mechanical strength.[21,22] On the other side synthetic polymers demonstrate better mechanical properties but often elicit immune responses.[23] To produce polymeric scaffolds various methods have been utilised[24],

including, solvent casting[25], gas foaming[26], thermal induce phase separation[27], electrospinning[28] and additive manufacturing techniques such as 3D bioprinting[29], which has marked a new era in bioengineering .

Signalling cues are fundamental in TE, as their integration facilitates and accelerates the regenerative process. These signal cues can be soluble and insoluble. Soluble signal cues comprise bioactive small molecules, including proteins, hormones, cytokines, growth factors and nuclei acid delivered via vectors.[30,31] Besides, insoluble cues such as biophysical and biomechanical cues notably alter substrate stiffness and topography at the micro and nanoscale, significantly impacting the ECM-cell interactions. These interactions lead to changes in cell shape and adhesion, gene expression proliferation, migration and differentiation.[30,32,33]

Nowadays, TE continues to encounter substantial obstacles, especially concerning the shortage of suitable and effective biomaterials that accurately stimulate cell growth and behaviour by mimicking the native properties of the target tissue, including architecture and mechanical features, essential for biological and overall substitute performance.[34,35] Nanotechnology, with nanoparticles at its forefront, has emerged as a promising tool for TE. Polymer-based nanocomposites exhibit significant benefits due to the integration of nanoparticles. This reinforcement can provide biophysical cues, which leads to enhanced mechanical and biological performances, fostering an improved niche for the interplay between cells and the ECM, thereby influencing cellular behaviour.[34,36–39]

1.1.2 Nanoparticles in TE

Nanoparticles, as a subset of nanomaterials, are characterised by their nano-scale size, typically ranging from 1 to 100 nm in all three dimensions.[40–42] Furthermore, nanoparticles differ from their bulk counterparts primarily, exhibiting unique properties including a high surface area, and distinctive mechanical, thermal, magnetic, electronic, optical and catalytic properties.[43]

In the context of TE, nanoparticles have emerged as pivotal components in the development of advanced biomaterials.[44,45] These nanoscale entities enable the precise adjustment of scaffolds due to their biocompatibility, enhancing their mechanical properties, facilitating the controlled release of bioactive molecules, improving targeting and imaging capabilities, and leveraging antimicrobial properties. Based on their application for TE, purposes nanoparticles can be broadly categorised into two main groups based on their composition: inorganic and organic. Inorganic nanoparticles encompass metals and ceramics, among which ceramics can be further divided into bioactive, biodegradable, or bioinert types, depending on their biological interactions, as exhibited in **Table 1.1**.[46]

Table 1.1: **An overview of the different ceramic nanoparticle categories mainly utilised in TE**. Mainly adapted from [46–48]

Types			Utilities	Examples	TE
Nanoparticles	Ceramic	Bioactive	-Enhance protein adsorption -Ion release -Antibacterial -Promote osteogenic differentiation -High similarity with mineral components of tissues	SiO_2-CaO, SiO_2-CaO-P_2O_5, hydroxyapatite	Bone[49–51], tooth[52,53] peridontium[53]
		Bioresorbable	-Increase cell attachment - Promote osteogenic differentiation -Resorption capability -Drug delivery -Some similarity with mineral components of tissues	Tricalcium phosphate, $CaCO_3$	Bone[54,55], peridontium[56], tooth[57]
		Bioinert	-Antimicrobial -High mechanical strength and wear-resistance -Chemical stability - Non-immunogenic - Promote osteogenic differentiation	ZrO_2, TiO_2	Bone[58,58], cartilage[58] periodontium[58], tooth[58,58]

1.1.2.1 ZrO_2 nanoparticles

The incorporation of ceramic nanoparticles, notably zirconium dioxide, ZrO_2, commonly known as zirconia, into scaffolds facilitates the modulation and enhancement of biomechanical attributes, highlighting its significance in developing advanced TE constructs. [69–71] ZrO_2 is categorised as a bioinert ceramic. [72] Bioinert ceramics stand out among ceramic biomaterials due to their exceptional mechanical strength and chemical stability. These attributes make them highly suitable for implantation within the human body, leading to minimal toxic and immunological reactions.[48,73] Among bioinert ceramics, ZrO_2 has been known as “ceramic steel” [74], due to its mechanical properties resembling those of stainless steel.[75] ZrO_2 exhibits remarkable strength, hardness, fatigue resistance and wear resistance.[76] While Al_2O_3 [77] and TiO_2 [78] have been extensively studied and utilised in dentistry and orthopaedical biomedical devices, ZrO_2 stands out for its exceptional fracture toughness. Therefore, the ability of ZrO_2 to improve mechanical properties when added to other materials makes it a versatile component in composite biomaterials.[75,79] This characteristic allows for advanced polymeric nature-derived scaffolds with

substantially improved mechanical performance. Such scaffolds can better withstand substantial physiological loads while maintaining their structural integrity throughout the tissue regeneration process, not compromising their biodegradability. Consequently, they provide optimised biophysical and biomechanical cues for mechanically challenging load-bearing TE applications.[39,46,80–82]. One such application is the development of engineered bone tissues, where ZrO_2 nanoparticles show great promise due to their capacity to promote the osteogenic differentiation of progenitor cells into osteoblasts, which are responsible for producing bone matrix. Therefore, incorporating ZrO_2 nanoparticles may provide important cues for developing scaffolds that better mimic bone tissues, characterised by challenging environments [83–86].

ZrO_2 is a metal oxide that usually crystallises in three phases ZrO_2: c-ZrO_2, tetragonal (t-ZrO_2), and monoclinic (m-ZrO_2) (**Figure 1.2**). The cubic phase has a fluorite (CaF_2) structure, and the tetragonal and monoclinic phases are distorted versions of the former. [87] ZrO_2 is stable in the cubic form at high temperatures (often over 2377°C), in the tetragonal form between 1205 and 2377 °C, and in the monoclinic phase from room temperature (RT) to 1205°C.[88]

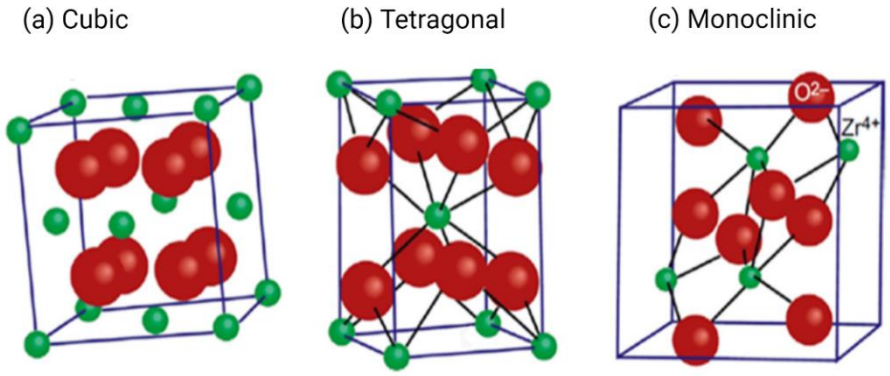

Figure 1.2: Unit cells of ZrO_2 in its three predominant crystalline phases. (A) Cubic. (B)Tetragonal. (C) Monoclinic. Oxygen atoms are represented in red, while zirconium (Zr) atoms are shown in green. Adapted from *Farid et al.*[89]

Furthermore, two additional polymorphs were identified, *i.e.,* orthorhombic-I and -II, at lower temperatures with increasing pressure.[90,91] It is known that the coordination number of Zr^{4+} cations is 7 for the monoclinic phase, whereas for cubic and tetragonal phases this number is 8. The strong covalent nature of the Zr-O bond favours a sevenfold coordination number, thus making monoclinic ZrO_2 thermodynamically stable at lower temperatures, particularly at RT. The stabilisation of both tetragonal and cubic phases at higher temperatures is associated with the lattice oxygen ion vacancy concentration in bulk ZrO_2 that increases at higher temperatures.[90]

Several studies have identified t-ZrO_2 as the most suitable and utilised for dentistry and orthopaedics applications. These fields involve tissues, including bone tissues, that are typically characterised by mechanically demanding and load-bearing environments.[83,92–96] Among, ZrO_2 crystalline phases, t-ZrO_2 exhibits outstanding toughness to fracture and elevated strength, as well as

a high elastic modulus and wear resistance.[92,94] These properties, especially the fracture toughness and damage resistance are related to a controlled tetragonal to monoclinic transformation, which may occur under stress. This phase transformation culminates with a volume increase of 4 to 5%, preventing crack propagation.[97,98]

Since t-ZrO_2 and c-ZrO_2 are known to be high-temperature phases that are thermodynamically unstable at RT, significant research efforts have been focusing on stabilising these phases under ambient conditions. This stabilisation is typically achieved either by doping with a proper cationic stabiliser or through the reduction of nanoparticle size below a critical threshold.[90]

Currently, for biomedical applications yttrium, a rare earth element, is widely applied as a stabiliser dopant for ZrO_2.[99,100] Moreover, several production techniques have been employed for the synthesis and stabilisation of t-ZrO_2 and c-ZrO_2 nanoparticles, including sol-gel method[101–106], co-precipitation[107,108], hydrothermal method[109–111], solution combustion method[112–115], among others. Additionally, most of the studies reported required high-temperature and post-treatments to synthesise the aforementioned phases.[105,115,116] Therefore, growing environmental and geopolitical concerns about rare earth elements mining alongside the need for greener and more economical synthesis methods have been stimulating the research for alternative strategies. These efforts aim to seek more environmentally friendly stabilisers and cost-effective synthesis techniques.[117–120] Recently, microwave-assisted synthesis appeared as a viable and efficient method for ZrO_2 regarding energy and cost criteria.[120–122]

1.1.3 ZrO_2 nanoparticles for TE applications

1.1.3.1 Osteochondral Tissue in clinical need

The osteochondral tissue is a composite system constituted of articular cartilage, calcified cartilage, and subchondral bone in articulating joints. This system is proficient in the transference of loads during joint motion, compromising the intersection of cartilage and bone. It is constituted of distinguished areas with different structures as illustrated in **Figure 1.3**.[123,124]

The articular cartilage is a low-friction, lubricated, and smooth layer of tissue that has the capacity to support compressive loads and shear forces during the synovial joint's extent of movement. Structurally, articular cartilage displays a multi-layer structure formed by superficial, middle, deep and calcified regions.[125,126] Contrary to most tissues, it lacks nerves, blood and lymphatic vessels, resulting in a poor regenerative capacity. Moreover, it is compounded by a dense ECM predominantly made of collagen, proteoglycans and water. Chondrocytes, derived from differentiated MSCs, are an essential cell type present in the articular cartilage. This cell type is responsible for the production of collagen and the ECM, performing a crucial role in its development, maintenance, and repair.[127,128]

Lastly, beneath the cartilage lies the subchondral bone, a vascularised structure, that provides both metabolically and mechanical support to the articular cartilage, preserving the joint shape and

absorbing shock. Osteoblasts, a product of MSCs osteogenic differentiation, are responsible for bone formation through the production of ECM, predominantly made of water, collagen and inorganic compounds.[129–131] Structurally, the subchondral bone is divided into the subchondral bone plate and the subchondral trabecular bone. The first is composed of a thin layer of cortical bone, whereas the second is highly vascularised, supplying nutrients to the cartilage besides the ones present in the synovial fluid.[132,133]

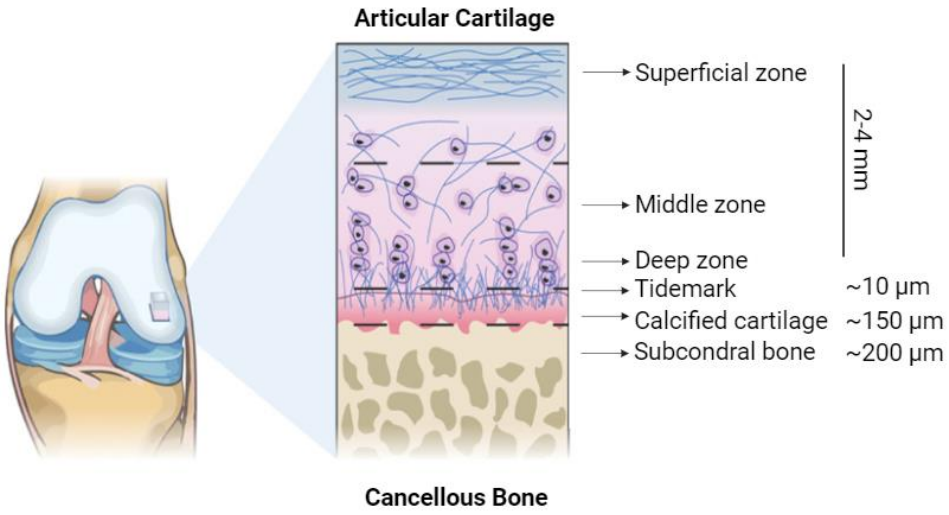

Figure 1.3: Schematic representation of the osteochondral tissue and its various layers. Adapted from Frassica et al[123]

Currently, osteochondral lesions and defects are major health concerns.[134] These injuries are predominantly caused by trauma-related injuries and their development is normally age-related.[135,136] The progression and worsening of these lesions and resulting defects present as a risk factor for the onset of osteoarthritis, a degenerative disease affecting millions of people worldwide.[137] Currently, the main treatment options are primarily palliative to alleviate symptoms or reparative and potentially invasive. These include microfracture techniques for smaller defects, and autograft or allograft transplantations for large defects that penetrate through the subchondral bone.[135,138,139] At present, restoring or even repairing osteochondral tissue with the desired durability and longevity is impossible. Therefore, in response to these limitations, TE has emerged as a promising alternative.[135]

Lately, ZrO_2 nanoparticles have been proven to have great potential as a reinforcing biomaterial for osteochondral TE, especially in enhancing scaffolds' mechanical properties which is paramount in a mechanically demanding environment, particularly when utilising polymeric matrices.[140,141] This is crucial for subchondral bone regeneration, where load-bearing capacity is essential.[141] Moreover, there is evidence that ZrO_2 nanoparticles can improve MSCs osteogenic potential fostering an osteoinductive environment [142–144] While primarily known for their bone-relates benefits ZrO_2 nanoparticles have also demonstrated potential in cartilage regeneration. When incorporated into scaffolds these nanoparticles resulted in a favourable biomimetic environment proper for chondrocyte deposition[145]. Additionally,

another study highlighted that the reinforcement of alginate-based scaffolds with ZrO_2 nanoparticles allowed to adjust scaffold properties, simultaneously improving its mechanical properties and cell adhesion. Therefore, fostering an advantageous microenvironment for osteochondral TE. [80] Thus, the incorporation of these nanoparticles into scaffolds has shown promise as an innovative approach for developing more effective treatments for complex osteochondral defects.[141]

1.1.3.2 Periodontal tissue in clinical need

The periodontal tissue, also known as periodontium, is a structurally diverse complex comprising both soft and hard tissues. It consists of four distinct components: the alveolar bone, the periodontal ligament, the cementum, and the gingiva, as represented in **Figure 1.4**. Among these, the gingiva, the periodontal ligament and the alveolar bone are highly vascularised.[146]

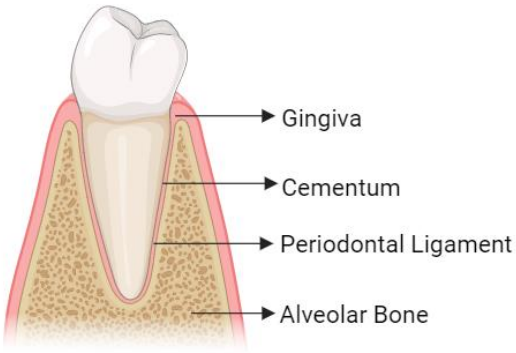

Figure 1.4: Schematic representation of the periodontal tissue under a premolar and its various components. Image created using BioRender (https://www.biorender.com/).

The alveolar bone, a component of the jaws, surrounds the roots of teeth, providing mechanical and structural support during mastication. It consists of an outer cortical plate and an inner trabecular component. Moreover, this bone plays a crucial role in mineral homeostasis. The ECM of alveolar bone is composed of collagen fibres embedded in a mineralised matrix, therefore having both an organic and inorganic composition. The alveolar bone, due to constant remodelling, contains various cell types involved in the turnover process. Osteoblasts, which are the product of osteogenic differentiation, are among these cells. These bone-forming cells are responsible for ECM production.[146–149]

The periodontal ligament (PDL) is a soft connective tissue localised between the alveolar bone and the cementum. This ligament is capable of widening in response to functional overloading protecting the teeth against external forces.[150] Besides, the PDL also has mechanoreceptors essential for proper tooth positioning during mastication.[151] The ECM of this fibrous tissue contains both collagen and non-collagen proteins like glycoproteins. [151] Fibroblasts, the primary cell type in PDL, are responsible for

collagen turnover. Other cell populations include osteoblasts and MSCs, with MSCs playing a role in periodontal repair and regeneration.[152,153]

Cementum is a mineralised avascular connective tissue that envelops the tooth roots. It provides support within the alveolar socket and allows attachment of PDL fibres. Additionally, cementum prevents root resorption during periodontal remodelling. Two types of cementum exist: cellular and acellular, covering different root regions. Cellular cementum contains cementoblasts.[154–156] Moreover, as a mineralised tissue, cementum has significant inorganic and organic components, with the latter primarily composed of collagen.[146]

Lastly, the gingiva constitutes a specialised component of the periodontal tissue, serving as the outside protective barrier against mechanical trauma and microorganisms.[157] The gingival tissue exhibits structural diversity. Its epithelium, primarily keratinised on the masticatory surface, consists of closely apposed cells with minimal extracellular space. In contrast, the underlying connective tissue has a lower cellular component, characterised by an integrated network of fibrous (mainly collagen) and non-fibrous proteins. Moreover, fibroblasts play a key role in maintaining this connective tissue structure.[158,159]

Periodontal disease is characterised by the progressive deterioration of both soft and hard periodontal tissues, initiated by bacterial colonisation that elicits a dysregulated host inflammatory response destroying the surrounding tissues. Gingivitis represents its initial manifestation affecting up to 90% of the population.[155,160] If untreated, gingivitis may progress to periodontitis, a severe disease affecting 19% of the adults.[161,162] Severe periodontitis is the primary cause of tooth loss. It causes the destruction of the alveolar bone, which results in the loss of structural support for teeth.[163,164] Currently, the available treatment options include professional cleaning to remove bacterial biofilm, defect filling with bone grafts (predominantly autologous), guided tissue and bone regeneration using barrier membranes to promote self-periodontal regeneration while impeding undesired cell infiltration, and the application of enamel matrix derivatives.[160,161,165] Nevertheless, despite the recent advances in periodontology the actual approaches fail to effectively regenerate the periodontal apparatus with the desired predictability and consistency. Therefore, novel progress in periodontal TE is essential to overcome these shortcomings [166,167]

At present, nanotechnology holds great promise for periodontal TE.[168] Severe periodontitis leads to alveolar bone destruction and tooth loss. A key challenge in periodontal TE and alveolar bone augmentation is developing scaffolds that can withstand masticatory forces.[163,169] Therefore, as previously mentioned, reinforcing scaffolds, particularly polymeric ones, with ZrO_2 leads to better mechanical properties and potentially creates an osteoinductive environment that enhances osteogenic differentiation, making them a viable option for alveolar bone regeneration strategies.[141,142,144] Besides enhancing scaffolds' mechanical properties, ZrO_2 nanoparticles possess essential antimicrobial characteristics that combat oral pathogens during periodontal regeneration.[170–174] Recently, a study reported that the incorporation of ZrO_2 nanoparticles into a polymeric biodegradable nanofibrous resulted in favourable cytocompatibility, cell proliferation and antimicrobial efficiency against oral pathogens for periodontal guided TE.[175]

1.2 Hypothesis and Aims

The inherent limitations in human tissue regeneration have given rise to significant clinical demand for advanced TE approaches.[4,176] Current therapeutic strategies in orthopaedics and dentistry still lack the desired consistency and predictability in addressing osteochondral[135,138] and periodontal[160,161] defects, failing to effectively regenerate the affected areas.

Taking this into consideration, natural polymers, such as alginate, have been extensively employed due to their biocompatibility, biodegradability, and ability to mimic the ECM.[177] Indeed, alginate scaffolds can be architecturally modified to more closely resemble native tissue structure, moreover through carbodiimide chemistry these scaffolds can also be engineered to exhibit shape-memory properties.[178] Nevertheless, natural polymers often present poor mechanical properties.[23,179] This limitation is particularly relevant in the context of, periodontal[180] and osteochondral tissues[181], where structural integrity and the capacity to withstand mechanically challenging load-bearing environments is crucial.

Nanoparticles have appeared as a promising tool for improving scaffold properties. [34,46] Among these, bioinert ceramics such as ZrO_2 have demonstrated biocompatibility[75], ability to promote osteogenic differentiation[83–85], chemical stability[48] and outstanding mechanical properties[73,75] Thus, biomaterials reinforced with these nanoparticles showed enhanced mechanical properties, providing an optimised biomechanical environment. This phenomenon has previously been documented for alginate-based scaffolds.[75,79,182] This overall enhancement in the mechanical properties is of particular interest, as matrices with increased stiffness are known to influence MSCs' differentiation commitment towards an osteogenic lineage. This influence is paramount in bone regeneration, including subchondral and alveolar bone.[183,184]

Among ZrO_2 nanoparticles, m-ZrO_2 is generally considered to possess low strength and toughness [185], while t-ZrO_2 is described as the most suitable for biomedical applications in mechanically demanding conditions. In the case of c-ZrO_2, studies reporting the application of c-ZrO_2 for these purposes are lacking in the literature.[97,186,187] Rare earth elements are commonly used to stabilise high-temperature ZrO_2 phases. [99,100] However, these elements are expensive and raise environmental concerns.[118,188] Moreover, current synthesis methods require high-temperature processing.[105,115,116] Therefore, these issues create opportunities for research into greener and more cost-effective alternatives.

The global aim of this proposal is to develop a new generation of ZrO_2 nanoparticles to enhance the osteoinductive properties of scaffolds for bone regeneration regarding osteochondral and periodontal tissues. To this end, the nanoparticles will be used to functionalise porous, biomimetic shape-memory alginate scaffolds.

We hypothesised that using Ca as a stabiliser and synthesising ZrO_2 nanoparticles via microwave-assisted hydrothermal method would potentially stabilise ZrO_2 phases at lower temperatures. This approach could guarantee process sustainability while addressing the biomedical

performance of ZrO_2 phases other than the tetragonal. This approach could offer a more environmentally friendly and cost-effective alternative, taking advantage of Ca abundance, bioactivity and biocompatibility. We propose that incorporating these nanoparticles into alginate scaffolds will enhance mechanical robustness and induce beneficial changes in topography, potentially improving their osteoinductive properties for the intended TE applications. To attend this goal this thesis is structured into two main chapters:

1. **Synthesis and characterisation of Ca-stabilised ZrO_2 nanoparticles**
    - Synthesis of ZrO_2 nanoparticles with different amounts of Ca
    - Characterisation of the obtained nanoparticles to assess the impact of the Ca content on phase transformation
2. **Incorporation of Ca-stabilised cubic ZrO_2 nanoparticles into shape memory-alginate scaffolds**
    - Assessment of c-ZrO_2 nanoparticle reinforcement impact on scaffolds' osteoinductive potential via systematic comparison of properties, including morphological, mechanical and biological characteristics, with those of the unmodified scaffolds

Chapter 2: Synthesis and Characterisation of Ca-Stabilised ZrO_2 Nanoparticles

2.1 Chapter Overview

In the present chapter, ZrO_2 nanoparticles were synthesised using a hydrothermal method assisted with microwave irradiation using Ca as a stabilising element. The effect of varying Ca molar concentrations (3, 7, and 10 mol.%) on ZrO_2 phase transformation was investigated through X-ray diffraction (XRD), Raman spectroscopy and STEM analysis. Additionally, energy dispersive X-ray spectroscopy (EDS) analysis was employed to evaluate the distribution of Ca throughout the nanoparticles and to detect any impurities. Lastly, the specific surface area of the nanopowders was determined using the Brunauer-Emmett-Teller (BET) method.

2.2 Introduction

The ZrO_2 crystalline phase plays a key role in some applications, in which the t-ZrO_2 has been preferred for biomedical applications in mechanically challenging conditions.[83,97,186] Indeed, at RT, both cubic and tetragonal phases are unstable in bulk forms. Thus, extensive efforts have been devoted to stabilising both phases at such temperatures, either by doping with various cationic stabilisers or reducing particle size to a critical nanometre range[90].

In the case of doping, yttrium is largely used as a stabiliser dopant, however other bivalent or trivalent cations have also been reported (La^{3+}, Ga^{3+}, Ca^{2+}, Fe^{2+}, Mg^{2+}, among others) [99,189]. In fact, seeking more sustainable stabiliser elements is imperative, especially since nowadays there are concerns in rare earth elements mining, such as the shortage of economically viable deposits and environmental risks, providing space for greener and more cost-effective options.[118] Moreover, it is well-known that China holds a dominant position in the global supply chain of rare earth elements. Thus, the economic implications of geopolitical tensions are profound, as they lead to an exponential increase in prices and a decrease in export quantities, significantly impacting the global economic system.[119]

It has been suggested that lower valence dopants (<+4) on ZrO_2 surfaces potentiate the formation of surface oxygen vacancies upon doping.[190] When these bivalent and trivalent cations replace the Zr^{4+} ions, oxygen vacancies are generated due to charge compensation.[99] Among the bivalent and trivalent cations, when doping occurs with larger cations than Zr^{4+} (*eg.*, Y^{3+} or Ca^{2+}), the eightfold coordination is favoured, which allows the association of oxygen ion vacancies with the Zr^{4+} cations, leading to a large concentration of oxygen ion vacancies from the Zr^{4+} cations. In contrast, when smaller cations are selected (*e.g.*, Fe^{2+} or Ga^{3+}), the sixfold coordination is facilitated, and the oxygen ion vacancies will be contested between the stabiliser and the Zr^{4+} cations, resulting in smaller concentrations of oxygen ion vacancies associated with the Zr^{4+} cations.[90]

In the case of the c-ZrO_2, when stabilised at high temperature (2377 °C), the Zr^{4+} cations occupy the sites of the face-centred cubic cell, while O^{2-} anions are positioned within the tetrahedral voids. However, at low temperatures, the effective size of the Zr^{4+} cations become insufficient to maintain the large tetrahedral voids for the cubic structure, and thus Zr^{4+} must be partially substituted with a larger

cation of lower valence to stabilise the structure. Like the tetragonal phase, the cubic phase has also been reported to be highly defective, with atomic displacements caused by the incorporation of stabilising elements into its lattice.[191] The presence of structural defects on ZrO_2 nanoparticles has been extensively investigated [191–195], however, there are no reports imaging atomic structural defects on stabilised c-ZrO_2 nanoparticles (<10 nm), which implies a gap in the literature because these defects are crucial in various applications.

Several production techniques have been employed for the stabilisation of t-ZrO_2 or c-ZrO_2.[101,108,111,114,196] Most of these studies of nanosized ZrO_2 require a post-treatment for the formation of the tetragonal phase, *i.e.*, calcination at temperatures higher than 500 ºC.[105,116] In the case of the cubic phase, it has been reported that a heat treatment of 400 ºC is needed for its stabilisation.[115] More recently, microwave synthesis has emerged as an appealing technique to produce nanostructured ZrO_2.[121,122] Synthesis assisted by microwave irradiation has advantages over conventional hydrothermal/solvothermal methods, since it is cost/energy efficient, fast, and produces homogeneous and reproducible materials with high yields. [120]

This chapter reports the effect of different amounts of Ca (3, 7, and 10 mol.%) on the ZrO_2 phase transformation and further stabilisation of the c-ZrO_2 crystalline phase using microwave irradiation. Moreover, to the author's best knowledge, this is the first time that has been reported ZrO_2 nanoparticles synthesised with Ca as a stabiliser element through a one-step microwave process (fast and low-temperature synthesis) without any pre- or post-treatment. Ca was selected as a stabiliser due to its abundance, biocompatibility, and bioactivity, enhancing its potential for TE and other biomedical applications.[197,198]

2.3 Materials and Methods

2.3.1 ZrO_2 synthesis under microwave irradiation

The ZrO_2 nanoparticles were synthesised using the hydrothermal method assisted by microwave irradiation, adapting the approach reported by *Matias et al*.[199] Therefore, 0.2 M of zirconium (IV) oxynitrate hydrate ($ZrO(NO_3)_2 \cdot xH_2O$; 99%, CAS:14985-18-3, Sigma-Aldrich) was mixed with a 0.4 M sodium hydroxide (NaOH; ≥ 98%; CAS:1310-73-2, Labchem) in an aqueous solution. All the reagents were used without further purification. The molar ratio of zirconium precursor and sodium hydroxide was maintained at 1:2. To prepare ZrO_2 nanopowders with Ca, 3, 7 and 10 mol.% of calcium nitrate tetrahydrate ($Ca(NO_3)_2 \cdot 4H_2O$; 99%; CAS:13477-34-4, Sigma-Aldrich) were added to the precursor solution before mixture. After homogenisation of the mixture, a whitish solution was obtained. The mixed solution was then distributed into Teflon vessels of 75 ml (each vessel containing 40 ml of solution) to carry out the microwave synthesis. The synthesis was carried out with a CEM MARS one microwave digestion system (CEM, Matthews, USA) and the applied parameters were 1000 W, 230 ± 10 °C and 1 h. The resulting nanopowder was then washed and centrifugated for 3 min at 4750 rpm for a total of eight times. Lastly, the nanopowder was dried in a desiccator at 60 ºC for five hours (**Figure 2.1**). The produced nanostructures are hereafter called: ZrO_2 (0 mol.% of Ca), and 3 mol.%Ca-ZrO_2, 7 mol.%Ca-ZrO_2 and 10 mol.%Ca-ZrO_2 for the materials with 3, 7 and 10 mol.% of Ca.

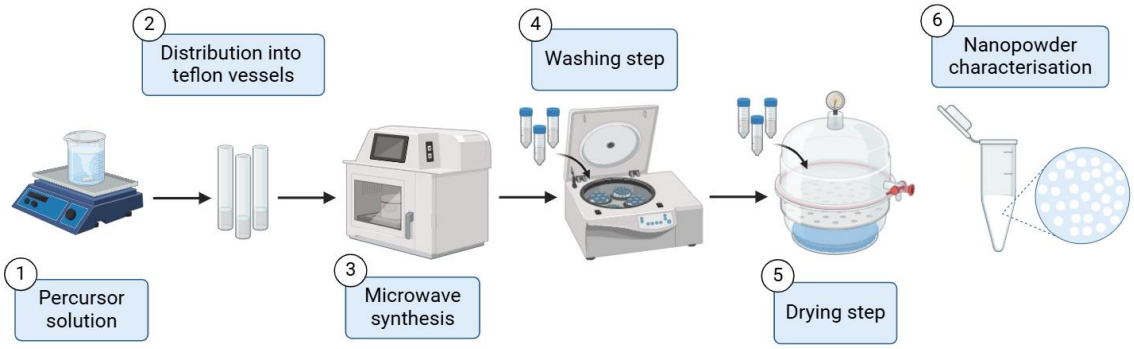

Figure 2.1: Overview of the synthesis procedure for ZrO_2 nanopowders without Ca and with different Ca amounts (3, 7 and 10 mol%). Key experimental steps are illustrated, including subsequent nanopowder characterisation. Image created using BioRender (https://www.biorender.com/)

2.3.2 Characterisation techniques

2.3.2.1 XRD

XRD experiments were carried out to identify the ZrO_2 crystalline phase. The crystalline phases of the obtained nanopowders were determined by comparison with the cards of the International Centre for Diffraction Data (ICDD). The reference monoclinic phase corresponds to ICDD file No. 00-037-1484,

the reference tetragonal phase to ICDD file No. 00-050-1089 and the reference cubic phase to ICDD file No. 00-049-1642. The XRD measurements were pursued using PANalytical's X'Pert PRO MRD X-ray diffractometer (PANalytical B.V., Almelo, The Netherlands) equipped with an X'Celerator one-dimensional detector and utilising a monochromatic CuKα radiation source (λ=1.540598 Å). XRD data were collected from 10º to 90º (*2Θ*) with a scanning step size of 0.033º and a time per step of 35 s.

2.3.2.2. Raman spectroscopy

Raman spectroscopy was conducted in a backscattering configuration using the 442 nm laser line in an HR800-UV system (Jobin- Yvon, Massachusetts, USA) equipped with a diffraction grating with 600 grooves/mm and using an objective lens of 50×.

2.3.2.3 STEM

STEM analyses were conducted using a Hitachi HF5000 (Hitachi, Tokyo, Japan) microscope equipped with an EDS detector from Oxford instruments at 200 kV. A sonicated dispersion of the ZrO_2 nanopowder was deposited onto 200-mesh copper grids coated with formvar and left to dry before imaging. Particle size and the respective standard deviation were determined from the STEM analysis considering 50 nanoparticles for each nanopowder using ImageJ Fiji (Version 2.9.0).

2.3.2.4 BET

The specific surface area was estimated by nitrogen adsorption according to the BET method, which was applied in the p/p_0 range determined following the methodology reported by the International Standard Organization (ISO) in standard number 9277.[200] The data were obtained at 77 K in an Autosorb IQ adsorption apparatus (Quantachrome, Florida, USA). Before the experiments, the ZrO_2 nanopowders (~0.2 g) were outgassed for 6 h at 120 ºC.

2.4 Results and Discussion

2.4.1 XRD

XRD measurements were carried out and are presented in **Figure 2.2**. It can be observed that the synthesised ZrO_2 nanopowder without Ca exhibits a mixture of t-ZrO_2 and m-ZrO_2, as previously observed in an analogous study.[199] Nevertheless, when Ca is added to the synthesis, it is shown that the 3 mol.%Ca-ZrO_2 nanopowder still demonstrates minor diffraction maxima of the monoclinic phase, which vanishes by increasing the amount of Ca. Both tetragonal and cubic phases have similar XRD diffractograms, so, Raman spectroscopy was employed to complement the analysis of the ZrO_2 crystalline phases.

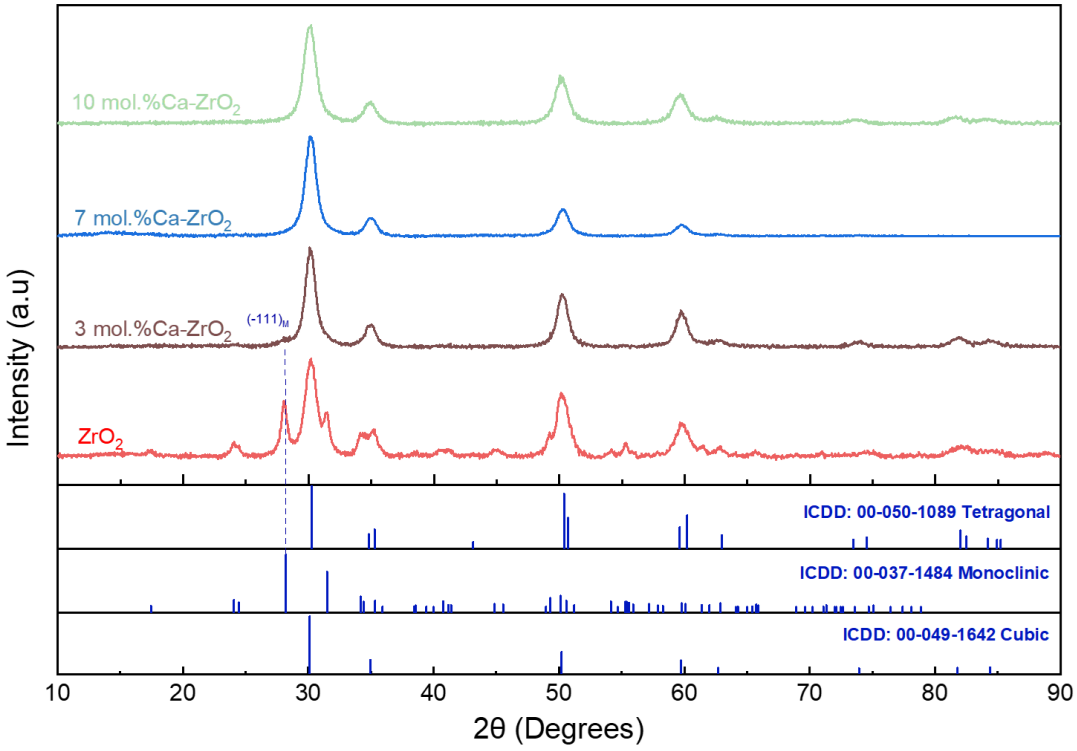

Figure 2.2: XRD diffractograms of the synthesised nanopowders. ZrO_2 nanoparticles without and with different amounts of Ca (3,7 and 10 mol.%), with ICDD reference patterns for the monoclinic, tetragonal and cubic phases.

2.4.2 Raman spectroscopy

The Raman spectra of the different phases of ZrO_2 are considerably different[201], and so this is a powerful technique to distinguish the effects promoted by the increase of Ca in the nanoparticles. Such spectra are depicted in **Figure 2.3**. Raman bands of ZrO_2 appear in the 130-700 cm^{-1} range, and it can be observed that the increase of Ca in the ZrO_2 nanopowders (from 3 to 10 mol.%) clearly reduces the number of Raman active modes, attributed to a rise in ZrO_2 crystal symmetry.[201] Moreover, Raman

spectroscopy is locally sensitive to the disorder in the first few atomic shells at the surface and lattice defects, which can not be detected in XRD analysis.[202]

From the Raman spectroscopy results, it can be inferred that the increase in Ca amount induced a phase transformation from monoclinic to tetragonal and then to cubic. A similar behaviour was previously reported after the incorporation of Y^{3+} or Er^{3+} ions in the ZrO_2 lattice.[203,204] For the m-ZrO_2 (C_{2h} point group), 18 Raman active vibrational modes ($9A_g + 9B_g$) at the Γ point of the first Brillouin zone were predicted.[199,203] The frequencies of these modes were shown to appear at 179 cm^{-1} (A_g), 190 cm^{-1} (A_g), 224 cm^{-1} (B_g), 305 cm^{-1} (A_g), 334 cm^{-1} (B_g), 348 cm^{-1} (A_g), 381 cm^{-1} (B_g), 476 cm^{-1} (A_g), 505 cm^{-1} (B_g), 536 cm^{-1} (B_g), 556 cm^{-1} (A_g), 616 cm^{-1} (B_g), 637 cm^{-1} (A_g).[205] As reported earlier, the t-ZrO_2, belonging to the D_{4h} point group, exhibits 6 Raman active modes with $A_{1g} + 2B_{1g} + 3E_g$ symmetries at the Γ point of the first Brillouin zone [206], with frequencies at 146 cm^{-1} (E_g), 270 cm^{-1} (A_{1g}), 318 cm^{-1} (B_{1g}), 458 cm^{-1} (E_g), 602 cm^{-1} (B_{1g}) and 648 cm^{-1} (E_g).[207] Vibrational bands assigned to both m-ZrO_2 and t-ZrO_2 are observed in the nanoparticles without Ca and with 3 mol.% of Ca, which is in agreement with the XRD results in **Figure 2.2**. This is in line with an analogous study, in which pure ZrO_2 nanoparticles were also synthesised at 230 ºC through a hydrothermal synthesis assisted by microwave irradiation.[208] For the addition of higher quantities of Ca, a smooth transformation to the cubic phase is observed, accompanied by the disappearance of the monoclinic modes. The Raman band broadening and intensity decrease was previously reported by Sinhamahapatra *et al*.[202] for black ZrO_2 produced by magnesiothermic reduction, which was related to the formation of oxygen vacancies at the surface, leading to crystal rearrangements. The 190 $cm^{-1}$and 476 cm^{-1} monoclinic bands possess high intensity and then undergo a reduction of intensities, as can be seen in **Figure 2.3**.[209]

Concerning the c-ZrO_2, it typically exhibits an intensive asymmetric broadband mode centred at around 600 cm^{-1} (F_{2g} vibrational mode)[210], owing to a disordered oxygen sub-lattice.[206] Besides, this band position might vary slightly when dopants are used.[210] As the Ca amount increases to 7 and 10 mol.%, the cubic phase appears (mixtures of tetragonal and cubic phases). Nevertheless, a smoother A_{1g} band in the 10 mol.% Ca material suggests a higher prevalence of the cubic phase (dominant phase). According to the literature, the Raman spectra of Y_2O_3 doped c-ZrO_2 present a wide-ranging band between 530-670 cm^{-1}, as well as a high-background profile[211], and so the results suggest the presence and further stabilisation of the cubic phase for higher Ca concentrations, especially for the 10 mol.% Ca nanopowder.

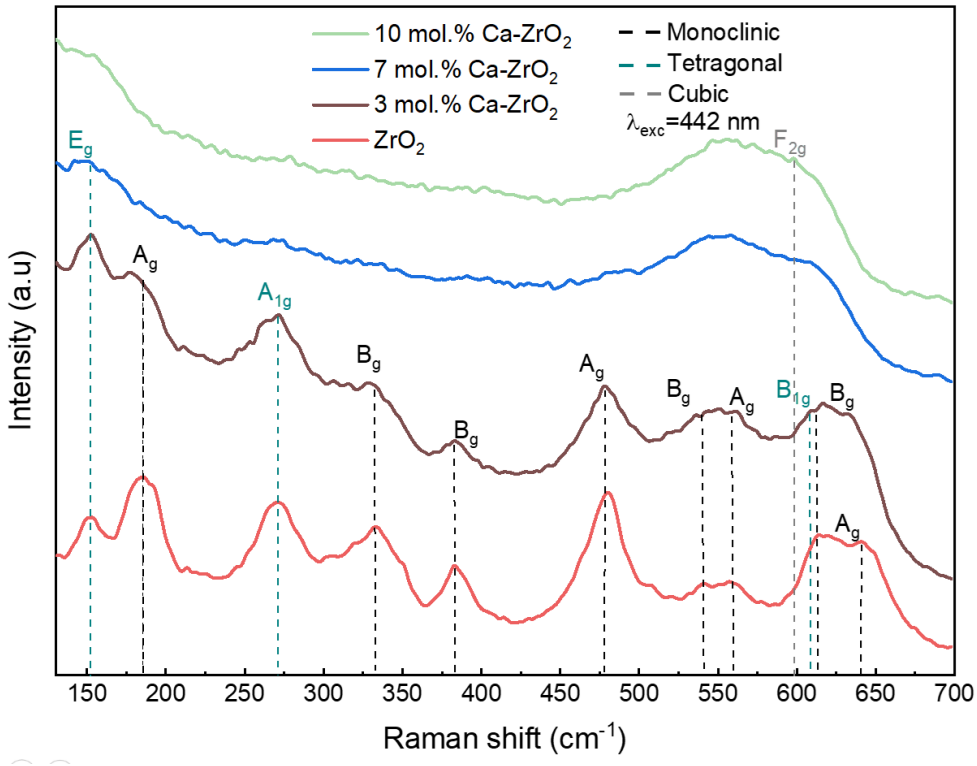

Figure 2.3: Raman spectra of the synthesised nanopowders. ZrO_2 nanopowders without and with different amounts of Ca (3,7 and 10 mol.%). The black, green and grey vertical dash lines represent the expected Raman shift for the monoclinic, tetragonal and cubic ZrO_2, respectively.

2.4.3 STEM analysis

STEM analyses were carried out for all ZrO_2 nanopowders and it was evident that Ca had a drastic impact on the structure of the ZrO_2 nanoparticles. From **Figure 2.4**, the presence of heterogeneous nanoparticles formed during microwave synthesis without Ca is evident (irregular-shaped, square, elongated and quasi-spherical nanoparticles). The average particle size was 8.26 ± 1.95 nm, and abnormally large nanoparticles were also observed (**Figure 2.4(a)**), in agreement with an analogous study.[206] XRD and Raman spectroscopy analyses confirmed the presence of both tetragonal and monoclinic phases, which was further corroborated by the STEM results using high-angle annular dark-field (HAADF) imaging. The Zr atomic columns are clearly visible in the HAADF image (**Figure 2.4(b)**). From the Zr atomic columns, it can be measured a lattice spacing of 2.9 Å that perfectly matches the (011) and (101) atomic planes of the tetragonal phase. Observed along the $[\bar{1}\bar{1}1]$ zone axis, it is clear from the fast Fourier transform (FFT) pattern that the angle between (011) and (101) is ~70º, in accordance with the theoretical value reported for pure crystalline t-ZrO_2 (ICDD 00-050-1089).

When Ca was added (3 mol.%Ca-ZrO_2 nanopowder), more uniform nanoparticles were crystallised, resulting in square nanoparticles, some with round corners (**Figures 2.5(a) and 2.5(b)**). The average particle size was 8.02 ± 1.86 nm, and the particle size distribution is presented in **Figure 2.5(a)**. A lattice spacing of 2.9 Å was measured, as in the case of the pure ZrO_2 nanoparticle, which

perfectly matches the (011) and (101) atomic planes of the tetragonal phase. It was observed along the $[\bar{1}\bar{1}1]$ zone axis an angle between both planes of ~71º, as measured by the FFT pattern in **Figure 2.5(c)** which perfectly matches the tetragonal phase. For this condition, the monoclinic phase was also detected (**Figures 2.2 and 2.3**), however, tetragonal nanoparticles were predominantly observed during STEM analysis.

Furthermore, by increasing the Ca amount to 7 mol.%, it could be observed a great impact on the nanoparticles size, with smaller nanoparticles, presenting an average size of 6.83 ± 1.35 nm (**Figures 2.6(a) and 2.6(b)**). Square nanoparticles were observed, together with some well-faceted quasi-hexagonal ones, as observed in **Figure 2.6(d)**. Lattice spacings of 2.3 Å and 2.9 Å were also measured, matching the (111) and (011) atomic planes of the tetragonal phase, respectively. Observed along the [211] zone axis, it is clear from FFT patterns that the angles between $(\bar{1}11)$ and $(01\bar{1})$ is ~74º, confirming the theoretical values reported for the tetragonal phase (**Figure 2.6(c)**). **Figure 2.6(d)** does not clearly reveal the presence of structural defects, *i.e.*, steps or absence of atoms. Nevertheless, such defects are usually present in high-index surfaces for other metal oxides, like TiO_2 [212] or WO_3 [213], and could be expected in the observed {102} exposed facets. Although such defects in ZrO_2 high-index surfaces have not been imaged at the atomic level, the formation of structural defects in ZrO_2 has been widely observed.[214–218]

As demonstrated by the Raman results (**Figure 2.3**), the cubic phase was present at 7 and 10 mol.% of Ca. At 7 mol.% of Ca, the nanoparticles exhibited a minor presence of the tetragonal phase, which vanished at 10 mol.% of Ca. Moreover, for this 10 mol.% of Ca nanopowder, the synthesised nanoparticles were smaller, with an average size of 6.24 ± 0.96 nm, and with the most uniform distribution among the investigated nanopowders (detected nanoparticles from 4 to 9 nm), as can be observed in **Figure 2.7(a)**. Square nanoparticles with angled/curved corners were observed (**Figures 2.7(a) and 2.7(b)**). A single nanoparticle was analysed in **Figure 2.7(b)**, and from its FFT pattern, which was observed along the [011] zone axis, it could be perfectly indexed to the cubic phase, with an angle between (002) and {111} planes of ~55º. Another nanoparticle (designed as B) was further investigated in **Figures 2.7(c) and 2.7(d)**, and it is clear the presence of zigzag edges and surface defects, *i.e.,* steps. The steps were observed at the {111} planes. Moreover, the nanoparticle exhibits both ordered and disordered regions. In the latter ones, the Zr atoms are misaligned along the [111] direction, causing the {111} lattice spacings to vary between 2.3 Å and 3.1 Å, compared to a predicted theoretical value of 2.9 Å for the {111} planes of the pure crystalline cubic phase (ICDD 00-049-1642). It was marked with white dashed lines to highlight the change in the distances between the neighbouring Zr atoms along the [111] directions. These lattice spacing variations also impacted the angles measured by the FFT patterns (observed along the [011] zone axis), which can be measured at a value of ~102.4º between the $(1\bar{1}1)$ and $(\bar{1}\bar{1}1)$, when it should be expected a theoretical value of ~109.5º for the cubic phase. This type of disarrangement of the Zr atoms was previously observed for films comprised c-ZrO_2 doped with Y_2O_3 (7 wt.%) grown on a polycrystalline alumina substrate via electron-beam physical vapor deposition at 1000 ºC.[191] Nevertheless, to the best of the author's knowledge, this is the first time that atomic structural defects, *i.e.,* steps and lattice displacements on the {111} planes have been observed on ~6

nm nanoparticles of c-ZrO_2 induced by the addition of Ca during microwave synthesis, without any post-treatment process.

EDS analysis was conducted to observe the distribution of Ca throughout the nanoparticles. **Figures 2.8(a) to 2.8(d)** show measurements of several nanoparticles, revealing that Ca is well distributed, along with Zr and O. No further impurities were detected by the EDS measurements. In the case of Ca, although it is identified within the nanoparticles, it appears that this element also tends to surround them, localised at the nanoparticles' surface. This assumption is further supported by **Figures 2.8(e) to 2.8(h)**, where a white square marks the area of a single nanoparticle. It can be speculated that Ca tends to segregate to the surface of the c-ZrO_2 nanoparticles. The segregation of stabiliser elements was previously reported by Feng *et al.*[219] In terms of Ca, the ionic radius is (1.14 Å[220]) larger than Zr, which may favour the segregation to the surface, releasing strain energy and making segregation energetically favourable.[219,220] Actually, in the present study, EDS analyses suggested the presence of Ca on the nanoparticle surface, which corroborates the theoretical studies for ZrO_2 with Ca as a stabiliser agent.[220,221]

Therefore, the present study suggests the presence of several surface defects induced by the amount of Ca and microwave irradiation. In fact, just with 10 mol.% of Ca, the surface defects were observed, indicating that there is a minimal amount of Ca to convert to cubic phase, but also to form the atomic-structural defects. Microwave irradiation could have also played a role in the formation of defects since this synthesis route is known to induce defects in metal oxides.[222–225] Nevertheless, as the microwave parameters were identical to all conditions investigated, the defects observed in the 10 mol.%Ca-ZrO_2 nanoparticles are expected to mostly result from the amount of Ca present.

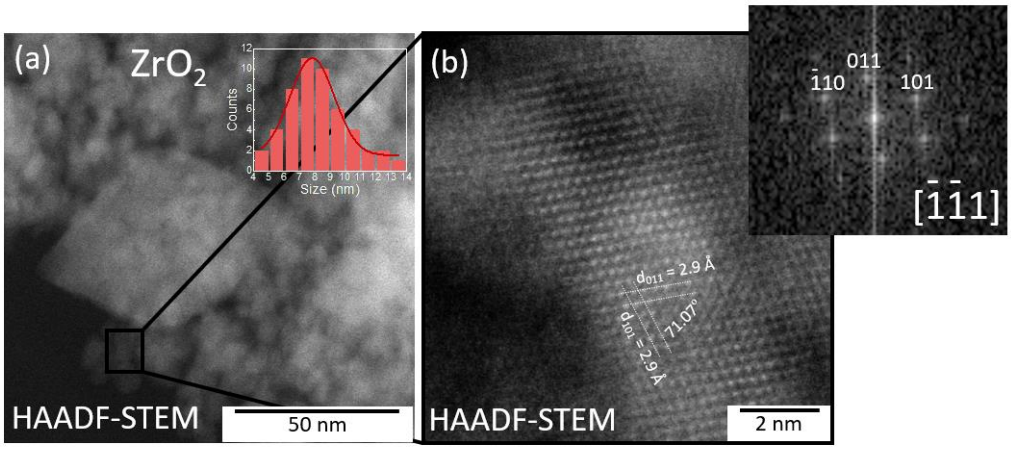

Figure 2.4: STEM analysis of the ZrO_2 nanopowder. (a) HAADF-STEM image of the ZrO_2 nanoparticles without calcium together with the nanoparticle size distribution. **(b)** HAADF-STEM image of an elongated ZrO_2 nanoparticle, together with its FFT image

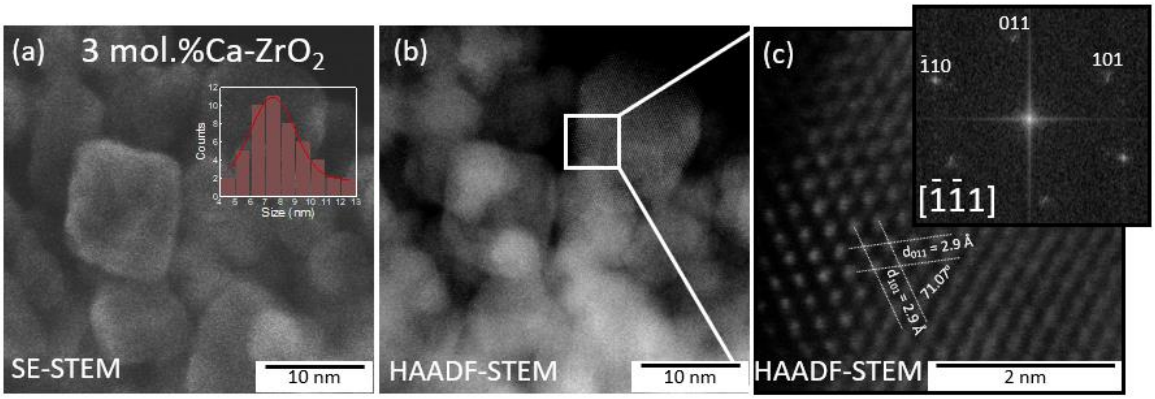

Figure 2.5: STEM analysis of the 3 mol.%Ca-ZrO_2. (a) Secondary electron (SE-STEM) and **(b)** HAADF-STEM image of the 3 mol.%Ca-ZrO_2 nanopowder together with the nanoparticle size distribution. **(c)** Magnified HAADF-STEM image of the indicated area in **(b)**, together with its FFT image observed along the $[\bar{1}\bar{1}1]$ zone axis.

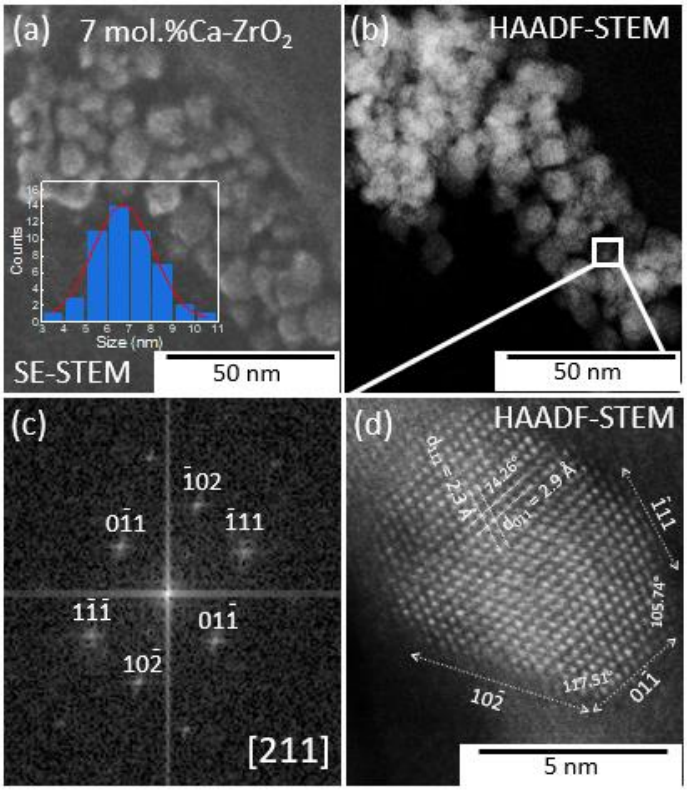

Figure 2.6: STEM analysis of the 7mol.%Ca-ZrO_2 nanopowder. (a) SE-STEM and **(b)** HAADF-STEM image of the 7 mol.%Ca-ZrO_2 nanopowder together with its nanoparticle size distribution. **(c)** and **(d)** FFT pattern and magnified HAADF-STEM image of the indicated area in (b).

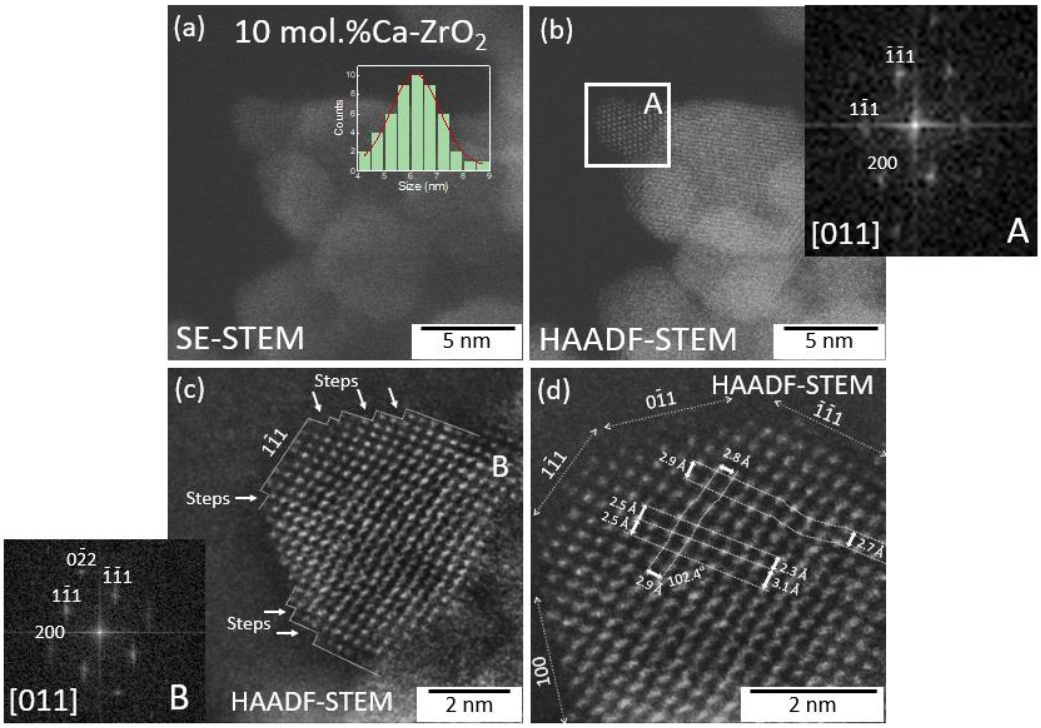

Figure 2.7: STEM analysis of the 7mol.%Ca-ZrO_2 nanopowder. (a) SE-STEM and **(b)** HAADF-STEM image of the 10 mol.%Ca-ZrO_2 nanopowder together with its nanoparticle size distribution and FFT pattern of the nanoparticle indicated as A. **(c)** and **(d)** HAADF-STEM image of an individual nanoparticle together with its FFT pattern (nanoparticle indicated as B).

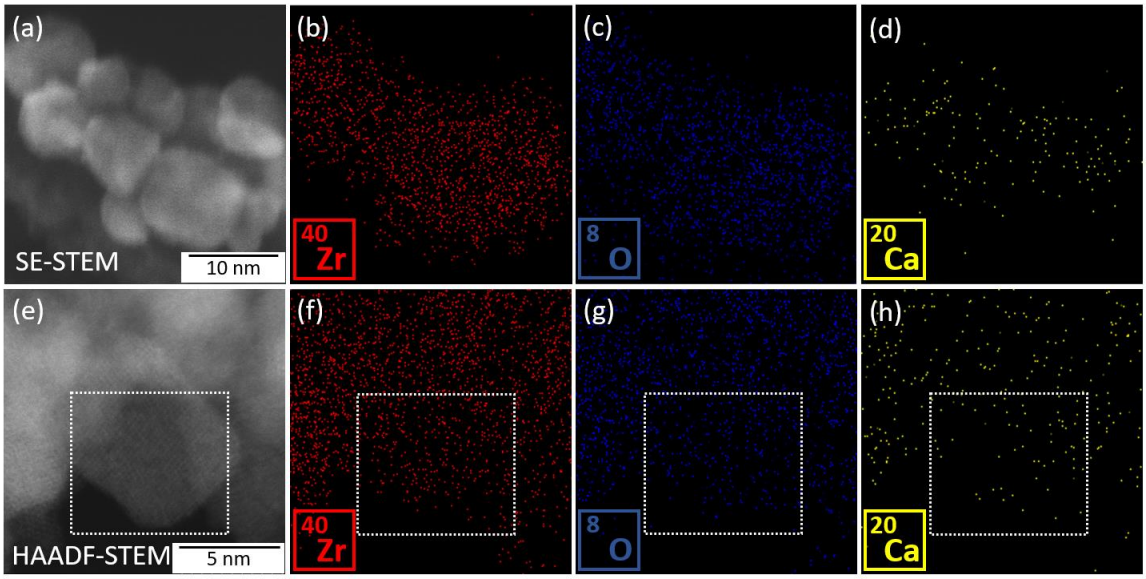

Figure 2.8: EDS analysis of the 10 mol.%Ca-ZrO_2 nanopowder. **(a)** SE-STEM and **(e)** HAADF-STEM images of the 10 mol.%Ca-ZrO_2 nanoparticles. Corresponding EDS maps of Zr **(b)** and **(f)**, O **(c)** and **(g)**, and Ca **(d)** and **(h)**. The white square determines the area of an individual nanoparticle

2.4.4 BET analysis

The BET analysis was performed to determine the specific surface area of both ZrO_2 and 10 mol.%Ca-ZrO_2 nanopowders. The results demonstrate that the addition of Ca significantly enhances the specific surface area of the nanopowders (**Table 2.1**). This result is in alignment with the nanoparticle sizes' decrease observed in **Figure 2.4(a)** and **Figure 2.7(a)**, showing a nanoparticle size of 8.26 ± 1.95 nm for the ZrO_2 without Ca (abnormal larger nanoparticles were also observed), and 6.24 ± 0.96 nm for the 10 mol.%Ca-ZrO_2 condition. This inverse correlation between nanoparticle size and specific surface area is expected and largely reported in the literature. [226–231]

When it comes to the ZrO_2 phases present, the results from the XRD, Raman spectroscopy and STEM measurements revealed the presence of both monoclinic and tetragonal phases in the ZrO_2 nanopowder, while the cubic phase was revealed as the amount of Ca increased. Therefore, the measured surface area of 98.034 m^2/g for the synthesised ZrO_2 without Ca is in agreement with previous studies, which reported a specific surface area of 83.4 m^2/g for m-ZrO_2 [232] and 100 m^2/g for t-ZrO_2 nanoparticles[233], both synthesised considering hydrothermal methods. In another study, c-ZrO_2 nanoparticles were synthesised using a hydrothermal method and stabilised with scandia, with a crystallite size of 6 nm. The measured specific surface area was 157 m^2/g [234], which is similar to the value of 151.62 m^2/g, obtained in this study, for the 10 mol.%Ca-ZrO_2 nanopowder. Some studies highlighted the enhanced specific surface area of defective nanoparticles [231,235], and as structural defects were observed for the 10 mol.%Ca-ZrO_2 nanopowder, some contribution of these defects can be expected for the enhanced surface area. Thus, the stabilisation of c-ZrO_2 resulted in smaller nanoparticle sizes and the formation of defects, thereby increasing the specific surface area of the 10 mol.%Ca-ZrO_2 nanopowder.

Table 2.1: Estimated BET surface area. Estimated value for the ZrO_2 and 10 mol.%Ca-ZrO_2 nanopowders.

Nanopowder	Surface Area (m^2/g)
ZrO_2	98.03
10 mol.%Ca-ZrO_2	151.62

2.5 Conclusion

This study introduced a sustainable approach to synthesising ZrO_2 nanoparticles using a Ca-stabilised microwave irradiation process. A fast (1h), low temperature (230 ºC) and water-based microwave method was considered, without any post-synthesis treatment. By incorporating different amounts of Ca (3, 7, and 10 mol.%) into the microwave synthesis, distinct ZrO_2 crystalline phases were obtained, up to the dominant cubic phase crystallisation with 10 mol.% of Ca, as demonstrated by the Raman spectroscopy results.

STEM analyses revealed that the stabilisation of the cubic phase for the 10 mol.%Ca-ZrO_2 nanopowder resulted in smaller nanoparticles (6.24 ± 0.96 nm) with uniform size and shape, compared to other ZrO_2 nanoparticles produced in this study. Additionally, the 10 mol.% Ca-ZrO_2 sample exhibited surface step defects and atomic disarrangements in its nanostructures. Moreover, the EDS analysis revealed that Ca is properly distributed and that no impurities were found, also suggesting a potential segregation to the surface of the c-ZrO_2 nanoparticles.

BET measurements further highlighted the influence of cubic phase stabilisation on the specific surface area, demonstrating a higher surface area for the 10 mol.%Ca-ZrO_2 nanopowder. This result is in alignment with the smaller nanoparticle size and the presence of defects leading to an enhancement in the specific surface area for the aforementioned nanopowder.

In conclusion, this study reports for the first time the stabilisation of defective c-ZrO_2 nanoparticles using Ca as a stabiliser through a one-step microwave process without any calcination treatment. This approach offers a more sustainable and economical method for ZrO_2 phase stabilisation, utilising Ca's availability, biocompatibility and bioactivity to enhance its efficiency for target applications, such as for TE purposes. Additionally, this approach demonstrates potential for the development of more environmentally sustainable nanoparticle synthesis methodologies.

Chapter 3: Incorporation of Ca-Stabilised Cubic ZrO_2 Nanoparticles into Shape Memory Alginate Scaffolds

3.1 Chapter Overview

In this chapter, the newly synthesised c-ZrO_2 nanoparticles (10 mol.%Ca-ZrO_2) were incorporated into shape memory alginate scaffolds, produced by solvent casting, using a soaking method. Two main groups were systematically investigated and compared to address the impact of nanoparticle incorporation: pristine alginate scaffolds and alginate scaffolds functionalised with c-ZrO_2 nanoparticles. Also, EDS analysis was employed to evaluate the distribution of c-ZrO_2 throughout the scaffolds and to detect any impurities. Additionally, gravimetric methods were used to determine the porosity, water uptake and weight loss. The impact of nanoparticle addition on the scaffolds' mechanical performance was evaluated through compression testing and subsequent Young's modulus determination. For biological characterisation preliminary *in vitro* cytotoxic experiments were carried out using (3-(4,5-Dimethylthiazol-2-yl)-2,5-diphenyltetrazolium bromide (MTT) assays. The proliferation of human BM-MSCs was monitored using the AlamarBlue assay over seven days. Lastly, following the cell culture, the morphology of the cell aggregates was studied using scanning electron microscopy (SEM) imaging, confocal and fluorescence microscopy The aspect ratio of the cell aggregates was also calculated

3.2 Introduction

Failure of tissues and organs resulting from illness, trauma or developmental defects has raised major issues, significantly affecting both healthcare and the economy.[236] As a result, TE aims to overcome the limited regeneration capacity of the human body instead of focusing on the replacement or reparation of the damaged tissues.[237] Therefore, biomaterials have been utilised to produce scaffolds with suitable structures to conduct cell proliferation and differentiation into effective tissues.[238,239]

Natural polymers have been widely used due to their biocompatibility, biodegradability and ability to mimic the ECM.[177] Alginate is a polysaccharide primarily present in the cell walls of certain types of brown seaweeds.[240] Additionally, alginate and its derivatives are bioinert and exhibit anionic and hydrophilic characteristics, being composed of (1,4) linked β-D-mannuronic and α-L-guluronic acids in a pyranose conformation and organised in blocks. This results in a large variety of structures, molecular weights and physicochemical properties.[241,242] Moreover, alginate scaffolds can be featured with shape memory properties, thus having the capability to revert to their original form upon rehydration, enabling them to fill in defects or conform to irregularities.[178,243,244] Their utilisation has already been previously reported for osteochondral[178,245,246] and periodontal[247,248] TE applications. In addition to exhibiting shape memory properties via covalent crosslinking through carbodiimide chemistry, alginate scaffolds can also undergo architectural modifications to mimic native tissue structures. Therefore, these highly porous scaffolds can be designed to exhibit anisotropic properties[178]. Anisotropic scaffolds have been developed for the periodontium[249,250] and osteochondral tissue[178,251], with the explicit aim of replicating certain structural elements inherent to these tissues. Despite their numerous advantages,

natural polymers often exhibit poor mechanical properties, which negatively affects their application for TE purposes.[23,179]

As the research for novel advanced biomaterials intensifies, nanomaterials such as ZrO_2 nanoparticles are being further explored to enhance scaffold performance in load-bearing environments.[34,46,81,238,252,253] ZrO_2 materials exhibit excellent biocompatibility, bio-inertness, high stability, antimicrobial activity[254], osteointegration ability[255] and potential to promote osteogenic differentiation, fostering an osteoinductive environment paramount for bone development.[83–85] The intricacy of mechanical forces applied to the periodontal tissues[180] and osteochondral tissues [256,257] during, respectively mastication and joint movement highlights the necessity for engineered bone tissues to endure substantial biomechanical stress. The incorporation of ZrO_2 nanoparticles into natural polymeric-based scaffolds has already been described in the literature.[71,258,259] More specifically, the functionalisation of alginate-based scaffolds with these nanoparticles has proven recently to induce a more regulated degradation, good cell viability and controlled interconnected porous structure with improved mechanical properties.[80,260,261] Moreover, as previously mentioned, Ca can be used as a stabiliser element for ZrO_2 nanoparticles.[262,263] Ca is biocompatible and naturally present in the human body[264]. Also, there is evidence that Ca may influence MSCs differentiation enhancing the expression of genes related to osteogenic differentiation[265,266] Furthermore, Ca positively affects biomineralisation, essential for bone development and strength .[85,267–269]

This chapter aims to preliminarily explore how the integration of the newly synthesised 10% mol.%Ca-ZrO_2 nanoparticles into shape memory alginate scaffolds enhance their osteoinductive potential for osteochondral and periodontal TE purposes, particularly for subchondral and alveolar bone regeneration. In addition, studies reporting the application of nano-cubic ZrO_2 in TE are lacking in the literature.[83,97,186] Moreover, not only the utilisation of Ca as a stabiliser allows a more cost-effective and eco-friendly synthesis but it also takes advantage of Ca's natural abundance, bioactivity and biocompatibility.[198] This opens new avenues for osteochondral and periodontal regeneration strategies.

3.3 Materials and Methods

3.3.1 Scaffolds preparation

The alginate scaffolds were produced by solvent casting, based on previous work by *Almeida et al* [178]. After that, the scaffolds were directionally frozen and later freeze-dried. Two main groups were prepared: pristine scaffolds and scaffolds coated with 10 mol.%Ca-ZrO_2 nanoparticles (**Figure 3.1**). To ensure clarity, the label "Alginate" will be used for the unmodified shape-memory scaffolds in the graph legends. Conversely, the scaffolds treated with 10 mol.%Ca-ZrO_2 nanoparticles will be identified as "Alginate + c-ZrO_2"

3.3.1.1 Shape-memory alginate scaffolds synthesis

Firstly, 0.1 M of 2-(N-Morpholino) ethanesulfonic acid buffer (MES, ≥ 99%, CAS:4432-31-4, Sigma-Aldrich) and 0.2 M of sodium chloride (NaCl, ≥99.5%, CAS:7647-14-5, PanReac AppliChem) were added in distilled water. Then, sodium alginate (COO^-, CAS:9005-38-3, Sigma-Aldrich) was dissolved to a final concentration of 4.5%(w/v) for 3 hours. After, solutions of 1-ethyl-3-dimethy aminopropyl carbodiimide (EDAC, CAS: 25952-53-8, Sigma-Aldrich) and N-Hydroxy-succinimide (NHS, ≥ 97.5%, CAS:6066-82-6; Sigma-Aldrich) were homogenised with the polymer solution during a few minutes to a final molar ratio of 2:1:2 EDAC: NHS: COO^-. Further, adipic acid dihydrazide (AAD, ≥ 98%, CAS: 1071-93-8, Sigma-Aldrich) was added in the form of an aqueous solution to a ratio of 45% compared to alginate ($n_{NH2}/_{COOH}$). Then the solution was rapidly homogenised and placed into a petri dish, and the crosslinking reaction occurred overnight at RT. The obtained hydrogel was washed with a 0.1 M calcium chloride aqueous solution ($CaCl_2$, ≥ 97%, CAS: 10043-52, Fluka) to promote an extra ionic crosslinking in an orbital shaker for 2 hours. Posteriorly, the hydrogel was washed several times with distilled water in an orbital shaker for 48 hours. Finally, after the washing steps, the hydrogel was cut into small pieces with the desired size.

3.3.1.2 Directional freezing and freeze-drying

Basically, the previously cut alginate scaffolds were vertically placed on a stainless-steel plate cooled with liquid nitrogen, until frozen. After, the samples were frozen at -80ºC. Finally, the frozen samples were freeze-dried in a FreeZone 4.5 Liter (Labconco, Kansas, USA).

3.3.1.3 Inclusion of 10 mol.%Ca-ZrO_2 nanoparticles into the scaffolds

A soaking technique was employed to functionalise the scaffolds with the nanoparticles, utilising PEG to prevent nanoparticle aggregation. Briefly, a solution of 0.2 mg/ml of PEG 35000 ($H(OCH_2CH_2)_nOH$, CAS: 25322-68-3, Sigma-Aldrich) was dissolved in distilled water over 24 hours. After, 1.8 ml of this PEG solution was mixed with 3 ml of a solution containing 0.25% ($w/v_{scaffold}$) of 10 mol.%Ca-ZrO_2 nanoparticles. Before mixing, the nanoparticles were dispersed in an ultrasonic bath for 30 minutes to ensure even distribution. The mixture of PEG and c-ZrO_2 was then stirred continuously for 6 hours at 50°C. Then, the final solution combining both the polymer and the nanoparticles, was used to coat the freeze-dried alginate scaffolds. The coating was tailored according to the volume and dimensions of the scaffolds, with a precise single droplet administered to each scaffold.

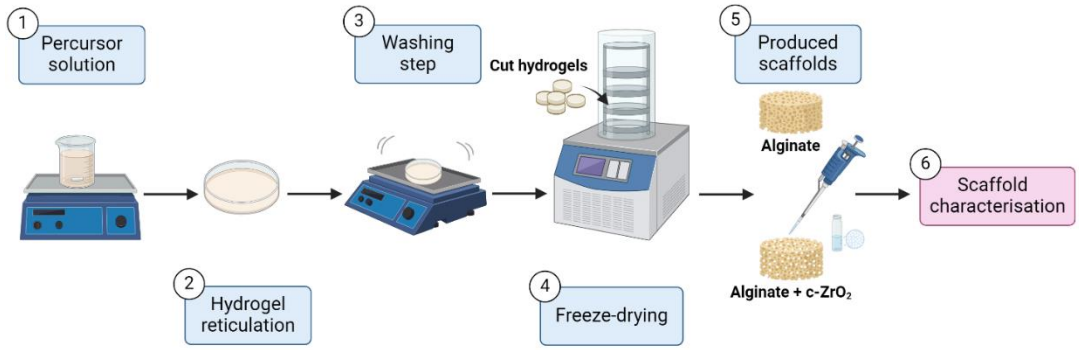

Figure 3.1: Overview of scaffold preparation via solvent casting. Key experimental steps are illustrated, including c-ZrO_2 incorporation through the soaking method and subsequent characterisation of both scaffold types. Image created using BioRender (https://www.biorender.com/)

3.3.2. Scaffolds Characterisation

3.3.2.1 Morphological characterisation

The scaffolds were imaged using Hitachi Regulus 8220 field-emission SEM (Hitachi, Tokyo, Japan) microscope equipped with an EDS detector from Oxford instruments, using an accelerating voltage of 5 kV. The incorporation of the nanoparticles into the scaffolds was assessed using EDS detector. Before imaging the scaffolds were coated with a gold/palladium layer. Moreover, 15 pores of each scaffold type were measured using ImageJ Fiji (Version 2.9.0) to determine pore size.

The scaffolds' porosities were calculated from the mass and the volume of each scaffold using **Equation 3.1**,[270,271] where $\rho_{apparent}$ is calculated from the weighted dry mass and the volume of each scaffold, and $\rho_{material}$ represents the literature density of alginic acid sodium salt, which is 1.59 g/cm^3.[272] This assay was conducted in triplicate.

$$P\ (\%) = 100 \times \left(1 - \frac{\rho_{apparent}}{\rho_{material}}\right) \quad (3.1)$$

3.3.2 2 Water uptake

The water uptake of the scaffolds was determined for each scaffold using **Equation 3.2**. Initially, the freeze-dried scaffolds (W_0) were pre-weighted and then submerged in phosphate-buffered saline (PBS) for seven days. Afterwards, the samples were collected and the excess of PBS was removed. Subsequently, the scaffolds were reweighted again (W_S) at different time points: 10 and 30 minutes, 2 hours, 3 hours, around 10 hours, and daily thereafter for 1, 2, 3, 6, and 7 days. This assay was conducted in quintuplicate.

$$Water\ uptake\ (\%) = \frac{W_s - W_0}{W_0} \times 100 \quad (3.2)$$

3.3.2.3 Weight loss assessment

The degradation was monitored by immersing the scaffolds in PBS. For each scaffold, the remaining scaffold (%), was calculated using **Equation 3.3**, where W_0 represents the initial weight of the freeze-dried scaffold. The mass degradation was evaluated across different time points: 7,14 and 21 days. On these specific days, the scaffolds were collected, allowed to air dry, and subsequently reweighed to obtain (W_f) for each. Afterwards, they were once again submerged in PBS for continued assessment. This assay was performed in quintuplicate.

$$Remaining\ mass\ of\ the\ scaffold\ (\%) = 100 - \left(\frac{W_0 - W_f}{W_0} \times 100\right) \quad (3.3)$$

3.3.2.4 Mechanical analysis

Compression tests were carried out at RT using a Model UV-200-01 mechanical tester (CellScale, Ontário, Canada) equipped with a load cell of 10 N. The two produced scaffold types were tested: pristine scaffolds (19 mm diameter, 2-3 mm height) and scaffolds with c-ZrO_2 nanoparticles (15 mm diameter, 1-1.5 mm height). The compression tests were conducted at a displacement rate of 1 mm/min. The samples subjected to the compression test did not collapse. Young's modulus was calculated from 0-20 % initial linear region slopes of the stress-strain curves, according to **Equation 3.4** This essay was performed in triplicate on wet samples that had been left in PBS for 24 hours before testing.

$$E\ (kPa) = \frac{\sigma}{\varepsilon} \quad (3.4)$$

3.3.3 Biological characterisation

3.3.3.1 Cell culture and media

The biological experiments were conducted using two different cell lines: NIH 3T3 fibroblast cells (93061524, Sigma - Aldrich) derived from a NIH Swiss mouse embryo and human BM-MSCs from a cell bank disposable at the Stem Cell Engineering Research Group, Institute for Bioengineering and Biosciences (iBB) at Instituto Superior Técnico (IST).

Fibroblast cells were cultured in Dulbecco's modified Eagle Medium (DMEM, Cat #D5796, Sigma-Adrich) supplemented with 10% (v/v) fetal bovine serum (FBS, Cat#12133C, Sigma-Aldrich), 2.5 µg/ml fungizone (Cat #A2942, Sigma-Aldrich) and a mixture of 100U/mL penicillin and 100µg/mL streptomycin (PenStrep, Cat #P4333, Sigma-Aldrich).

The human BM-MSCs were formerly isolated following protocols that had been previously established at iBB-IST. Bone marrow aspirates (46-year-old male) were acquired through collaboration agreements between iBB-IST and Centro Clínico da GNR, Lisboa. The Ethics Committee of the relevant clinical institution approved the acquisition of all human samples from healthy donors, which were obtained after written informed consent was obtained following the Directive 2004/23/EC of the European Parliament and of the Council of March 31, 2004, on setting standards of quality and safety for the donation, procurement, testing, processing, preservation, storage, and distribution of human tissues and cells (Portuguese Law 22/2007, June 29). [273] Until their utilisation cells were stored frozen. For the cell assays the human BM-MSCs were previously thawed and cultured in low-glucose DMEM (Cat # 31600091, Thermo Fisher) supplemented with 10% (v/v) FBS qualified for MSCs (Cat# 12662029, Thermo Fisher) and 1% antibiotic-antimycotic (Anti-Anti solution, Cat# 15240062, Thermo Fisher).

3.3.3.2 Cytotoxicity assessment

To evaluate the cytotoxic potential of the developed scaffolds MTT assays were performed. Before the essay, the scaffolds underwent sterilisation through three sequential baths in 70% (v/v) ethanol, each of five minutes, followed by a 15-minute exposure to ultraviolet light within a laminar flow chamber.

Firstly, extracts of the two different scaffold groups were prepared, utilising the fibroblast cells culture media outlined in section 3.3.3.1 as the extraction vehicle. The extraction ratio (scaffold surface area/ extraction vehicle volume) was 3 cm^2/mL as reported in ISO 10993-12[274] for samples exceeding 1 mm thickness. After, the samples were kept at 37 °C, 5 % CO_2 incubator for 24 hours.

Simultaneously, NIH 3T3 fibroblast cells (P2-P15) were seeded in 96-well plates at a concentration of 1 x 10^5 per well in culture media (200µL) and incubated at 37 °C, 5 % CO_2 for 24 h. After, the cell culture medium was discarded and replaced with four different concentrations of the test

sample extracts diluted in culture media (200 µL): 100% (v/v), 50 %(v/v), 25% (v/v) and 12.5% (v/v). At the same time, 10% (v/v) dimethyl sulfoxide (DMSO, Cat #D5879, Sigma-Aldrich) (200 µL) was used as a positive control. The extract dilutions and the positive control were incubated at 37 °C, 5 % CO_2 for another 24 hours. Post incubation, the culture medium was once more removed and the wells were washed with PBS (100 µL). Then, the MTT solution (Cat #M5655, Sigma-Aldrich) of 0.5 mg/mL prepared in culture media without FBS, was added to each well, and the plates were placed in an incubator (37 °C, 5 % CO_2) for 3h. Following this, a solution (200 µL) composed of 4 mM HCl, 0.1% IGEPAL CA630 (CAS: 9036-19-5, Sigma-Aldrich) in isopropanol was added to solubilise the crystals by up and down. Finally, the plates were agitated on an orbital shaker for 3h, after which the absorbance was measured at 565 nm in an Infinite 200 Pro plate reader (TECAN, Männedorf, Switzerland). The cell viability was calculated using **Equation 3.5**. This assay was conducted in triplicate, following the standard set forth in ISO 109993-5.[275]

$$Cell\ Viability\ (\%) = 100 \times \frac{Abs_{565} Dilution\ extract\ sample}{Abs_{565} Cells\ with\ medium} \qquad (3.5)$$

3.3.3.3 Proliferation experiment

Before the experiments, the scaffolds were immersed in PBS overnight. Subsequently, they were coated with gelatine from porcine skin (gel strength type A, CAS 9000-70-8, Sigma-Aldrich), and prepared as a 5% (w/v in sterile distilled water) solution to ensure cell adhesion. The scaffolds underwent sterilisation through three washes using a PBS solution enriched with 1% antibiotic-antimycotic (Anti-Anti solution, Cat# 15240062, Thermo Fisher). Following sterilisation, the scaffolds were immersed in culture media for one hour within an incubator set at 37 °C and 5% CO_2. After this period, the culture media was discarded, and the scaffolds were kept for another hour under the same incubator conditions. Then, the human BM-MSCs were seeded (P6) onto the scaffolds at a density of 1 x 10^5 cells per scaffold without culture media. To facilitate initial cell adhesion, these cell-seeded scaffolds were returned to the incubator under the same conditions. Subsequently, culture media was introduced to the wells containing the constructs, and this media was replaced every 3 to 4 days. To ensure clarity and readability even after the cell-seeding the designation scaffold will be further used for both experimental groups.

The proliferation of human BM-MSCs on the scaffolds was assessed using the AlamarBlue assay under the manufacturer's instructions. Briefly, the scaffolds were treated with a 10% (v/v in culture media) AlamarBlue solution (Cat #DAL1100, Thermo Fisher) (700 µL). Additionally, the solution was added to an empty well as a negative control. Following this, the plate was incubated in the dark under the same conditions. The fluorescence intensity was measured using an Infinite 200 Pro plate reader (TECAN, Männedorf, Switzerland) at an excitation/emission wavelength of 560/590 nm. For the two scaffold types, three independent scaffolds were seeded and tested, and acellular scaffolds were used as blanks. Besides, the fluorescence intensity was measured in triplicate for each tested sample and

the metabolic activity was calculated using **Equation 3.6** on days 1,4 and 7. The Fold increase was calculated on days 4 and 7 following **Equation 3.7**

$$Metabolic\ activity\ (a.u) = Abs_{560/590} Sample - blank \tag{3.6}$$

$$Fold\ increase\ = \frac{Metabolic\ activity\ _{Day\ x}}{Metabolic\ activity\ _{Day\ 1}} \tag{3.7}$$

3.3.3.4 Cell morphology analysis

To observe the morphology and phenotype of the human BM-MSCs after 7 days of cell culture and determine if the inclusion of the c-ZrO_2 nanoparticles affected cell adhesion and distribution, the samples were stained with 4,6-diamidino-2-phenylindole dihydrochloride (DAPI, CAS: 28718-90-3, Sigma-Aldrich) and Phalloidin-TRIC (Cat# P1951, Sigma-Aldrich) after 7 days of cell culture. Firstly, the samples were fixated in PBS with 4% (w/v) paraformaldehyde (PFA, CAS: 305525-89-4, Sigma-Aldrich) for 20 minutes and washed twice in PBS. Subsequently, the samples were permeabilised with 0.1% (v/v in PBS) Triton X-100 (CAS: 9002-93-1, Sigma-Aldrich) for 10 minutes, and washed with PBS. Afterwards, the samples were incubated in the dark (37 °C and 5% CO_2) with Phalloidin-TRIC (2 µg/mL in PBS) for 45 minutes and washed twice with PBS. Then, the samples were again incubated in the dark, but with DAPI (1.5 µg/mL in PBS) for 5 minutes, and washed twice with PBS. The fluorescence staining was imaged using an LSM 700 confocal Laser scanning microscope (Zeiss, Jena, Germany) to acquire z-stacks images with a magnification of 20x, and a BX51 fluorescence microscope (Olympus, Tokyo, Japan) with a magnification of 20x. The obtained data was processed using ImageJ Fiji (Version 2.9.0). Additionally, aspect ratio, a shape descriptor, was calculated, as the ratio between the sample's major axis and the minor axis of an elliptical fit, as depicted in **Equation 3.8**. The aspect ratio was determined using two images from the confocal microscope and two images from the fluorescence microscope of each cell-seeded scaffold type.

$$Aspect\ Ratio\ = \frac{Major\ axis}{Minor\ axis} \tag{3.8}$$

The cell morphology on the samples was also observed using a using Hitachi Regulus 8220 field-emission SEM (Hitachi, Tokyo, Japan) after 7 days of cell culture, using an accelerating voltage of 5 kV. The samples were previously fixed in 4% paraformaldehyde (w/v in PBS) (PFA, CAS: 305525-89-4, Sigma-Aldrich) and dehydrated via a series of five-minute ethanol baths of increasing concentrations (50%, 70%, 80%, 95%, 100% (v/v)). After completing the final bath, the ethanol was discarded, and the samples were immersed in fresh absolute ethanol overnight. After this, the samples were left to air-dry in a conventional oven. Prior to SEM imaging the samples were coated with a gold/palladium layer.

3.3.4 Statistical Analysis

The statistical analysis was performed using GraphPad Prism Software (Version 9.0.0). The results are presented as mean ± standard deviation (S.D.), and N refers to independent experiments. All the collected data was initially evaluated for normal distribution using the Shapiro-Wilk test, with a significance level set at $\alpha=0.05$. Statistical significance was evaluated using either a T-test or a Two-way ANOVA with subsequent application of Šidák test for multiple comparisons, based on the requirements of the data analysis. Statistical significance was considered at different levels of probability *$p<0.05$, **$p<0.01$, ***$p<0.001$ and ****$p<0.0001$. Results that did not show statistical significance when compared directly were denoted as not significant (ns).

3.4 Results and Discussion

3.4.1 Scaffolds characterisation

3.4.1.1 Morphological characterisation

The morphological analysis of the shape memory alginate scaffolds was performed to elucidate the comprehensive structure of the composites at a microscopic level. Furthermore, EDS analysis was employed to evaluate the incorporation of c-ZrO_2 nanoparticles via soaking. The SEM images depicted below (**Figure 3.2**) allow to observe that both scaffold types possess highly porous structures.

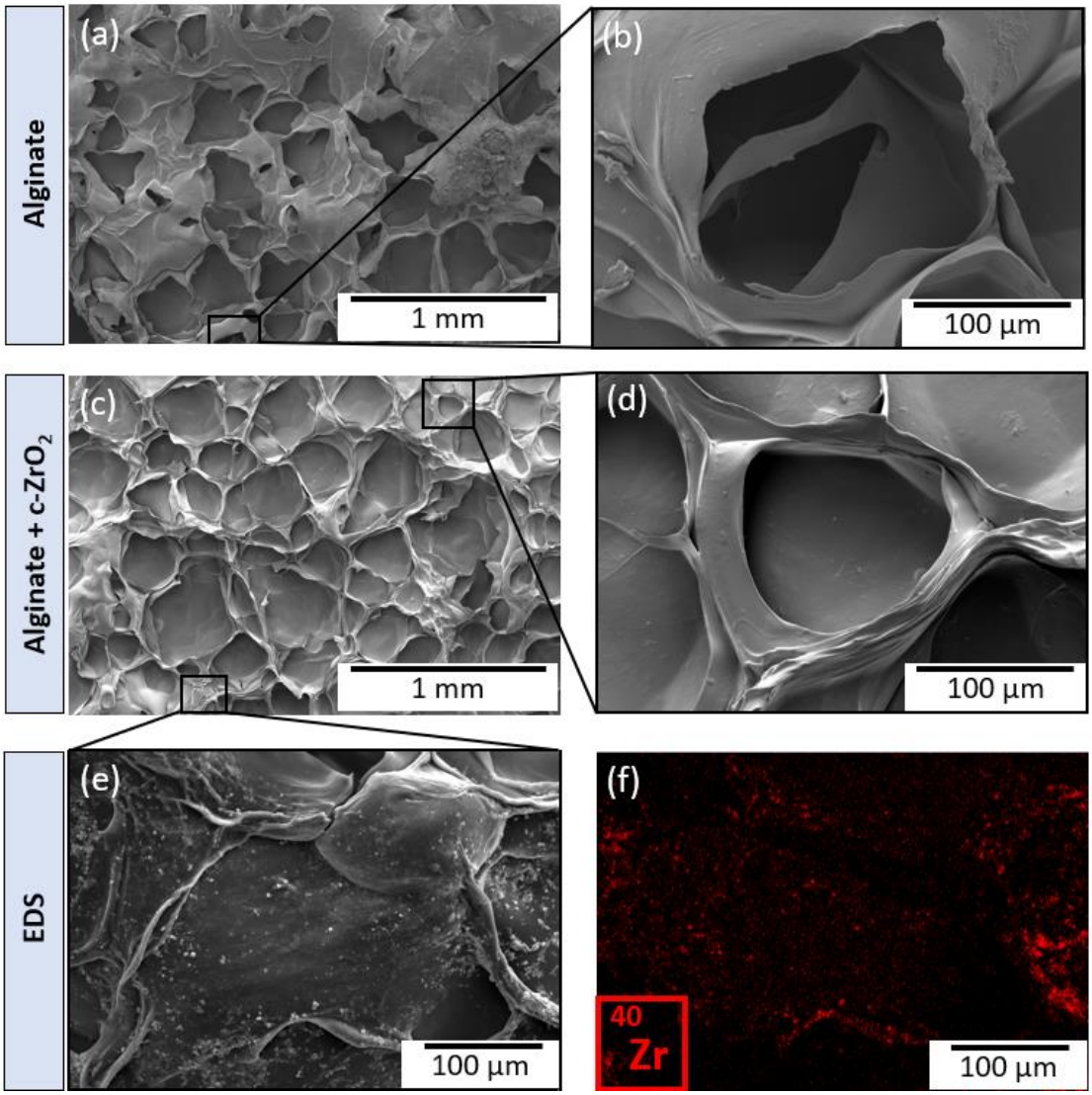

Figure 3.2: SEM morphological analysis of the scaffolds. (a) and **(b)** Alginate scaffold without nanoparticles. **(c)** and **(d)** Alginate scaffold functionalised with c-ZrO_2 nanoparticles. **(e)** and **(f)** EDS analysis of the alginate scaffold coated c-ZrO_2 nanoparticles. Scale bars represent 1 mm and 100 µm as indicated

Additionally, it was observable that the pristine alginate scaffold (**Figure 3.2(a) and 3.2(b)**) presented a smoother surface profile with fewer round-shaped pores compared to the alginate scaffold coated with c-ZrO_2 nanoparticles (**Figure 3.2(c) and 3.2(d)**). This distinction in surface roughness and pore format might be explained by inter-batch variability, a phenomenon frequently encountered in natural polymers such as alginate.[276]

Furthermore, the findings from EDS analysis (**Figure 3.2(e) and 3.2(f)**) confirm the successful deposition of the newly synthesised c-ZrO_2 nanoparticles onto the surface of the alginate scaffold via the applied soaking method. No additional impurities were detected. The presence of carbon and oxygen, shown in **Figure S1** (in the supplementary data) is related to the composition of the alginate polymer.[277]

Scaffold design is paramount for TE since scaffolds serve as structural support for the creation of engineering tissues that will mimic *in vivo* features.[278] Among these characteristics, mean pore size and porosity are intrinsically vital for establishing an appropriate microenvironment. Additionally, porosity significantly impacts the mechanical properties of scaffolds, typically a higher porosity is linked with reduced mechanical performance.[271,279] Optimal pore size and an interconnected network are essential to guarantee proper nutrient, growth factor delivery, oxygen diffusion and structural cues for proper cell proliferation.[280]

Regarding the scaffolds' porous structure, the mean pore size (**Figure 3.3(a)**) and the porosity (**Figure 3.3(b)**) of both scaffold types, with and without c-ZrO_2, were assessed. Based on **Figure 3.3(a)** it can be inferred that the incorporation of c-ZrO_2 nanoparticles did not result in a significant difference in the pore size for both scaffold groups, with a pore size of 289.64 ± 35.73 μm for the pristine alginate scaffold and a value of 286.44 ± 41.73 μm for the alginate scaffold functionalised with the nanoparticles, in accordance to the SEM imaging. Moreover, this tendency persisted, as there was no significant variation in porosity between the alginate scaffolds and the alginate scaffolds coated with the c-ZrO_2 nanoparticles. A slightly reduced value was obtained for the scaffolds with nanoparticles (87.43 ± 2.86 %) when compared to the pristine scaffolds (93.45 ± 1.58 %).

Regarding the field of osteochondral TE, a pore size between 100-300 μm[281] and a porosity between 70-90% are described as adequate for bone regeneration.[282] Similarly, regarding periodontal TE, alveolar bone regeneration studies mentioned a porosity range of 70-86%[283] and a pore size of 150-300 μm[284].The functionalisation of alginate scaffolds with c-ZrO_2 nanoparticles did not lead to a significant alteration in their porosity or pore size. However, the porosity of the modified scaffolds aligns marginally more closely with the literature values cited for the engineered development of the bone component in osteochondral and periodontal tissues.

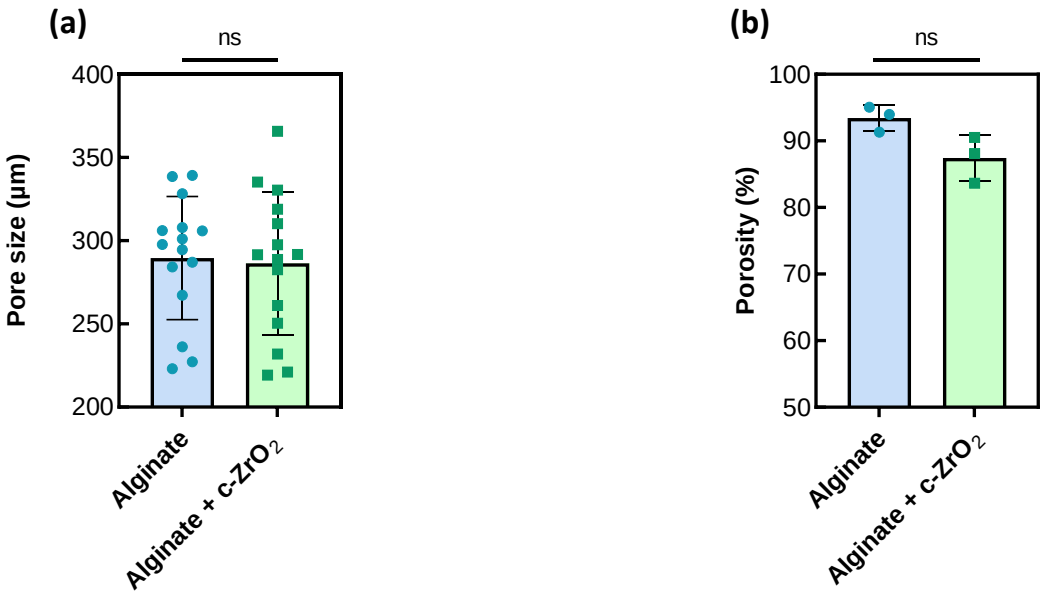

Figure 3.3: Determination of the pore size and porosity for the alginate scaffolds with and without c-ZrO_2 nanoparticles. (a) Determination of pore size for both scaffold types. T-test, ns (not significant), N=15. **(b)** Porosity assessment for both scaffold types. T-test, ns (not significant), N=3. All data presented as plot individual values, mean ± SD.

3.4.1.2 Water uptake

Evaluating the water uptake is crucial as it directly affects the scaffolds' capacity to absorb nutrients and metabolites, essential for supporting cell growth and tissue development. [17]

The results from **Figure 3.4** strongly suggest that the addition of even a small quantity of c-ZrO_2 nanoparticles to pristine alginate scaffolds had a significant impact on their water uptake. After seven days, the unmodified alginate scaffolds exhibited a water uptake of 2796.16 ± 135.74 %, while the alginate scaffolds with the c-ZrO_2 nanoparticles showed a notably lower water uptake of 1993.47 ± 68.25 %.

Due to its hydrophilic properties, alginate can be crosslinked to form a hydrogel, enabling it to absorb a considerable amount of water or other hydrophilic substances.[285] Despite the popularity of high-swelling composites, excessive water uptake can lead to rapid degradation of the scaffold structure and a significant reduction in mechanical strength. Therefore, customising the water uptake of scaffolds is vital to strike a balance between providing an inviting environment for cell growth and maintaining the structural integrity of the scaffold over time.[17] Similarly to the results shown in **Figure 3.4**, a study led by *Ghanbari et al*[252] also reported a decrease in the water uptake of an alginate-based hydrogel after the addiction of ZrO_2 nanoparticles, suggesting that the water uptake of the hydrogels can be adjusted by nanoparticles incorporation. Since the water uptake is largely influenced by the accessibility and presence of hydrophilic groups this phenomenon was possibly attributed to the interaction between the

ZrO_2 nanoparticles and the hydrogel matrix itself. The inclusion of c-ZrO_2 nanoparticles could have created some barrier effect, diminishing the accessible scaffold interface for direct media absorption.[17,286] Also, the slightly reduced porosity observed in scaffolds containing nanoparticles (as shown in **Figure 3.3(b)**) may have contributed to their decreased water uptake.[287] Besides, ZrO_2 nanoparticles, the incorporation of TiO_2 nanoparticles in alginate-based composites has also been described to induce a diminished water uptake.[288,289]

Given that higher water uptake remarkably compromise the mechanical properties of hydrogels[290], incorporating c-ZrO_2 nanoparticles has shown promise in reinforcing scaffolds for applications in load-bearing environments. This is particularly relevant for applications in osteochondral and periodontal tissues, especially in their bone component.

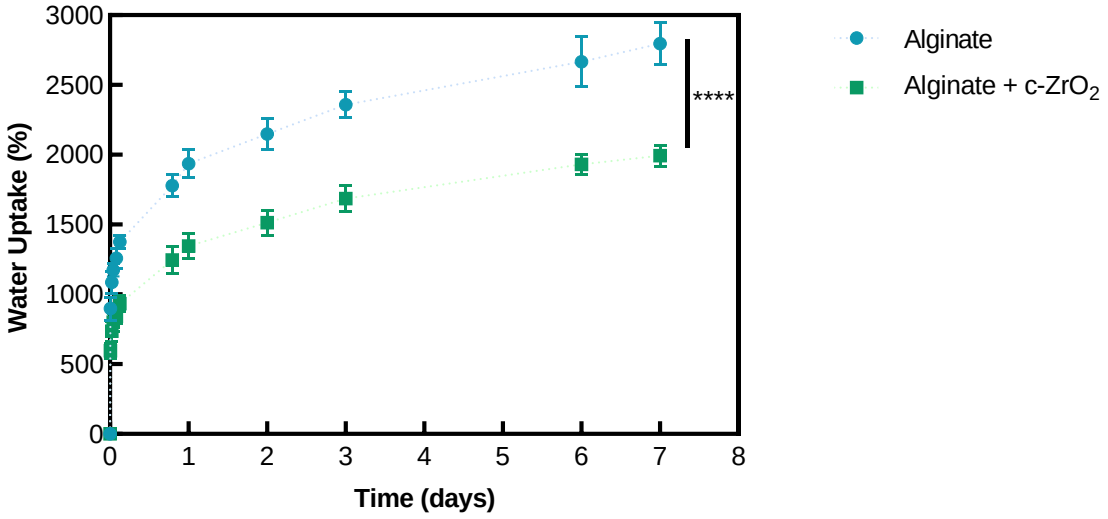

Figure 3.4: Water uptake of the alginate scaffolds with and without c-ZrO_2 nanoparticles over a seven-day period. Two-way ANOVA test, ****p<0.0001. All data presented as plot individual values, mean ± SD (N=5).

3.4.1.3 Weight loss assessment

The degradation of scaffolds over time was evaluated by monitoring the weight loss. **Figure 3.5** illustrates that there was no significant difference in the degradation behaviour between the unmodified alginate scaffolds and those functionalised with c-ZrO_2 nanoparticles. Following the 21-day experiment the pristine scaffolds retained 80.06 ± 1.68 % of their original weight whereas those reinforced with c-ZrO_2 nanoparticles maintained 80.36 ± 1.16% of their initial weight.

Ideally, polymer-based scaffolds must be capable of keeping their physical properties, mechanical performance and while also fostering an environment for cell growth and differentiation until full tissue or defect regeneration is achieved. Thus, the scaffolds' degradation rate should accompany

neo-tissue formation and development. This balance is crucial until the complete regeneration of tissue is accomplished.[291]

Interestingly, the scaffolds functionalised with the c-ZrO_2 nanoparticles did not show a significantly reduced degradation rate. This outcome was somewhat unexpected, considering their lower water uptake (**Figure 3.4**), suggesting they would undergo less hydrolysis.[292] The inclusion of the nanoparticles may have caused alterations in the polymeric matrix, thereby altering its inherent properties.[293] Consequently, it is plausible that despite a reduced water uptake, the amount of aqueous media absorbed had been enough to initiate the hydrolytic reaction. Thereupon, the inclusion of the nanoparticles within the scaffolds' structure did not interfere with their degradation, despite the lower water uptake, suggesting the possibility of having simultaneously more mechanically robust scaffolds with an even degradation rate.

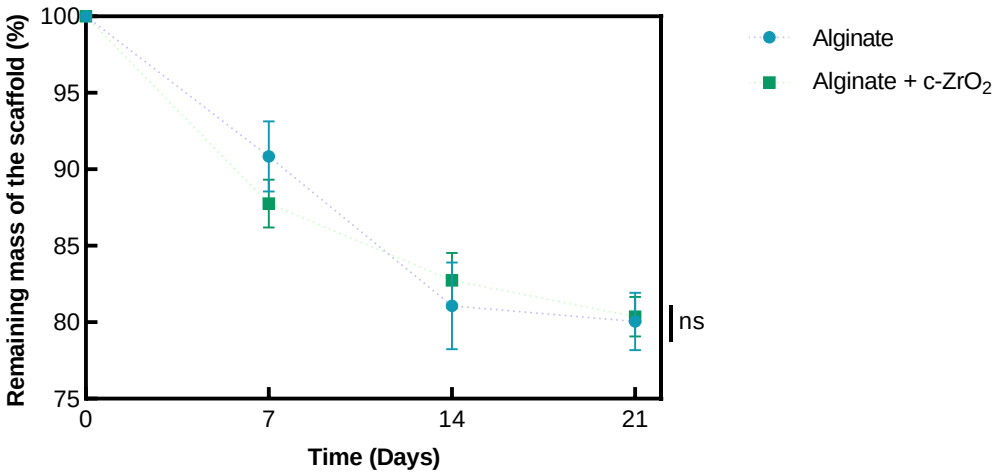

Figure 3.5:Remaining mass of the alginate scaffolds with and without c-ZrO_2 nanoparticles over 21 days. Two-way ANOVA test, (ns) not significant. All data presented as plot individual values, mean ± SD (N=5).

3.4.1.4 Mechanical analysis

Scaffolds' ability to withstand compressive forces is crucial for the proper development of scaffolds capable of supporting bone regeneration and growth. Moreover, a comprehensive understanding of scaffolds' mechanical behaviour is paramount since the cellular activity and differential fate are also regulated by mechanical cues.[294]

The results presented in **Figure 3.6(a)** illustrate the stress-strain curve of the two scaffold types, highlighting the scaffolds' elastomeric behaviour. **Figure 3.6(b)** indicates that incorporating c-ZrO_2 nanoparticles into the alginate scaffolds led to a slightly increased Young's modulus (4.68 ± 2.68 kPa) compared to the unmodified alginate scaffolds (3.42 ± 1.43 kPa). Nevertheless, statistical significance was not obtained, possibly due to the small sample size (N). Thus, the repetition of this assay with a larger sample size could eventually provide more valuable insights.

Compressive testing was executed on samples that had been pre-wetted to better simulate conditions found *in vivo* or cell culture environments. The Young's modulus, also known as elastic modulus, of the resulting hydrogels was calculated at low strain levels to avoid the densification effect on their polymeric network caused by water expulsion during compression. Young's modulus quantitatively measures the stiffness within its elastic range. It is defined as the ratio between stress exerted upon a material and the resultant strain during compression. As such, Young's modulus is an essential metric for evaluating a material's ability to withstand deformation under load.[295] Higher young modulus signifies an increased stiffness of the material and, therefore greater resistance towards deformation.[296].

The results depicted in **Figure 3.6(b)** are in accordance with the lower water uptake (**Figure 3.4**) and porosity (**Figure 3.3(b)**) obtained for the scaffolds functionalised with the nanoparticles. Despite this, given the remarkable difference in the water uptake between both scaffold types, it would have been expected that the scaffolds with nanoparticles presented significantly higher Young's modulus. The inclusion of ceramic nanoparticles into biomaterials is widely reported to enhance its stiffness.[297,298] Moreover, the elastic modulus of alginate-based hydrogels exhibits considerable variation, influenced by the crosslinking and synthesis methods employed. For instance, reported values range from 2.8 kPa to 78.8 kPa.[299,300]

Regarding osteochondral TE, the subchondral bone exhibits a Young's modulus ranging from 6 x 10^6 - 13 x 10^6 kPa[301]. Similarly, in the periodontium for the alveolar bone, an elastic modulus of 11.5 x 10^6 kPa has been mentioned.[302] Despite incorporating c-ZrO_2 nanoparticles leading to a minor enhancement of the scaffolds' elastic modulus, making it closer to *in vivo* conditions, the achieved value of 4.68 ± 2.68 kPa largely fails to replicate the elastic moduli of the hard bone tissues found in both the osteochondral unit and periodontium, Therefore, a substantial increase in the nanoparticle content could potentially elevate the elastic modulus, allowing better proximity to these native structures.

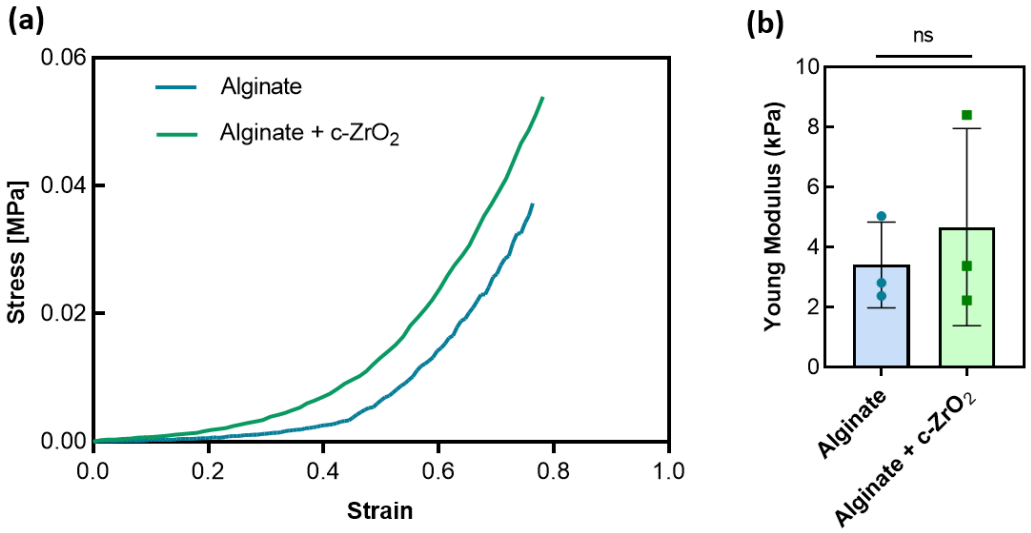

Figure 3.6: Mechanical characterisation of the alginate scaffolds with and without c-ZrO_2 nanoparticles. (a) Comparison of stress-strain profiles between both scaffold types. **(b)** Determination of the young's modulus values for both scaffold types within the initial linear region. T-test, (ns) not significant. Data presented as plot individual values, mean ± SD (N=3).

3.4.2 Biological characterisation

3.4.2.1 Cytotoxic assessment

To evaluate the cytotoxicity of the produced scaffolds, particularly to determine if the incorporation of the newly synthesised c-ZrO_2 nanoparticles had any adverse effect MTT assays were conducted. The MTT assay is a calorimetric experiment commonly utilised to assess cell cytotoxicity providing insights about cell proliferation and viability. This assay quantifies the mitochondrial activity of viable cells by monitoring the enzymatic degradation of the yellow MTT dye into insoluble purple-blue formazan crystals, facilitating quantitative analysis via spectrometry.[303,304] The MTT assay has been extensively utilised in studying *in vitro* toxicity of nanoparticles[305,306], enabling the evaluation of their effects when incorporated into scaffolds as potential medical devices, via extract testing.[307] Moreover, addressing the cytotoxicity of scaffolds prior to cell culture is an important step in evaluating the safety and effectiveness of biomaterials, providing valuable insights about their biocompatibility before proceeding with more extensive *in vitro* or *in vivo* testing.[308] NIH/3T3 fibroblast cells are frequently used as a model for in vitro cytotoxicity assessments due to their ease of cultivation and consistent response to stimuli, making them highly suitable for investigating biomaterials' cytotoxicity.[309,310]

The findings exhibited in **Figure 3.7** denote that the functionalisation of the alginate scaffolds with the newly synthesised c-ZrO_2 nanoparticles did not compromise the cell viability of the pristine alginate scaffolds and showed no significant statistical variation. Interestingly, the cell viability was found

slightly elevated for the alginate scaffolds functionalised with the nanoparticles (99.05 ± 4.68 %) when compared to the unmodified alginate scaffold (95.09 ± 13.76%). The cell viability results for the various extract dilutions (100%, 50%, 25% and 12.5%) are depicted in **Figure S2**, in the supplementary data.

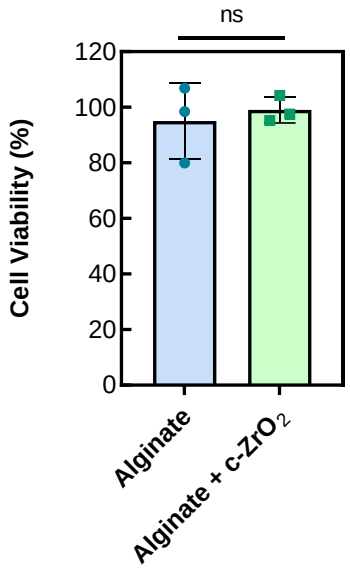

Figure 3.7: Cell viability using MTT assay on alginate scaffolds with and without c-ZrO_2 nanoparticles, after 24 hours for the 100% extract sample. T-test, (ns) not significant. Data presented as plot individual values, mean ± SD (N=3).

According to ISO 109993-5 a biomaterial has a cytotoxic potential if its cell viability is inferior to 70%.[275] From the results presented in **Figure 3.7** it is possible to infer that none of the scaffolds used in this study presented a cytotoxic potential even after the c-ZrO_2 nanoparticles inclusion, with cell viabilities close to 100%. These results are in accordance with what is expected since alginate is consensually described as a biocompatible polymer [179,311] and ZrO_2 nanoparticles are mostly described as non-toxic and biocompatible.[312,313] Similarly, *Ghanbari et al*[80] observed an enhancement in cell viability within alginate-based hydrogels that incorporated 1.5% ZrO_2 nanoparticles, achieving a viability rate of 87.5%. This was contrasted with the viability of unmodified alginate hydrogel, which was found to be 81.0%. These findings were also determined through MTT assays conducted over a 24-hour period of exposure.

Hence, the synthesised Ca-stabilised ZrO_2 nanoparticles in this study, referred to as c-ZrO_2 nanoparticles, exhibited minimal cytotoxic potential. This low toxicity of the alginate scaffolds functionalised with the c-ZrO_2 marks them as suitable and promising for posterior studying and cell culture experiments.

3.4.2.2. Proliferation experiment

The proliferation of human BM-MSCs was qualitatively evaluated using the Alamar Blue assay. This non-destructive fluorometric assay monitors the reduction of resazurin, a blue non-fluorescent component into resorufin, a pink fluorescent compound, through mitochondrial enzyme activity.[273,314] Moreover, this dye is soluble in water, non-toxic, maintains its stability within cell culture environments and is permeable across cell membranes. Therefore, the continuous monitoring of cell cultures and cellular proliferation via fluorescence detection is possible.[315] human BM-MSCs were selected due to their ability to differentiate into various mesodermal lineages when properly stimulated, and their well-documented use in TE applications.[316,317] Nevertheless, this cell type is primarily associated with osteochondral TE due to its high potential to differentiate in osteoblasts[318] (bone-forming cells) and chondrocytes (cartilage cells)[319]. Despite this, human BM-MSCs may serve as an alternative cell source to human periodontal ligament stem cells (PDLSCs), this is due to their high osteogenic potential, an essential property for alveolar bone regeneration[320]

The graph presented in **Figure 3.8(a)** illustrates the results obtained from the Alamar Blue assay, which assessed the proliferation of human BM-MSCs on days 1, 4, and 7. As mentioned before, the fluorescence intensity reflects the reduction of resazurin by metabolically active cells. Thus, increased fluorescence intensity signifies enhanced metabolic activity within the scaffold, and therefore strongly suggesting a higher cell proliferation. Based on the fluorescence intensity, it can be inferred that the scaffolds without nanoparticles exhibited a relatively uniform proliferation rate (1201.22 ± 659.96 a.u) compared to the c-ZrO_2 alginate scaffolds (940.78 ± 277.65 a.u) on day 1. Interestingly, the observed pattern did not persist on days 4 and 7 instead, the intensity measurements revealed a statistically significant increase in cell proliferation within the pristine scaffolds. Specifically, the fluoresce intensity was obtained at 4705.89 ± 806.60 a.u on day 4 and 5675.00 ± 941.55 a.u on day 7. In comparison, the scaffolds containing nanoparticles showed lower levels of cell proliferation, with values of 2001.22 ± 612.04 a.u on day 4 and 2766.33 ± 831.75 a.u on day 7. Moreover, regarding the fold increase on day 4 (**Figure 3.8(b)**) a statistically significant difference was observed. The sole alginate scaffolds exhibited the highest rise with a value of 3.92 ± 0.75, whereas the scaffolds incorporating nanoparticles showed only an increase of 2.13 ± 0.65. This tendency persisted on day 7 (**Figure 3.8(c)**) with the scaffolds showing increases of 4.72 ± 0.78 and 2.94 ± 0.88, for those without and with c-ZrO_2 nanoparticles, respectively. Nonetheless, statistical significance was not obtained.

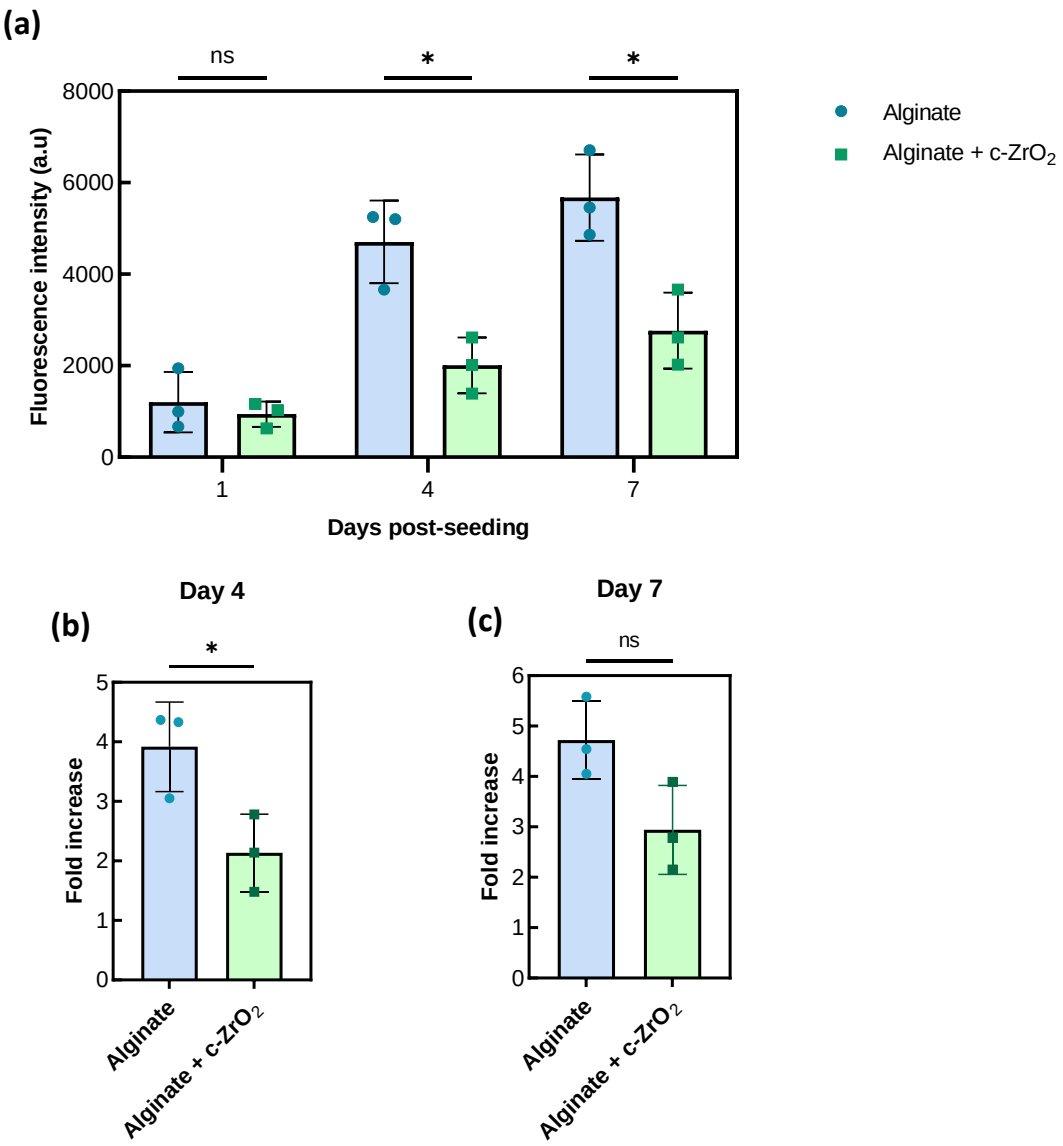

Figure 3.8: Almar Blue assay for proliferation analysis of human BM-MSCs on alginate scaffolds with and without c-ZrO_2. (a) Assessment of cellular metabolic activity within scaffolds at various time points: day 1, day 4, and day 7. Two-way ANOVA test with Šidák multiple comparison test. **(b)** Day 4-fold increase comparison between the scaffold groups relative to day 1. T-test, *p<0.05, ns (not significant). **(c)** Day 7-fold increase comparison between the scaffold groups relative to day 1. T-test, *p<0.05, ns (not significant). All data presented as plot individual values, mean ± SD (N=3).

The effect of the addition of the c-ZrO_2 within the scaffolds is evident, however, it is improbable that the synthesised c-ZrO_2 nanoparticles exerted a direct cytotoxic effect on the human BM-MSCs. This is supported by the consensus that ZrO_2 nanoparticles are biocompatible [170,254], as evidenced by the minimal cytotoxic potential shown in **Figure 3.7**. However, it is fundamental to denote that after the addition c-ZrO_2 nanoparticles, the scaffolds presented a reduction in their dimensions, and consequently a diminished cross-sectional area and volume as depicted in **Table S1** in the supplementary data. Moreover, this size reduction was more prominent for the scaffolds that were produced for this

experiment (**Figure S3** in the supplementary data). This phenomenon opens avenues for improvement. To further comprehend and refine the soaking process of the newly synthesised c-ZrO_2 nanoparticles into the alginate scaffolds, assessing their zeta potential could provide valuable insights.[321] This assessment could clarify how these nanoparticles interact with the PEG aqueous solution during their delivery and subsequently, with the scaffold itself. Understanding this interaction is pivotal to improve the integration of nanoparticles and possibly to manage the reduction in scaffolds' size effectively.

Scaffold architecture significantly affects cell growth and cell spatial distribution.[322,323] Since cell proliferation is constricted to the scaffold structure and nutrients, oxygen and waste products diffusion is limited by surface area and other factors such as porosity, pore size and scaffold macroscopic shape.[323] Nevertheless, the findings from this study indicated that there were no substantial variations observed in terms of porosity and pore size between both scaffold groups (**Figure 3.3(b) and 3.3(a)**). Therefore, macroscopic shape characteristics, specifically the diminished dimensions of the scaffolds functionalised with the nanoparticles likely influenced the results presented in **Figure 3.8**. Since scaffolds provide a void volume for cell proliferation and tissue formation, a reduced size and consequently surface area and volume may raise diffusion limitations and less available space for cell proliferation, impairing the metabolic activity of human BM-MSCs.[323–325] Taking this into account, the alginate scaffolds without nanoparticles due to their major dimensions probably displayed a more suitable microenvironment for the proliferation of metabolically active cells.

The reduced metabolic activity observed upon c-ZrO_2 nanoparticle incorporation presents a challenge. However, it is noteworthy that the differentiation of human BM-MSCs has not been conducted in the current study. Additionally, other factors, including cell morphology, could indeed play a role in determining the cell fate within the scaffold.[326]

3.4.2.3 Cell morphology analysis

SEM analysis is a widely used powerful tool for examining both cell morphology and scaffold characteristics. Furthermore, it facilitates the observation of cell adhesion and integration within the scaffold's structure.[327,328]

As evident from **Figure 3.9**, it is possible to confirm that the human BM-MSCs adhered and were integrated within the scaffold structure after a 7-day cultivation period. This finding is supported by the visibility of cell-aggregated structures at the 1 mm scale (**Figure 3.9(c) to 3.9(f)**) and their absence in the acellular alginate scaffold (**Figure 3.9(a) and 3.9(b)**). Moreover, the larger size dimension of these structures in the pristine alginate scaffold is in alignment with the aforementioned results (**Figure 3.8(c)**) which reported a higher fold increase compared to the scaffolds functionalised with the nanoparticles. Nonetheless, it is noteworthy that the inclusion of the c-ZrO_2 nanoparticles led to a change in the morphology of the cell aggregates, resulting in a more elongated appearance, as will be further discussed. Moreover, in the amplified insert in **Figure 3.9(f),** it is possible to observe the deposition of ECM which is essential to guarantee stability, support cell migration and adhesion and regulate tissue homeostasis by biomechanical and biochemical cues. [329] Specifically, the fibrous structure observed appears to be a collagen fibre, which is the most prevalent protein found in the ECM.[330] Lastly, when

examining the morphologies of the scaffolds in **Figure 3.9** compared to their initial state before cell culture (**Figure 3.2**), a noticeable shrinkage of their dimensions and pore size is observed. However, this discrepancy is attributed to the dehydration of the scaffolds following sequential ethanol baths for SEM imaging, as documented in the literature.[331]

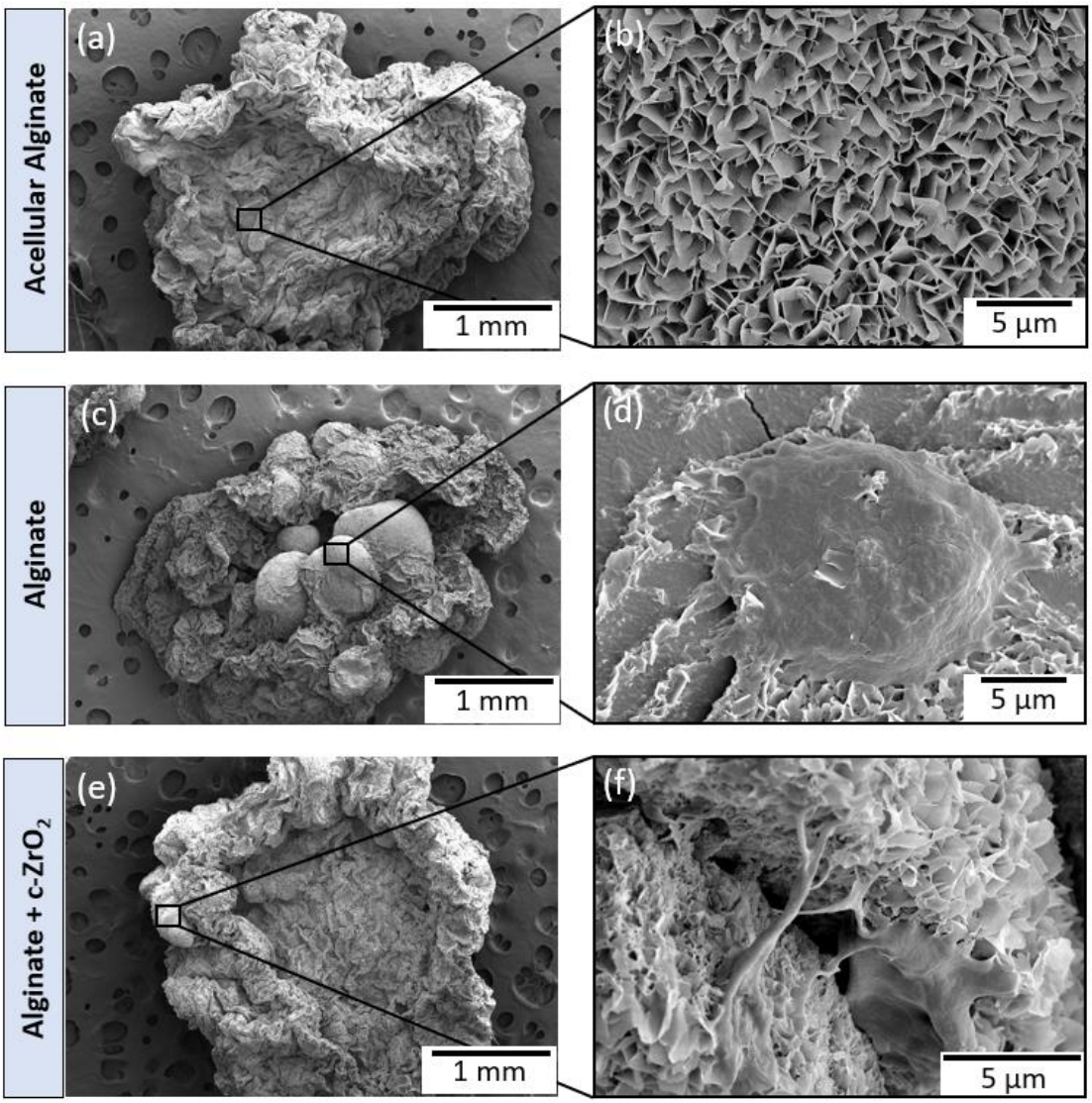

Figure 3.9: Representative SEM images of the scaffolds. (**a)** and **(b)** Alginate scaffold without cells, serving as control. **(c)** and **(d)** Pristine alginate scaffold following a 7-day cultivation period with human BM-MSCs. **(e)** and **(f)** Alginate scaffold functionalised with c-ZrO_2 nanoparticles after a 7-day cultivation period with human BM-MSCs. Scale bars represent 1 mm and 5 µm as indicated.

With the aim to further investigate with more detail the different morphology of the cell aggregates for each scaffold type and assess if that difference was significant, the alginate scaffolds with and without c-ZrO_2 nanoparticles were stained and observed using fluorescence and confocal microscopy. Therefore, different markers such as DAPI (nuclei) and Phalloidin (actin filaments) were

used. From **Figures 3.10(c), 3.10 (d), 3.10 (g) and 3.10(h)** it is evident that the addition of c-ZrO_2 nanoparticles leads to the formation of larger human BM-MSCs aggregates with notably more elongated shape, contrasting with the more rounded morphology of cell aggregates in the alginate scaffolds alone. Moreover, the shape descriptor aspect ratio (ratio between the major axis and the minor axis) permitted to quantitatively evaluate the extent of such elongation. From **Figure 3.10(i)** it can deduced that the inclusion of c-ZrO_2 significantly influenced a statistically significant cell shape shift towards a more elongated shape with an aspect ratio of 2.26 ± 0.57 compared to a value of 1.17 ± 0.14 without nanoparticles.

Cell shape plays a significant role in determining their fate during development and differentiation. Therefore, the cell nucleus and cytoplasm exhibit morphological alterations in response to signalling events, cellular functions, and differentiation processes.[332] Cell shape plays a pivotal role in tissue morphogenesis throughout development. Moreover, cell shape regulation depends on intracellular mechanics and the interaction between cells and the microenvironment.[333] Scaffold microenvironment is known to influence cell shape and therefore impact gene expression, cell metabolism and differentiation.[334,335] The inclusion of Ca-stabilised c-ZrO_2 nanoparticles resulted in a slightly enhanced stiffness, as documented in **Figure 3.6(b).** Moreover, the impact of matrix stiffness on the differentiation of human BM-MSC is well-documented throughout the scientific literature.[183,336] Furthermore, the stabilisation of the newly synthesised c-ZrO_2 nanoparticles with Ca resulted in an enhancement of their surface area due to the presence of surface defects, when compared to the pristine ZrO_2 nanoparticles, as shown by the BET analysis in **Table 2.1** (in chapter 2). Beyond merely expanding the surface area of scaffolds, incorporating nanostructures within them establishes a modified enlarged surface with specific anchoring sites, influencing cell adhesion, behaviour and morphology,[337,338] Consequently, this elucidates the observation of human BM-MSCs aggregates exhibiting an enlarged size and altered shape within the alginate scaffolds functionalised with c-ZrO_2 nanoparticles. Furthermore, the EDS analysis in **Figure 2.8** (Chapter 2) suggests that Ca tends to surround the nanoparticles enabling the speculation about their segregation to the c-ZrO_2 nanoparticles surface. This particular arrangement may facilitate MSCs accessibility to Ca ions. This could possibly influence their differentiation through the upregulation of osteogenic gene expression[266], and subsequent biomineralisation.[85,267] Therefore, offering appealing features for bone tissue regeneration, and consequently for osteochondral and periodontal TE.

Moreover, based on **Figure 3.10** it is possible to denote that the elongation of human BM-MSCs correlates with a stretching of the actin filaments (F-actin) resulting from the incorporation of nanoparticles. Given the intricate interplay between cells and ECM nanostructures, nanotopographical features may promote cell adhesion and the formation of focal adhesions (FA), which connect the actin cytoskeleton to the ECM.[337,339,340] FAs are integrin-containing multiprotein structures that enable cells to communicate microenvironment cues, to the cell nucleus through biochemical signalling [341,342] Therefore, scaffolds mechanical cues from substrate topography and stiffness are communicated through a mechanotransduction process changing gene and protein expression.[343] Complex pathways interplay through integrin-mediated signalling involving the RhoA/Rho-associated kinase(ROCK) and

others, that regulate FAs influence in the osteogenic potential of human BM-MSCs. [344] Upon proper stimulation, integrin-mediated signal transduction pathways initiate actin filament polymerisation, creating adequate cytoskeletal tension. This tension is transmitted to the nucleus, enhancing *lamin-A* expression, which in turn promotes *RUNX2* expression. Consequently, *RUNX2* drives osteogenic differentiation and the production of several markers, such as alkaline phosphatase (ALP), essential for mineralisation.[345,346] *Yang et al* [347] described that the elongation in the actin cytoskeleton, influenced by the RhoA/ROCK pathway, is linked to an enhanced osteogenic potential of human BM-MSCs. This improvement is associated with the presence of nanoscale cues that promote the formation of FAs. Also, a cell aspect ratio of 2 was identified as optimal for osteogenic potential, which correlates with the observed value for cell aggregates within this research, for the alginate scaffolds functionalised with the c-ZrO_2 nanoparticles (**Figure 3.10(i)**).[347] Moreover, more research has shown that BM-MSC[348] and human BM-MSCs[349] display an increased osteogenic potential when they exhibit a more elongated cell shape.

In the field of osteochondral TE, human BM-MSCs are widely employed because of their capacity to differentiate into osteoblasts and chondrocytes. This dual differentiation capability facilitates the regeneration of both the underlying subchondral bone tissue and cartilage.[318,319] The incorporation of the c-ZrO_2 within the alginate scaffolds resulted in a more elongated morphology of the human BM-MSCs potentially indicating an enhanced osteogenic rather than chondrogenic potential [349–351] With that being said, the incorporation of such nanoparticles shows promising features in the development of osteoinductive scaffolds to direct subchondral bone regeneration

Furthermore, human BM-MSCs can undergo differentiation into various cell types and therefore be used in periodontal regenerative therapy, despite not being the most commonly used cell type.[352,353]. Due to inherent osteogenic potential, they can be applied for the regeneration of alveolar bone, possibly improving the structural integrity and functionality of compromised periodontal tissues.[149] The results from this current study highlighted the elongation of the cell aggregates upon the inclusion of c-ZrO_2 nanoparticles within the alginate scaffolds, suggesting a potential beneficial effect on osteogenic cell potential. Elongated cell morphologies play a crucial role in the osteogenic differentiation process, a phenomenon not limited to human BM-MSCs but widely observed across MSCs.[345,354] Moreover, *Liu et al*[355] observed a stretched cell morphology and enhanced osteogenic potential for human PDLSCs cultivated in stiffer substrates possibly due to cell mechanical sensing. Thus, the alginate scaffold functionalised with the c-ZrO_2 nanoparticles may offer nanotopographical features and a suitable microenvironment for enhanced osteoblastic differentiation regarding alveolar bone regeneration for periodontal TE.

Even though this preliminary study did not conduct the differentiation of the human BM-MSCs nor analyse differential markers, the overall findings suggest that incorporating c-ZrO_2 nanoparticles into the scaffolds' environment favoured the development of larger and more elongated cell aggregates. This outcome is attributed to alterations in the scaffolds' microenvironment and topography, potentially creating a more osteoinductive setting that could stimulate MSC osteogenic differentiation. These

results open avenues for developing advanced strategies in periodontal and osteochondral tissue engineering, particularly for their bone component regeneration.

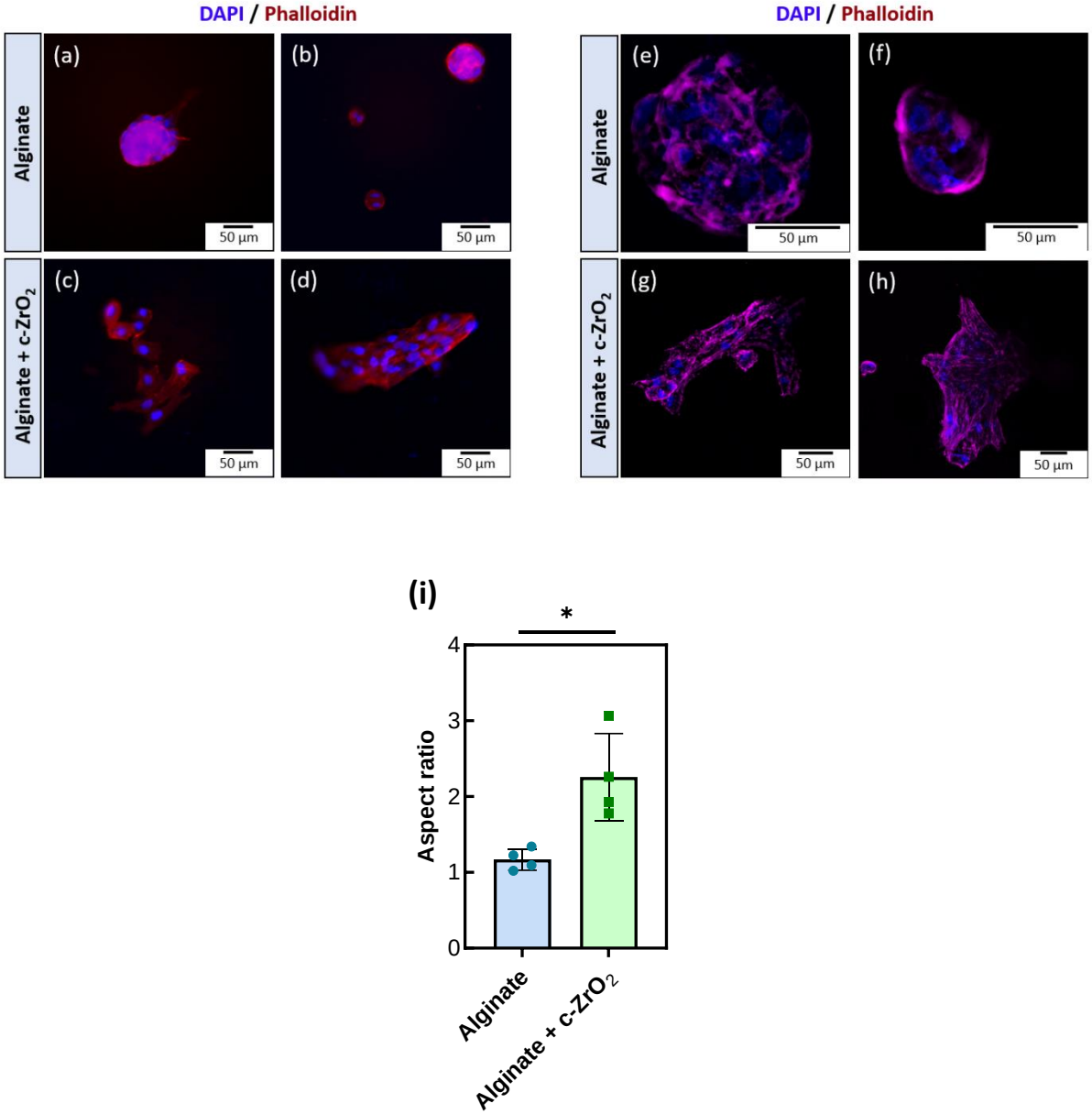

Figure 3.10: Morphological characterisation of human BM-MSCs on the alginate scaffolds with and without c-ZrO_2 nanoparticles. (a) to **(d)** Fluorescence microscopy images of 7-day cultivated alginate scaffolds without nanoparticles and with nanoparticles. **(e)** to **(h)** Confocal microscopy images of 7-day cultivated alginate scaffolds without nanoparticles and with nanoparticles. Representative images of DAPI (blue) and Phalloidin staining, all scale bars represent 50 µm. **(i)** Determination of the cell aggerates aspect ratio parameter for both scaffold types. T-test, *p<0.05. Data presented as plot individual values, mean ± SD (N=4)

3.5 Conclusion

This work aimed to establish preliminary insights about how the reinforcement of shape-memory alginate scaffolds with the newly synthesised c-ZrO_2 nanoparticles may enhance their osteoinductive potential for bone regeneration regarding osteochondral and periodontal tissues.

Two different scaffold types were produced: pristine alginate scaffolds and alginate scaffolds functionalised with c-ZrO_2 nanoparticles. After SEM imaging it was possible to observe that both scaffold types presented a highly porous surface with a mean pore size approximately equal. Moreover, no significant difference was obtained in terms of porosity for both scaffolds, however, the addition of c-ZrO_2 nanoparticles resulted in a slight decrease in porosity. Furthermore, the obtained results were in accordance with literature values described for scaffolds aiming to regenerate subchondral and alveolar bone tissues

Regarding the water uptake, it was possible to conclude that the incorporation of the c-ZrO_2 nanoparticles strongly reduced it without altering the degradation rate. This paradoxical phenomenon may be due to the possible interaction between the nanoparticles and the polymeric matrix. Moreover, despite the reduced water uptake due to nanoparticle incorporation, the amount of aqueous media absorbed might have been enough to start the hydrolytic degradation at an equal rate.

Surprisingly, only a moderate increase in stiffness was observed for the alginate scaffolds functionalised with the c-ZrO_2 nanoparticles when compared to the sole alginate scaffolds. Given the eminent diminished water uptake ratio and even the slightly decreased porosity for the scaffolds reinforced with nanoparticles, it would have been expected a more prominent enhancement in Young's modulus value. The obtained value insufficiently resembles the needed stiffness to mimic osteochondral and periodontal bone structures. An augmentation in the nanoparticle content could potentially elevate the elastic modulus, allowing better proximity to these native tissues.

Additionally, *in vitro* preliminary cytotoxicity results revealed that the inclusion of the synthesised nanoparticles did not compromise the cell viability of the unmodified alginate scaffolds. Conversely, a moderate increase was observed therefore confirming the biocompatibility of the used biomaterials. Moreover, human BM-MSCs proliferation results revealed a significantly higher fold increase on day 4, also day-7-fold increase data exhibited a higher value for the unmodified alginate scaffolds when compared to the nanoparticles ones. These results suggest that the incorporation of the c-ZrO_2 nanoparticles within the alginate scaffolds impaired cell proliferation. The observed size reduction of the functionalised scaffolds, rather than the incorporation of nanoparticles, may have negatively affected their proliferation rate, given that the nanoparticles' biocompatibility had been previously established. Therefore, there is space for improvement regarding the soaking method employed in the scaffolds' functionalisation with the synthesised nanoparticles.

Lastly, SEM imaging denoted the presence of more elongated cell aggregates for the alginate scaffolds functionalised with the c-ZrO_2 nanoparticles. The morphology of the human BM-MSCs was further assessed by confocal and fluorescence microscopy. The results confirmed a more elongated

shape for the modified alginate scaffolds, which was translated into a significantly higher aspect ratio, likely fostering an osteoinductive environment for bone regeneration. This shape modification induced by the incorporation of the c-ZrO_2 nanoparticles, possibly due to topographical mechanical sensing, is associated with an enhanced osteogenic potential of various MSCs types. Therefore, scaffold functionalisation with c-ZrO_2 nanoparticles may offer suitable nanotopographical features for osteochondral and periodontal TE, regarding subchondral and alveolar bone regeneration.

In conclusion, the incorporation of the newly synthesised c-ZrO_2 nanoparticles into the alginate scaffolds offers promising features for developing osteoinductive scaffolds. Nevertheless, further improvements must be made to obtain more a suitable applicability in the aforementioned TE applications

Chapter 4: Overall Conclusions and Future Work

4.1 Conclusions and Future work

The global aim of this thesis was to develop a new generation of ZrO_2 nanoparticles to enhance the osteoinductive properties of scaffolds for bone regeneration regarding osteochondral and periodontal tissues.

Chapter 2 described the effect of different amounts of Ca (3, 7 and 10 mol.%) on phase transformation and subsequent stabilisation of the c-ZrO_2 phase using a hydrothermal synthesis assisted by microwave irradiation without any calcination treatment. Therefore, STEM and Raman spectroscopy analysis revealed the presence of distinctive ZrO_2 crystalline phases and the subsequent stabilisation of the cubic crystalline phase for the 10 mol.%Ca-ZrO_2 nanopowder. Among the produced samples, these nanoparticles exhibited the smallest size, with an average size of 6.24 ± 0.96 nm and the presence of surface defects. These results were in alignment with the enhanced surface area obtained in the BET analysis for the c-ZrO_2 nanopowder. Additionally, EDS analysis suggests a potential Ca surface segregation, for these nanoparticles. To the author's best knowledge this study reported for the first time the stabilisation of c-ZrO_2 nanoparticles using Ca as a stabiliser in a one-step microwave approach without any pre-or post-treatment. This novel approach is both a sustainable and a cost-effective process, taking advantage of Ca biocompatibility, availability and bioactivity for TE purposes. The systematic structural characterisation of the synthesised nanoparticles resulted in a scientific manuscript and contributed to the understanding of the role of microwave irradiation in the ZrO_2 system.

Chapter 3 assessed how the reinforcement of the shape memory alginate scaffolds with the newly synthesised c-ZrO_2 nanoparticles through a soaking method impacted their osteoinductive potential for the aforementioned TE purposes. When compared to the pristine scaffolds, the alginate scaffolds functionalised with the c-ZrO_2 nanoparticles demonstrated no significant difference in terms of pore size and porosity. Moreover, the incorporation of the nanoparticles resulted in a significant decrease in the scaffolds' water uptake. Nevertheless, no substantial alteration in their degradation rate was observed. Surprisingly, only a moderate increase in Young's modulus was observed for the modified scaffolds. The obtained value revealed insufficient to fully mimic to mimic osteochondral and periodontal bone structures. Furthermore, preliminary cytotoxicity results highlighted that the incorporation of c-ZrO_2 nanoparticles did not impair cell viability. However, a decreased proliferation of the human BM-MSCs was observed (day 4 and 7) for the modified scaffolds, possibly due to the size reduction of the scaffolds upon c-ZrO_2 nanoparticles addition. Notably, after a 7-day cell culture period, the scaffolds reinforced with c-ZrO_2 nanoparticles revealed the presence of elongated cell aggregates. These aggregates demonstrated a significantly higher aspect ratio compared to those on unmodified scaffolds. This result is particularly promising since this shape modification is associated with an enhanced osteogenic of several MSCs. Thus, the incorporation of c-ZrO_2 nanoparticles may offer suitable nanotopographical characteristics such as an enhanced surface area and specific anchoring sites possibly influencing cell behaviour and morphology providing an appropriate osteoinductive environment.

Despite the limited literature on c-ZrO_2 nanoparticles for TE applications, this thesis has provided novel insights into their potential. For future research, it would be valuable to extend this one-

step green microwave approach to stabilise t-ZrO_2 also using Ca as a stabiliser. Therefore, investigating other ranges of Ca concentrations as well as different precursors would be of interest. Moreover, there is still room for improvement regarding the functionalisation of the alginate scaffolds with the synthesised nanoparticles to effectively manage their size reduction. Future work should include measuring the zeta potential of the nanoparticles to evaluate their interaction with the polymeric aqueous solution used for the soaking method. Additionally, increasing the amount of nanoparticles delivered could potentially enhance the scaffolds' mechanical performance. Future studies should consider using a larger sample size (N) and increased scaffold height to strengthen the validity of the findings. Lastly, assessing the osteogenic differentiation potential of MSCs would be crucial to validate the impact of the elongated cell aggregates on modified scaffolds and their suitability for the intended TE applications. This evaluation is currently being conducted in a collaboration.

In ongoing collaborative efforts with the Stem Cell Engineering Research Group at iBB, scaffold groups identical to those extensively studied in this thesis are undergoing further evaluation for periodontal TE applications, specifically for alveolar bone regeneration. The osteogenic potential of PDLSCs in both scaffold types was evaluated through ALP quantification analysis and by the quantification of osteogenic-related markers such as *OPN, COL I, OCN* and *RUNX2* by real-time polymerase chain reaction. Preliminary results indicated that the biological cues provided by the c-ZrO_2 nanoparticles led to enhanced early ALP activity and increased expression of the previously mentioned osteogenic-related genes. These findings further support the positive impact of c-ZrO_2 nanoparticle addition in the development of osteoinductive scaffolds capable of supporting alveolar bone tissue regeneration. This research may also result in a scientific manuscript, contributing to the development of periodontal regeneration strategies. The continuation of this thesis study highlights its promising nature, despite the current limitations.

References

(1) Chapekar, M. S. Tissue Engineering: Challenges and Opportunities. *J. Biomed. Mater. Res.* **2000**, *53* (6), 617–620. https://doi.org/10.1002/1097-4636(2000)53:6<617::AID-JBM1>3.0.CO;2-C.

(2) Mao, A. S.; Mooney, D. J. Regenerative Medicine: Current Therapies and Future Directions. *Proc. Natl. Acad. Sci. U. S. A.* **2015**, *112* (47), 14452–14459. https://doi.org/10.1073/pnas.1508520112.

(3) Facchin, F.; Bianconi, E.; Canaider, S.; Basoli, V.; Biava, P. M.; Ventura, C. Tissue Regeneration without Stem Cell Transplantation: Self-Healing Potential from Ancestral Chemistry and Physical Energies. *Stem Cells Int.* **2018**, *2018* (1), 7412035. https://doi.org/10.1155/2018/7412035.

(4) Mhanna, R.; Hasan, A. Introduction to Tissue Engineering. In *Tissue Engineering for Artificial Organs*; John Wiley & Sons, Ltd, 2017; pp 1–34. https://doi.org/10.1002/9783527689934.ch1.

(5) O'Brien, F. J. Biomaterials & Scaffolds for Tissue Engineering. *Mater. Today* **2011**, *14* (3), 88–95. https://doi.org/10.1016/S1369-7021(11)70058-X.

(6) Ostadfar, A. Chapter 9 - Tissue Engineering of Cardiovascular System. In *Biofluid Mechanics*; Ostadfar, A., Ed.; Academic Press, 2016; pp 323–339. https://doi.org/10.1016/B978-0-12-802408-9.00009-0.

(7) Caddeo, S.; Boffito, M.; Sartori, S. Tissue Engineering Approaches in the Design of Healthy and Pathological In Vitro Tissue Models. *Front. Bioeng. Biotechnol.* **2017**, *5*. https://doi.org/10.3389/fbioe.2017.00040.

(8) Polak, J. M.; Bishop, A. E. Stem Cells and Tissue Engineering: Past, Present, and Future. *Ann. N. Y. Acad. Sci.* **2006**, *1068* (1), 352–366. https://doi.org/10.1196/annals.1346.001.

(9) Kwon, S. G.; Kwon, Y. W.; Lee, T. W.; Park, G. T.; Kim, J. H. Recent Advances in Stem Cell Therapeutics and Tissue Engineering Strategies. *Biomater. Res.* **2018**, *22* (1), 36. https://doi.org/10.1186/s40824-018-0148-4.

(10) Yamzon, J. L.; Kokorowski, P.; Koh, C. J. Stem Cells and Tissue Engineering Applications of the Genitourinary Tract. *Pediatr. Res.* **2008**, *63* (5), 472–477. https://doi.org/10.1203/PDR.0b013e31816a704a.

(11) Park, S. J.; Kim, Y. Y.; Han, J. Y.; Kim, S. W.; Kim, H.; Ku, S.-Y. Advancements in Human Embryonic Stem Cell Research: Clinical Applications and Ethical Issues. *Tissue Eng. Regen. Med.* **2024**, *21* (3), 379–394. https://doi.org/10.1007/s13770-024-00627-3.

(12) Naderi, H.; Matin, M. M.; Bahrami, A. R. Review Paper: Critical Issues in Tissue Engineering: Biomaterials, Cell Sources, Angiogenesis, and Drug Delivery Systems. *J. Biomater. Appl.* **2011**, *26* (4), 383–417. https://doi.org/10.1177/0885328211408946.

(13) *Cell Sources for Tissue Engineering | SpringerLink*. https://link.springer.com/chapter/10.1007/978-3-031-35832-6_3 (accessed 2024-08-11).

(14) Zhao, S.; Chen, J.; Wu, L.; Tao, X.; Yaqub, N.; Chang, J. Induced Pluripotent Stem Cells for Tissue-Engineered Skeletal Muscles. *Int. J. Mol. Sci.* **2023**, *24* (14), 11520. https://doi.org/10.3390/ijms241411520.

(15) Ma, P. X. Scaffolds for Tissue Fabrication. *Mater. Today* **2004**, *7* (5), 30–40. https://doi.org/10.1016/S1369-7021(04)00233-0.

(16) Nandgaonkar, A. G.; Krause, W. E.; Lucia, L. A. 9 - Fabrication of Cellulosic Composite Scaffolds for Cartilage Tissue Engineering. In *Nanocomposites for Musculoskeletal Tissue Regeneration*; Liu, H., Ed.; Woodhead Publishing: Oxford, 2016; pp 187–212. https://doi.org/10.1016/B978-1-78242-452-9.00009-1.

(17) Feng, W.; Wang, Z. Tailoring the Swelling-Shrinkable Behavior of Hydrogels for Biomedical Applications. *Adv. Sci.* **2023**, *10* (28), 2303326. https://doi.org/10.1002/advs.202303326.

(18) Krishani, M.; Shin, W. Y.; Suhaimi, H.; Sambudi, N. S. Development of Scaffolds from Bio-Based Natural Materials for Tissue Regeneration Applications: A Review. *Gels* **2023**, *9* (2), 100. https://doi.org/10.3390/gels9020100.

(19) Murphy, C. M.; Matsiko, A.; Haugh, M. G.; Gleeson, J. P.; O'Brien, F. J. Mesenchymal Stem Cell Fate Is Regulated by the Composition and Mechanical Properties of Collagen-Glycosaminoglycan Scaffolds. *J. Mech. Behav. Biomed. Mater.* **2012**, *11*, 53–62. https://doi.org/10.1016/j.jmbbm.2011.11.009.

(20) Nikolova, M. P.; Chavali, M. S. Recent Advances in Biomaterials for 3D Scaffolds: A Review. *Bioact. Mater.* **2019**, *4*, 271–292. https://doi.org/10.1016/j.bioactmat.2019.10.005.

(21) Socci, M. C.; Rodríguez, G.; Oliva, E.; Fushimi, S.; Takabatake, K.; Nagatsuka, H.; Felice, C. J.; Rodríguez, A. P. Polymeric Materials, Advances and Applications in Tissue Engineering: A Review. *Bioengineering* **2023**, *10* (2), 218. https://doi.org/10.3390/bioengineering10020218.

(22) Puertas-Bartolomé, M.; Mora-Boza, A.; García-Fernández, L. Emerging Biofabrication Techniques: A Review on Natural Polymers for Biomedical Applications. *Polymers* **2021**, *13* (8), 1209. https://doi.org/10.3390/polym13081209.

(23) Phutane, P.; Telange, D.; Agrawal, S.; Gunde, M.; Kotkar, K.; Pethe, A. Biofunctionalization and Applications of Polymeric Nanofibers in Tissue Engineering and Regenerative Medicine. *Polymers* **2023**, *15* (5), 1202. https://doi.org/10.3390/polym15051202.

(24) Suamte, L.; Tirkey, A.; Barman, J.; Jayasekhar Babu, P. Various Manufacturing Methods and Ideal Properties of Scaffolds for Tissue Engineering Applications. *Smart Mater. Manuf.* **2023**, *1*, 100011. https://doi.org/10.1016/j.smmf.2022.100011.

(25) Joseph, B.; Jose, C.; Kavil, S. V.; Kalarikkal, N.; Thomas, S. Solvent-Casting Approach for Design of Polymer Scaffolds and Their Multifunctional Applications. In *Functional Biomaterials*; John Wiley & Sons, Ltd, 2023; pp 371–394. https://doi.org/10.1002/9783527827657.ch12.

(26) Dehghani, F.; Annabi, N. Engineering Porous Scaffolds Using Gas-Based Techniques. *Curr. Opin. Biotechnol.* **2011**, *22* (5), 661–666. https://doi.org/10.1016/j.copbio.2011.04.005.

(27) Pavia, F. C.; La Carrubba, V.; Piccarolo, S.; Brucato, V. Polymeric Scaffolds Prepared via Thermally Induced Phase Separation: Tuning of Structure and Morphology. *J. Biomed. Mater. Res. A* **2008**, *86* (2), 459–466. https://doi.org/10.1002/jbm.a.31621.

(28) Flores-Rojas, G. G.; Gómez-Lazaro, B.; López-Saucedo, F.; Vera-Graziano, R.; Bucio, E.; Mendizábal, E. Electrospun Scaffolds for Tissue Engineering: A Review. *Macromol* **2023**, *3* (3), 524–553. https://doi.org/10.3390/macromol3030031.

(29) Reddy, V. S.; Ramasubramanian, B.; Telrandhe, V. M.; Ramakrishna, S. Contemporary Standpoint and Future of 3D Bioprinting in Tissue/Organs Printing. *Curr. Opin. Biomed. Eng.* **2023**, *27*, 100461. https://doi.org/10.1016/j.cobme.2023.100461.

(30) Dang, M.; Saunders, L.; Niu, X.; Fan, Y.; Ma, P. X. Biomimetic Delivery of Signals for Bone Tissue Engineering. *Bone Res.* **2018**, *6* (1), 1–12. https://doi.org/10.1038/s41413-018-0025-8.

(31) De Laporte, L.; Shea, L. D. Matrices and Scaffolds for DNA Delivery in Tissue Engineering. *Adv. Drug Deliv. Rev.* **2007**, *59* (4–5), 292–307. https://doi.org/10.1016/j.addr.2007.03.017.

(32) Mohindra, P.; Desai, T. A. Micro- and Nanoscale Biophysical Cues for Cardiovascular Disease Therapy. *Nanomedicine Nanotechnol. Biol. Med.* **2021**, *34*, 102365. https://doi.org/10.1016/j.nano.2021.102365.

(33) Li, J.; Liu, Y.; Zhang, Y.; Yao, B.; Enhejirigala; Li, Z.; Song, W.; Wang, Y.; Duan, X.; Yuan, X.; Fu, X.; Huang, S. Biophysical and Biochemical Cues of Biomaterials Guide Mesenchymal Stem Cell Behaviors. *Front. Cell Dev. Biol.* **2021**, *9*, 640388. https://doi.org/10.3389/fcell.2021.640388.

(34) Hasan, A.; Morshed, M.; Memic, A.; Hassan, S.; Webster, T. J.; Marei, H. E.-S. Nanoparticles in Tissue Engineering: Applications, Challenges and Prospects. *Int. J. Nanomedicine* **2018**, *13*, 5637–5655. https://doi.org/10.2147/IJN.S153758.

(35) Ashammakhi, N.; GhavamiNejad, A.; Tutar, R.; Fricker, A.; Roy, I.; Chatzistavrou, X.; Hoque Apu, E.; Nguyen, K.-L.; Ahsan, T.; Pountos, I.; Caterson, E. J. Highlights on Advancing Frontiers in Tissue Engineering. *Tissue Eng. Part B Rev.* **2022**, *28* (3), 633–664. https://doi.org/10.1089/ten.teb.2021.0012.

(36) Sharma, R.; Kumar, S.; Bhawna; Gupta, A.; Dheer, N.; Jain, P.; Singh, P.; Kumar, V. An Insight of Nanomaterials in Tissue Engineering from Fabrication to Applications. *Tissue Eng. Regen. Med.* **2022**, *19* (5), 927–960. https://doi.org/10.1007/s13770-022-00459-z.

(37) Liu, S.; Lin, R.; Pu, C.; Huang, J.; Zhang, J.; Hou, H.; Liu, S.; Lin, R.; Pu, C.; Huang, J.; Zhang, J.; Hou, H. Nanocomposite Biomaterials for Tissue Engineering and Regenerative Medicine Applications. In *Nanocomposite Materials for Biomedical and Energy Storage Applications*; IntechOpen, 2022. https://doi.org/10.5772/intechopen.102417.

(38) Sagadevan, S.; Schirhagl, R.; Rahman, M. Z.; Bin Ismail, M. F.; Lett, J. A.; Fatimah, I.; Mohd Kaus, N. H.; Oh, W.-C. Recent Advancements in Polymer Matrix Nanocomposites for Bone Tissue Engineering Applications. *J. Drug Deliv. Sci. Technol.* **2023**, *82*, 104313. https://doi.org/10.1016/j.jddst.2023.104313.

(39) Carotenuto, F.; Politi, S.; Ul Haq, A.; De Matteis, F.; Tamburri, E.; Terranova, M. L.; Teodori, L.; Pasquo, A.; Di Nardo, P. From Soft to Hard Biomimetic Materials: Tuning Micro/Nano-Architecture of Scaffolds for Tissue Regeneration. *Micromachines* **2022**, *13* (5), 780. https://doi.org/10.3390/mi13050780.

(40) Kreyling, W. G.; Semmler-Behnke, M.; Chaudhry, Q. A Complementary Definition of Nanomaterial. *Nano Today* **2010**, *5* (3), 165–168. https://doi.org/10.1016/j.nantod.2010.03.004.

(41) Paras, null; Yadav, K.; Kumar, P.; Teja, D. R.; Chakraborty, S.; Chakraborty, M.; Mohapatra, S. S.; Sahoo, A.; Chou, M. M. C.; Liang, C.-T.; Hang, D.-R. A Review on Low-Dimensional Nanomaterials:

Nanofabrication, Characterization and Applications. *Nanomater. Basel Switz.* **2022**, *13* (1), 160. https://doi.org/10.3390/nano13010160.

(42) Mekuye, B.; Abera, B. Nanomaterials: An Overview of Synthesis, Classification, Characterization, and Applications. *Nano Sel.* **2023**, *4* (8), 486–501. https://doi.org/10.1002/nano.202300038.

(43) Joudeh, N.; Linke, D. Nanoparticle Classification, Physicochemical Properties, Characterization, and Applications: A Comprehensive Review for Biologists. *J. Nanobiotechnology* **2022**, *20* (1), 262. https://doi.org/10.1186/s12951-022-01477-8.

(44) Han, S.; Cruz, S. H.; Park, S.; Shin, S. R. Nano-Biomaterials and Advanced Fabrication Techniques for Engineering Skeletal Muscle Tissue Constructs in Regenerative Medicine. *Nano Converg.* **2023**, *10* (1), 48. https://doi.org/10.1186/s40580-023-00398-y.

(45) Bapat, R. A.; Chaubal, T. V.; Dharmadhikari, S.; Abdulla, A. M.; Bapat, P.; Alexander, A.; Dubey, S. K.; Kesharwani, P. Recent Advances of Gold Nanoparticles as Biomaterial in Dentistry. *Int. J. Pharm.* **2020**, *586*, 119596. https://doi.org/10.1016/j.ijpharm.2020.119596.

(46) Fathi-Achachelouei, M.; Knopf-Marques, H.; Ribeiro da Silva, C. E.; Barthès, J.; Bat, E.; Tezcaner, A.; Vrana, N. E. Use of Nanoparticles in Tissue Engineering and Regenerative Medicine. *Front. Bioeng. Biotechnol.* **2019**, *7*.

(47) Gulati, S.; Kumar, S.; Sharma, N.; Goyal, K.; Agarwal, T. Chapter 7 - Bioresorbable Nanoceramics: Novel and Efficient Drug Delivery Vehicles. In *Industrial Applications of Nanoceramics*; Mallakpour, S., Hussain, C. M., Eds.; Micro and Nano Technologies; Elsevier, 2024; pp 99–125. https://doi.org/10.1016/B978-0-323-88654-3.00008-1.

(48) Anjaneyulu, U.; Zhang, V.; Ren, P.-G. Bioinert Ceramics for Biomedical Applications; 2019.

(49) Monavari, M.; Homaeigohar, S.; Fuentes-Chandía, M.; Nawaz, Q.; Monavari, M.; Venkatraman, A.; Boccaccini, A. R. 3D Printing of Alginate Dialdehyde-Gelatin (ADA-GEL) Hydrogels Incorporating Phytotherapeutic Icariin Loaded Mesoporous SiO2-CaO Nanoparticles for Bone Tissue Engineering. *Mater. Sci. Eng. C Mater. Biol. Appl.* **2021**, *131*, 112470. https://doi.org/10.1016/j.msec.2021.112470.

(50) Łukowicz, K.; Zagrajczuk, B.; Nowak, A.; Niedźwiedzki, Ł.; Laczka, M.; Cholewa-Kowalska, K.; Osyczka, A. M. The Role of CaO/SiO2 Ratio and P2O5 Content in Gel-Derived Bioactive Glass-Polymer Composites in the Modulation of Their Bioactivity and Osteoinductivity in Human BMSCs. *Mater. Sci. Eng. C* **2020**, *109*, 110535. https://doi.org/10.1016/j.msec.2019.110535.

(51) Mo, X.; Zhang, D.; Liu, K.; Zhao, X.; Li, X.; Wang, W. Nano-Hydroxyapatite Composite Scaffolds Loaded with Bioactive Factors and Drugs for Bone Tissue Engineering. *Int. J. Mol. Sci.* **2023**, *24* (2), 1291. https://doi.org/10.3390/ijms24021291.

(52) Lee, J.-H.; Seo, S.-J.; Kim, H.-W. Bioactive Glass-Based Nanocomposites for Personalized Dental Tissue Regeneration. *Dent. Mater. J.* **2016**, *35* (5), 710–720. https://doi.org/10.4012/dmj.2015-428.

(53) Pushpalatha, C.; Gayathri, V. S.; Sowmya, S. V.; Augustine, D.; Alamoudi, A.; Zidane, B.; Hassan Mohammad Albar, N.; Bhandi, S. Nanohydroxyapatite in Dentistry: A Comprehensive Review. *Saudi Dent. J.* **2023**, *35* (6), 741–752. https://doi.org/10.1016/j.sdentj.2023.05.018.

(54) N. Sathy, B.; Olvera, D.; Gonzalez-Fernandez, T.; M. Cunniffe, G.; Pentlavalli, S.; Chambers, P.; Jeon, O.; Alsberg, E.; O. McCarthy, H.; Dunne, N.; Donahue, T. L. H.; J. Kelly, D. RALA Complexed

α-TCP Nanoparticle Delivery to Mesenchymal Stem Cells Induces Bone Formation in Tissue Engineered Constructs in Vitro and in Vivo. *J. Mater. Chem. B* **2017**, *5* (9), 1753–1764. https://doi.org/10.1039/C6TB02881K.

(55) Li, X.; Yang, X.; Liu, X.; He, W.; Huang, Q.; Li, S.; Feng, Q. Calcium Carbonate Nanoparticles Promote Osteogenesis Compared to Adipogenesis in Human Bone-Marrow Mesenchymal Stem Cells. *Prog. Nat. Sci. Mater. Int.* **2018**, *28* (5), 598–608. https://doi.org/10.1016/j.pnsc.2018.09.004.

(56) Ogawa, K.; Miyaji, H.; Kato, A.; Kosen, Y.; Momose, T.; Yoshida, T.; Nishida, E.; Miyata, S.; Murakami, S.; Takita, H.; Fugetsu, B.; Sugaya, T.; Kawanami, M. Periodontal Tissue Engineering by Nano Beta-Tricalcium Phosphate Scaffold and Fibroblast Growth Factor-2 in One-Wall Infrabony Defects of Dogs. *J. Periodontal Res.* **2016**, *51* (6), 758–767. https://doi.org/10.1111/jre.12352.

(57) Elsayed, N. A.; Zada, S.; Allam, N. K. Mineralization of Electrospun Gelatin/CaCO3 Composites: A New Approach for Dental Applications. *Mater. Sci. Eng. C* **2019**, *100*, 655–664. https://doi.org/10.1016/j.msec.2019.03.049.

(58) Bhowmick, A.; Jana, P.; Pramanik, N.; Mitra, T.; Banerjee, S. L.; Gnanamani, A.; Das, M.; Kundu, P. P. Multifunctional Zirconium Oxide Doped Chitosan Based Hybrid Nanocomposites as Bone Tissue Engineering Materials. *Carbohydr. Polym.* **2016**, *151*, 879–888. https://doi.org/10.1016/j.carbpol.2016.06.034.

(59) Zhang, R.; Lee, P.; Lui, V. C. H.; Chen, Y.; Liu, X.; Lok, C. N.; To, M.; Yeung, K. W. K.; Wong, K. K. Y. Silver Nanoparticles Promote Osteogenesis of Mesenchymal Stem Cells and Improve Bone Fracture Healing in Osteogenesis Mechanism Mouse Model. *Nanomedicine Nanotechnol. Biol. Med.* **2015**, *11* (8), 1949–1959. https://doi.org/10.1016/j.nano.2015.07.016.

(60) Yang, D. H.; Nah, H.; Lee, D.; Min, S. J.; Park, S.; An, S.-H.; Wang, J.; He, H.; Choi, K.-S.; Ko, W.-K.; Lee, J. S.; Kwon, I. K.; Lee, S. J.; Heo, D. N. A Review on Gold Nanoparticles as an Innovative Therapeutic Cue in Bone Tissue Engineering: Prospects and Future Clinical Applications. *Mater. Today Bio* **2024**, *26*, 101016. https://doi.org/10.1016/j.mtbio.2024.101016.

(61) Abdel-Gawad, R.; Osman, R.; Awad, G. A. S.; Mortada, N. Wound Healing Potential of Silver Nanoparticles Embedded in Optimized Bio-Inspired Hybridized Chitosan Soft and Dry Hydrogel. *Carbohydr. Polym.* **2024**, *324*, 121526. https://doi.org/10.1016/j.carbpol.2023.121526.

(62) Batool, Z.; Muhammad, G.; Iqbal, M. M.; Aslam, M. S.; Raza, M. A.; Sajjad, N.; Abdullah, M.; Akhtar, N.; Syed, A.; Elgorban, A. M.; Al-Rejaie, S. S.; Shafiq, Z. Hydrogel Assisted Synthesis of Gold Nanoparticles with Enhanced Microbicidal and in Vivo Wound Healing Potential. *Sci. Rep.* **2022**, *12* (1), 6575. https://doi.org/10.1038/s41598-022-10495-3.

(63) Shevach, M.; Maoz, B. M.; Feiner, R.; Shapira, A.; Dvir, T. Nanoengineering Gold Particle Composite Fibers for Cardiac Tissue Engineering. *J. Mater. Chem. B* **2013**, *1* (39), 5210–5217. https://doi.org/10.1039/C3TB20584C.

(64) Ghandforoushan, P.; Hanaee, J.; Aghazadeh, Z.; Samiei, M.; Navali, A. M.; Khatibi, A.; Davaran, S. Enhancing the Function of PLGA-Collagen Scaffold by Incorporating TGF-B1-Loaded PLGA-PEG-PLGA Nanoparticles for Cartilage Tissue Engineering Using Human Dental Pulp Stem Cells. *Drug Deliv. Transl. Res.* **2022**, *12* (12), 2960–2978. https://doi.org/10.1007/s13346-022-01161-2.

(65) Ribeiro, M. C.; Correa, V. L. R.; Silva, F. K. L. da; Casas, A. A.; Chagas, A. de L. das; Oliveira, L. P. de; Miguel, M. P.; Diniz, D. G. A.; Amaral, A. C.; Menezes, L. B. de. Wound Healing Treatment Using Insulin within Polymeric Nanoparticles in the Diabetes Animal Model. *Eur. J. Pharm. Sci.* **2020**, *150*, 105330. https://doi.org/10.1016/j.ejps.2020.105330.

(66) Deng, C.; Dong, N.; Shi, J.; Chen, S.; Xu, L.; Shi, F.; Hu, X.; Zhang, X. Application of Decellularized Scaffold Combined with Loaded Nanoparticles for Heart Valve Tissue Engineering in Vitro. *J. Huazhong Univ. Sci. Technolog. Med. Sci.* **2011**, *31* (1), 88–93. https://doi.org/10.1007/s11596-011-0156-2.

(67) Choe, G.; Lee, M.; Oh, S.; Seok, J. M.; Kim, J.; Im, S.; Park, S. A.; Lee, J. Y. Three-Dimensional Bioprinting of Mesenchymal Stem Cells Using an Osteoinductive Bioink Containing Alginate and BMP-2-Loaded PLGA Nanoparticles for Bone Tissue Engineering. *Biomater. Adv.* **2022**, *136*, 212789. https://doi.org/10.1016/j.bioadv.2022.212789.

(68) Xue, Y.; Hong, X.; Gao, J.; Shen, R.; Ye, Z. Preparation and Biological Characterization of the Mixture of Poly(Lactic-Co-Glycolic Acid)/Chitosan/Ag Nanoparticles for Periodontal Tissue Engineering. *Int. J. Nanomedicine* **2019**, *14*, 483–498. https://doi.org/10.2147/IJN.S184396.

(69) Liu, H.; Webster, T. J. Mechanical Properties of Dispersed Ceramic Nanoparticles in Polymer Composites for Orthopedic Applications. *Int. J. Nanomedicine* **2010**, *5*, 299–313.

(70) Tjong, S. C. Structural and Mechanical Properties of Polymer Nanocomposites. *Mater. Sci. Eng. R Rep.* **2006**, *53* (3), 73–197. https://doi.org/10.1016/j.mser.2006.06.001.

(71) Jayakumar, R.; Ramachandran, R.; Sudheesh Kumar, P. T.; Divyarani, V. V.; Srinivasan, S.; Chennazhi, K. P.; Tamura, H.; Nair, S. V. Fabrication of Chitin–Chitosan/Nano ZrO2 Composite Scaffolds for Tissue Engineering Applications. *Int. J. Biol. Macromol.* **2011**, *49* (3), 274–280. https://doi.org/10.1016/j.ijbiomac.2011.04.020.

(72) Pina, S.; Rebelo, R.; Correlo, V. M.; Oliveira, J. M.; Reis, R. L. Bioceramics for Osteochondral Tissue Engineering and Regeneration. In *Osteochondral Tissue Engineering: Nanotechnology, Scaffolding-Related Developments and Translation*; Oliveira, J. M., Pina, S., Reis, R. L., San Roman, J., Eds.; Advances in Experimental Medicine and Biology; Springer International Publishing: Cham, 2018; pp 53–75. https://doi.org/10.1007/978-3-319-76711-6_3.

(73) Yamamuro, T. Bioceramics. In *Biomechanics and Biomaterials in Orthopedics*; Poitout, D. G., Ed.; Springer: London, 2004; pp 22–33. https://doi.org/10.1007/978-1-4471-3774-0_3.

(74) Manicone, P. F.; Rossi Iommetti, P.; Raffaelli, L. An Overview of Zirconia Ceramics: Basic Properties and Clinical Applications. *J. Dent.* **2007**, *35* (11), 819–826. https://doi.org/10.1016/j.jdent.2007.07.008.

(75) Gautam, C.; Joyner, J.; Gautam, A.; Rao, J.; Vajtai, R. Zirconia Based Dental Ceramics: Structure, Mechanical Properties, Biocompatibility and Applications. *Dalton Trans.* **2016**, *45* (48), 19194–19215. https://doi.org/10.1039/C6DT03484E.

(76) Chopra, D.; Guo, T.; Gulati, K.; Ivanovski, S. Load, Unload and Repeat: Understanding the Mechanical Characteristics of Zirconia in Dentistry. *Dent. Mater. Off. Publ. Acad. Dent. Mater.* **2024**, *40* (1), e1–e17. https://doi.org/10.1016/j.dental.2023.10.007.

(77) Piconi, C.; Sprio, S. Oxide Bioceramic Composites in Orthopedics and Dentistry. *J. Compos. Sci.* **2021**, *5* (8), 206. https://doi.org/10.3390/jcs5080206.

(78) Mansoor, A.; Khurshid, Z.; Khan, M. T.; Mansoor, E.; Butt, F. A.; Jamal, A.; Palma, P. J. Medical and Dental Applications of Titania Nanoparticles: An Overview. *Nanomaterials* **2022**, *12* (20), 3670. https://doi.org/10.3390/nano12203670.

(79) Alhotan, A.; Yates, J.; Zidan, S.; Haider, J.; Silikas, N. Assessing Fracture Toughness and Impact Strength of PMMA Reinforced with Nano-Particles and Fibre as Advanced Denture Base Materials. *Materials* **2021**, *14* (15), 4127. https://doi.org/10.3390/ma14154127.

(80) Ghanbari, M.; Salavati-Niasari, M.; Mohandes, F.; Firouzi, Z.; Mousavi, S.-D. The Impact of Zirconium Oxide Nanoparticles Content on Alginate Dialdehyde-Gelatin Scaffolds in Cartilage Tissue Engineering. *J. Mol. Liq.* **2021**, *335*, 116531. https://doi.org/10.1016/j.molliq.2021.116531.

(81) Hu, C.; Sun, J.; Long, C.; Wu, L.; Zhou, C.; Zhang, X. Synthesis of Nano Zirconium Oxide and Its Application in Dentistry. *Nanotechnol. Rev.* **2019**, *8* (1), 396–404. https://doi.org/10.1515/ntrev-2019-0035.

(82) Saurav, S.; Sharma, P.; Kumar, A.; Tabassum, Z.; Girdhar, M.; Mamidi, N.; Mohan, A. Harnessing Natural Polymers for Nano-Scaffolds in Bone Tissue Engineering: A Comprehensive Overview of Bone Disease Treatment. *Curr. Issues Mol. Biol.* **2024**, *46* (1), 585–611. https://doi.org/10.3390/cimb46010038.

(83) Afzal, A. Implantable Zirconia Bioceramics for Bone Repair and Replacement: A Chronological Review. *Mater. Express* **2014**, *4* (1), 1–12. https://doi.org/10.1166/mex.2014.1148.

(84) Yoon, S. J.; Yang, D. H.; Kim, E.-C.; Noh, K.; Lee, D.-W. In Vitro Osteogenic Differentiation Enhanced by Zirconia Coated with Nano-Layered Growth and Differentiation Factor-5. *J. Nanosci. Nanotechnol.* **2016**, *16* (1), 280–286. https://doi.org/10.1166/jnn.2016.10828.

(85) Tana, F.; De Giglio, E.; Cometa, S.; D'Agostino, A.; Serafini, A.; Variola, F.; Bono, N.; Chiesa, R.; De Nardo, L. Ca-Doped Zirconia Mesoporous Coatings for Biomedical Applications: A Physicochemical and Biological Investigation. *J. Eur. Ceram. Soc.* **2020**, *40* (11), 3698–3706. https://doi.org/10.1016/j.jeurceramsoc.2019.10.024.

(86) Zhu, S.; Chen, W.; Masson, A.; Li, Y.-P. Cell Signaling and Transcriptional Regulation of Osteoblast Lineage Commitment, Differentiation, Bone Formation, and Homeostasis. *Cell Discov.* **2024**, *10* (1), 1–39. https://doi.org/10.1038/s41421-024-00689-6.

(87) Rao, J. C.; Zhou, Y.; Li, D. X. L12- and L10-like Cation-Ordered Structures in ZrO2–Y2O3 Ceramics. *J. Mater. Res.* **2001**, *16* (6), 1806–1813. https://doi.org/10.1557/JMR.2001.0249.

(88) Raza, M.; Boulet, P.; Pierson, J.-F.; Snyders, R.; Konstantinidis, S. Thermal Stability of Oxygen Vacancy Stabilized Zirconia (OVSZ) Thin Films. *Surf. Coat. Technol.* **2021**, *409*, 126880. https://doi.org/10.1016/j.surfcoat.2021.126880.

(89) Farid, S. B. H. 2 - Structure, Microstructure, and Properties of Bioceramics. In *Bioceramics: For Materials Science and Engineering*; Farid, S. B. H., Ed.; Woodhead Publishing Series in Biomaterials; Woodhead Publishing, 2019; pp 39–76. https://doi.org/10.1016/B978-0-08-102233-7.00002-1.

(90) Shukla, S.; Seal, S. Mechanisms of Room Temperature Metastable Tetragonal Phase Stabilisation in Zirconia. *Int. Mater. Rev.* **2005**, *50* (1), 45–64. https://doi.org/10.1179/174328005X14267.

(91) Xu, C.; He, D.; Liu, C.; Wang, H.; Wang, P.; Wang, Q.; Wang, W. Preparation of ZrO2 Whiskers through High Pressure and High Temperature Method. *Solid State Sci.* **2015**, *41*, 52–55. https://doi.org/10.1016/j.solidstatesciences.2015.01.009.

(92) Pina, S.; Rebelo, R.; Correlo, V. M.; Oliveira, J. M.; Reis, R. L. Bioceramics for Osteochondral Tissue Engineering and Regeneration. In *Osteochondral Tissue Engineering: Nanotechnology, Scaffolding-Related Developments and Translation*; Oliveira, J. M., Pina, S., Reis, R. L., San Roman, J., Eds.; Advances in Experimental Medicine and Biology; Springer International Publishing: Cham, 2018; pp 53–75. https://doi.org/10.1007/978-3-319-76711-6_3.

(93) Hadjicharalambous, C.; Mygdali, E.; Prymak, O.; Buyakov, A.; Kulkov, S.; Chatzinikolaidou, M. Proliferation and Osteogenic Response of MC3T3-E1 Pre-Osteoblastic Cells on Porous Zirconia Ceramics Stabilized with Magnesia or Yttria. *J. Biomed. Mater. Res. A* **2015**, *103* (11), 3612–3624. https://doi.org/10.1002/jbm.a.35475.

(94) Tosiriwatanapong, T.; Singhatanadgit, W. Zirconia-Based Biomaterials for Hard Tissue Reconstruction. *Bone Tissue Regen. Insights* **2018**, *9*, 1179061X18767886. https://doi.org/10.1177/1179061X18767886.

(95) Li, J.; Wang, X.; Lin, Y.; Deng, X.; Li, M.; Nan, C. In Vitro Cell Proliferation and Mechanical Behaviors Observed in Porous Zirconia Ceramics. *Materials* **2016**, *9* (4), 218. https://doi.org/10.3390/ma9040218.

(96) Han, M.-K. Advances and Challenges in Zirconia-Based Materials for Dental Applications. *J. Korean Ceram. Soc.* **2024**. https://doi.org/10.1007/s43207-024-00416-7.

(97) Yin, L.; Nakanishi, Y.; Alao, A.-R.; Song, X.-F.; Abduo, J.; Zhang, Y. A Review of Engineered Zirconia Surfaces in Biomedical Applications. *Procedia CIRP* **2017**, *65*, 284–290. https://doi.org/10.1016/j.procir.2017.04.057.

(98) Matsui, K.; Hosoi, K.; Feng, B.; Yoshida, H.; Ikuhara, Y. Ultrahigh Toughness Zirconia Ceramics. *Proc. Natl. Acad. Sci. U. S. A. 120* (27), e2304498120. https://doi.org/10.1073/pnas.2304498120.

(99) Reddy, C. V.; Reddy, I. N.; Shim, J.; Kim, D.; Yoo, K. Synthesis and Structural, Optical, Photocatalytic, and Electrochemical Properties of Undoped and Yttrium-Doped Tetragonal ZrO2 Nanoparticles. *Ceram. Int.* **2018**, *44* (11), 12329–12339. https://doi.org/10.1016/j.ceramint.2018.04.020.

(100) Imariouane, M.; Saâdaoui, M.; Denis, G.; Reveron, H.; Chevalier, J. Low-Yttria Doped Zirconia: Bridging the Gap between Strong and Tough Ceramics. *J. Eur. Ceram. Soc.* **2023**, *43* (11), 4906–4915. https://doi.org/10.1016/j.jeurceramsoc.2023.04.021.

(101) *Local structures surrounding Zr in nanostructurally stabilized cubic zirconia: Structural origin of phase stability | Journal of Applied Physics | AIP Publishing*. https://pubs.aip.org/aip/jap/article/104/11/113535/145894/Local-structures-surrounding-Zr-in (accessed 2024-08-20).

(102) *Sol–gel synthesis of tetragonal ZrO2 nanoparticles stabilized by crystallite size and oxygen vacancies | Journal of Sol-Gel Science and Technology*. https://link.springer.com/article/10.1007/s10971-013-3112-8 (accessed 2024-08-20).

(103) Liu, Y.; Chi, W.; Liu, H.; Su, Y.; Zhao, L. Preparation of T-ZrO2 by a Sol–Gel Process with Carbon as a Phase Transformation Promoter. *RSC Adv.* **2015**, *5* (43), 34451–34455. https://doi.org/10.1039/C5RA04932F.

(104) El-Fadl, A. A.; Eltokhey, A. M.; Abu-Sehly, A. A.; Abozeed, A. A. Stabilization of Tetragonal Phase of Nanostructured Fex/ZrO2 System (0 ≤ x ≤ 25) Prepared by Modified Sol-Gel Method. *Phys. Scr.* **2022**, *97* (2), 025706. https://doi.org/10.1088/1402-4896/ac4864.

(105) Kumar, S.; Bhunia, S.; Ojha, A. K. Effect of Calcination Temperature on Phase Transformation, Structural and Optical Properties of Sol–Gel Derived ZrO2 Nanostructures. *Phys. E Low-Dimens. Syst. Nanostructures* **2015**, *66*, 74–80. https://doi.org/10.1016/j.physe.2014.09.007.

(106) Meetei, S. D.; Singh, S. D. Hydrothermal Synthesis and White Light Emission of Cubic ZrO2:Eu3+ Nanocrystals. *J. Alloys Compd.* **2014**, *587*, 143–147. https://doi.org/10.1016/j.jallcom.2013.10.159.

(107) Aminipoya, H.; Ghomi, A. B.; Rayati, S. ZrO2 Nanoparticles: Optical Properties of Tetragonal Phase and Enhanced Photocatalytic Activity. **2020**, *5* (2).

(108) Qiu, H.; Huang, W.; Zhang, Y.; Chen, J.; Gao, L.; Omran, M.; Nan, L.; Chen, G. Co-Precipitation of Nano Mg–Y/ZrO2 Ternary Oxide Eutectic System: Effects of Calcination Temperature. *Ceram. Int.* **2022**, *48* (16), 23452–23459. https://doi.org/10.1016/j.ceramint.2022.04.339.

(109) *Inorganics | Free Full-Text | Tetragonal Nanosized Zirconia: Hydrothermal Synthesis and Its Performance as a Promising Ceramic Reinforcement*. https://www.mdpi.com/2304-6740/11/5/217 (accessed 2024-08-20).

(110) Reddy, Ch. V.; Babu, B.; Reddy, I. N.; Shim, J. Synthesis and Characterization of Pure Tetragonal ZrO2 Nanoparticles with Enhanced Photocatalytic Activity. *Ceram. Int.* **2018**, *44* (6), 6940–6948. https://doi.org/10.1016/j.ceramint.2018.01.123.

(111) Tahir, M. N.; Gorgishvili, L.; Li, J.; Gorelik, T.; Kolb, U.; Nasdala, L.; Tremel, W. Facile Synthesis and Characterization of Monocrystalline Cubic ZrO2 Nanoparticles. *Solid State Sci.* **2007**, *9* (12), 1105–1109. https://doi.org/10.1016/j.solidstatesciences.2007.07.033.

(112) Matias, M. L.; Carlos, E.; Branquinho, R.; Do Valle, H.; Marcelino, J.; Morais, M.; Pimentel, A.; Rodrigues, J.; Monteiro, T.; Fortunato, E.; Martins, R.; Nunes, D. A Comparison between Solution-Based Synthesis Methods of ZrO2 Nanomaterials for Energy Storage Applications. *Energies* **2022**, *15* (17), 6452. https://doi.org/10.3390/en15176452.

(113) Vidya, Y. S.; Anantharaju, K. S.; Nagabhushana, H.; Sharma, S. C.; Nagaswarupa, H. P.; Prashantha, S. C.; Shivakumara, C.; Danithkumar. Combustion Synthesized Tetragonal ZrO2: Eu3+ Nanophosphors: Structural and Photoluminescence Studies. *Spectrochim. Acta. A. Mol. Biomol. Spectrosc.* **2015**, *135*, 241–251. https://doi.org/10.1016/j.saa.2014.06.151.

(114) Gupta, S. K.; Chandrasekhar, D.; Kadam, R. M. Tetragonal ZrO2:Nd3+ Nanosphere: Combustion Synthesis, Luminescence and Photoacoustic Spectroscopy. *J. Mol. Struct.* **2015**, *1102*, 141–145. https://doi.org/10.1016/j.molstruc.2015.08.058.

(115) Prakashbabu, D.; Hari Krishna, R.; Nagabhushana, B. M.; Nagabhushana, H.; Shivakumara, C.; Chakradar, R. P. S.; Ramalingam, H. B.; Sharma, S. C.; Chandramohan, R. Low Temperature Synthesis of Pure Cubic ZrO2 Nanopowder: Structural and Luminescence Studies. *Spectrochim. Acta. A. Mol. Biomol. Spectrosc.* **2014**, *122*, 216–222. https://doi.org/10.1016/j.saa.2013.11.043.

(116) Horti, N. C.; Kamatagi, M. D.; Nataraj, S. K.; Wari, M. N.; Inamdar, S. R. Structural and Optical Properties of Zirconium Oxide (ZrO2) Nanoparticles: Effect of Calcination Temperature. *Nano Express* **2020**, *1* (1), 010022. https://doi.org/10.1088/2632-959X/ab8684.

(117) Ying, S.; Guan, Z.; Ofoegbu, P. C.; Clubb, P.; Rico, C.; He, F.; Hong, J. Green Synthesis of Nanoparticles: Current Developments and Limitations. *Environ. Technol. Innov.* **2022**, *26*, 102336. https://doi.org/10.1016/j.eti.2022.102336.

(118) Balaram, V. Potential Future Alternative Resources for Rare Earth Elements: Opportunities and Challenges. *Minerals* **2023**, *13* (3), 425. https://doi.org/10.3390/min13030425.

(119) Fan, J. H.; Omura, A.; Roca, E. Geopolitics and Rare Earth Metals. *Eur. J. Polit. Econ.* **2023**, *78*, 102356. https://doi.org/10.1016/j.ejpoleco.2022.102356.

(120) Branquinho, R.; Carlos, E.; Nunes, D.; Fortunato, E.; Martins, R. Sustainable Synthesis of Oxides for Electronics and Photocatalysis. In *Synthesis and Applications in Chemistry and Materials*; Series on Chemistry, Energy and the Environment; WORLD SCIENTIFIC, 2023; Vol. Volume 14, pp 443–482. https://doi.org/10.1142/9789811283239_0043.

(121) Mishra, S.; Debnath, A. K.; Muthe, K. P.; Das, N.; Parhi, P. Rapid Synthesis of Tetragonal Zirconia Nanoparticles by Microwave-Solvothermal Route and Its Photocatalytic Activity towards Organic Dyes and Hexavalent Chromium in Single and Binary Component Systems. *Colloids Surf. Physicochem. Eng. Asp.* **2021**, *608*, 125551. https://doi.org/10.1016/j.colsurfa.2020.125551.

(122) *Photoluminescence of Tetragonal ZrO2 Nanoparticles Synthesized by Microwave Irradiation | Inorganic Chemistry*. https://pubs.acs.org/doi/10.1021/ic025532q (accessed 2024-08-20).

(123) Frassica, M. T.; Grunlan, M. A. Perspectives on Synthetic Materials to Guide Tissue Regeneration for Osteochondral Defect Repair. *ACS Biomater. Sci. Eng.* **2020**, *6* (8), 4324–4336. https://doi.org/10.1021/acsbiomaterials.0c00753.

(124) Tamaddon, M.; Wang, L.; Liu, Z.; Liu, C. Osteochondral Tissue Repair in Osteoarthritic Joints: Clinical Challenges and Opportunities in Tissue Engineering. *Bio-Des. Manuf.* **2018**, *1* (2), 101–114. https://doi.org/10.1007/s42242-018-0015-0.

(125) Decker, R. S.; Koyama, E.; Pacifici, M. Articular Cartilage: Structural and Developmental Intricacies and Questions. *Curr. Osteoporos. Rep.* **2015**, *13* (6), 407–414. https://doi.org/10.1007/s11914-015-0290-z.

(126) Lu, X. L.; Mow, V. C. Biomechanics of Articular Cartilage and Determination of Material Properties. *Med. Sci. Sports Exerc.* **2008**, *40* (2), 193–199. https://doi.org/10.1249/mss.0b013e31815cb1fc.

(127) Guilak, F.; Jones, W. R.; Ting-Beall, H. P.; Lee, G. M. The Deformation Behavior and Mechanical Properties of Chondrocytes in Articular Cartilage. *Osteoarthritis Cartilage* **1999**, *7* (1), 59–70. https://doi.org/10.1053/joca.1998.0162.

(128) Nahian, A.; Sapra, A. Histology, Chondrocytes. In *StatPearls [Internet]*; StatPearls Publishing, 2023.

(129) Lin, X.; Patil, S.; Gao, Y.-G.; Qian, A. The Bone Extracellular Matrix in Bone Formation and Regeneration. *Front. Pharmacol.* **2020**, *11*, 757. https://doi.org/10.3389/fphar.2020.00757.

(130) Zhu, X.; Chan, Y. T.; Yung, P. S. H.; Tuan, R. S.; Jiang, Y. Subchondral Bone Remodeling: A Therapeutic Target for Osteoarthritis. *Front. Cell Dev. Biol.* **2021**, *8*. https://doi.org/10.3389/fcell.2020.607764.

(131) Binks, D. A.; Gravallese, E. M.; Bergin, D.; Hodgson, R. J.; Tan, A. L.; Matzelle, M. M.; McGonagle, D.; Radjenovic, A. Role of Vascular Channels as a Novel Mechanism for Subchondral Bone Damage at Cruciate Ligament Entheses in Osteoarthritis and Inflammatory Arthritis. *Ann. Rheum. Dis.* **2015**, *74* (1), 196–203. https://doi.org/10.1136/annrheumdis-2013-203972.

(132) Säämänen, A.-M.; Arokoski, J. P. A.; Jurvelin, J. S.; Kiviranta, I. 1 - The Structure and Regenerative Capacity of Synovial Joint Tissues. In *Regenerative Medicine and Biomaterials for the Repair of Connective Tissues*; Archer, C., Ralphs, J., Eds.; Woodhead Publishing Series in Biomaterials; Woodhead Publishing, 2010; pp 1–38. https://doi.org/10.1533/9781845697792.1.

(133) Martel-Pelletier, J.; Lajeunesse, D.; Reboul, P.; Pelletier, J.-P. Chapter 2 - The Role of Subchondral Bone in Osteoarthritis. In *Osteoarthritis*; Sharma, L., Berenbaum, F., Eds.; Mosby: Philadelphia, 2007; pp 15–32.

(134) Gonçalves, A. M.; Moreira, A.; Weber, A.; Williams, G. R.; Costa, P. F. Osteochondral Tissue Engineering: The Potential of Electrospinning and Additive Manufacturing. *Pharmaceutics* **2021**, *13* (7), 983. https://doi.org/10.3390/pharmaceutics13070983.

(135) Zhou, L.; Gjvm, V. O.; Malda, J.; Stoddart, M. J.; Lai, Y.; Richards, R. G.; Ki-wai Ho, K.; Qin, L. Innovative Tissue-Engineered Strategies for Osteochondral Defect Repair and Regeneration: Current Progress and Challenges. *Adv. Healthc. Mater.* **2020**, *9* (23), 2001008. https://doi.org/10.1002/adhm.202001008.

(136) Dinoro, J.; Maher, M.; Talebian, S.; Jafarkhani, M.; Mehrali, M.; Orive, G.; Foroughi, J.; Lord, M. S.; Dolatshahi-Pirouz, A. Sulfated Polysaccharide-Based Scaffolds for Orthopaedic Tissue Engineering. *Biomaterials* **2019**, *214*, 119214. https://doi.org/10.1016/j.biomaterials.2019.05.025.

(137) Maglio, M.; Brogini, S.; Pagani, S.; Giavaresi, G.; Tschon, M. Current Trends in the Evaluation of Osteochondral Lesion Treatments: Histology, Histomorphometry, and Biomechanics in Preclinical Models. *BioMed Res. Int.* **2019**, *2019* (1), 4040236. https://doi.org/10.1155/2019/4040236.

(138) Babaniamansour, P.; Salimi, M.; Dorkoosh, F.; Mohammadi, M. Magnetic Hydrogel for Cartilage Tissue Regeneration as Well as a Review on Advantages and Disadvantages of Different Cartilage Repair Strategies. *BioMed Res. Int.* **2022**, *2022*, 7230354. https://doi.org/10.1155/2022/7230354.

(139) Howell, M.; Liao, Q.; Gee, C. W. Surgical Management of Osteochondral Defects of the Knee: An Educational Review. *Curr. Rev. Musculoskelet. Med.* **2021**, *14* (1), 60–66. https://doi.org/10.1007/s12178-020-09685-1.

(140) Farag, M. M. Recent Trends on Biomaterials for Tissue Regeneration Applications: Review. *J. Mater. Sci.* **2023**, *58* (2), 527–558. https://doi.org/10.1007/s10853-022-08102-x.

(141) Fu, J.-N.; Wang, X.; Yang, M.; Chen, Y.-R.; Zhang, J.-Y.; Deng, R.-H.; Zhang, Z.-N.; Yu, J.-K.; Yuan, F.-Z. Scaffold-Based Tissue Engineering Strategies for Osteochondral Repair. *Front. Bioeng. Biotechnol.* **2022**, *9*, 812383. https://doi.org/10.3389/fbioe.2021.812383.

(142) Ye, M.; Shi, B. Zirconia Nanoparticles-Induced Toxic Effects in Osteoblast-Like 3T3-E1 Cells. *Nanoscale Res. Lett.* **2018**, *13*, 353. https://doi.org/10.1186/s11671-018-2747-3.

(143) Sun, Y.; Sun, J.; Wu, X.; Li, Y.; Li, X.; Li, R.; Wang, T.; Bi, W.; Cui, W.; Yu, Y. Mechanism of Zirconia Microgroove Surface Structure for Osseointegration. *Mater. Today Adv.* **2021**, *12*, 100159. https://doi.org/10.1016/j.mtadv.2021.100159.

(144) A. Bapat, R.; Jan Yang, H.; V. Chaubal, T.; Dharmadhikari, S.; Mohamed Abdulla, A.; Arora, S.; Rawal, S.; Kesharwani, P. Review on Synthesis, Properties and Multifarious Therapeutic Applications of Nanostructured Zirconia in Dentistry. *RSC Adv.* **2022**, *12* (20), 12773–12793. https://doi.org/10.1039/D2RA00006G.

(145) Sotoudeh, A.; Jahanshahi, A.; Takhtfooladi, M. A.; Bazazan, A.; Ganjali, A.; Harati, M. P. Study on Nano-Structured Hydroxyapatite/Zirconia Stabilized Yttria on Healing of Articular Cartilage Defect in Rabbit. *Acta Cir. Bras.* **2013**, *28* (5), 340–345. https://doi.org/10.1590/s0102-86502013000500004.

(146) Buduneli, N. Anatomy of Periodontal Tissues. In *Biomarkers in Periodontal Health and Disease: Rationale, Benefits, and Future Directions*; Buduneli, N., Ed.; Springer International Publishing: Cham, 2020; pp 1–7. https://doi.org/10.1007/978-3-030-37317-7_1.

(147) Jakovljevic, A.; Nikolic, N.; Paternò Holtzman, L.; Tournier, P.; Gaudin, A.; Cordaro, L.; Milinkovic, I. Involvement of the Notch Signaling System in Alveolar Bone Resorption. *Jpn. Dent. Sci. Rev.* **2023**, *59*, 38–47. https://doi.org/10.1016/j.jdsr.2023.02.003.

(148) Perinpanayagam, H.; Martin, T.; Mithal, V.; Dahman, M.; Marzec, N.; Lampasso, J.; Dziak, R. Alveolar Bone Osteoblast Differentiation and Runx2/Cbfa1 Expression. *Arch. Oral Biol.* **2006**, *51* (5), 406–415. https://doi.org/10.1016/j.archoralbio.2005.09.004.

(149) Hollý, D.; Klein, M.; Mazreku, M.; Zamborský, R.; Polák, Š.; Danišovič, Ľ.; Csöbönyeiová, M. Stem Cells and Their Derivatives—Implications for Alveolar Bone Regeneration: A Comprehensive Review. *Int. J. Mol. Sci.* **2021**, *22* (21), 11746. https://doi.org/10.3390/ijms222111746.

(150) Gulabivala, K.; Ng, Y.-L. 1 - Tooth Organogenesis, Morphology and Physiology. In *Endodontics (Fourth Edition)*; Gulabivala, K., Ng, Y.-L., Eds.; Mosby, 2014; pp 2–32. https://doi.org/10.1016/B978-0-7020-3155-7.00001-1.

(151) Trulsson, M. Sensory-Motor Function of Human Periodontal Mechanoreceptors. *J. Oral Rehabil.* **2006**, *33* (4), 262–273. https://doi.org/10.1111/j.1365-2842.2006.01629.x.

(152) Ivanovski, S.; Gronthos, S.; Shi, S.; Bartold, P. Stem Cells in the Periodontal Ligament. *Oral Dis.* **2006**, *12* (4), 358–363. https://doi.org/10.1111/j.1601-0825.2006.01253.x.

(153) Nanci, A.; Bosshardt, D. D. Structure of Periodontal Tissues in Health and Disease. *Periodontol. 2000* **2006**, *40* (1), 11–28. https://doi.org/10.1111/j.1600-0757.2005.00141.x.

(154) Chapter 9 - Periodontium. In *Ten Cate's Oral Histology (Eighth Edition)*; Nanci, A., Ed.; Mosby: St. Louis (MO), 2013; pp 205–232. https://doi.org/10.1016/B978-0-323-07846-7.00009-4.

(155) Hughes, F. J. Chapter 34 - Periodontium and Periodontal Disease. In *Stem Cell Biology and Tissue Engineering in Dental Sciences*; Vishwakarma, A., Sharpe, P., Shi, S., Ramalingam, M., Eds.; Academic Press: Boston, 2015; pp 433–444. https://doi.org/10.1016/B978-0-12-397157-9.00038-2.

(156) Arzate, H.; Zeichner-David, M.; Mercado-Celis, G. Cementum Proteins: Role in Cementogenesis, Biomineralization, Periodontium Formation and Regeneration. *Periodontol. 2000* **2015**, *67* (1), 211–233. https://doi.org/10.1111/prd.12062.

(157) Koller, A.; Sapra, A. Anatomy, Head and Neck, Oral Gingiva. In *StatPearls*; StatPearls Publishing: Treasure Island (FL), 2024.

(158) Torabi, S.; Soni, A. Histology, Periodontium. In *StatPearls*; StatPearls Publishing: Treasure Island (FL), 2024.

(159) Bartold, P. M.; Walsh, L. J.; Narayanan, A. S. Molecular and Cell Biology of the Gingiva. *Periodontol. 2000* **2000**, *24*, 28–55. https://doi.org/10.1034/j.1600-0757.2000.2240103.x.

(160) Santos, M. S.; dos Santos, A. B.; Carvalho, M. S. New Insights in Hydrogels for Periodontal Regeneration. *J. Funct. Biomater.* **2023**, *14* (11), 545. https://doi.org/10.3390/jfb14110545.

(161) Sanz, M.; D'Aiuto, F.; Deanfield, J.; Fernandez-Avilés, F. European Workshop in Periodontal Health and Cardiovascular Disease—Scientific Evidence on the Association between Periodontal and Cardiovascular Diseases: A Review of the Literature. *Eur. Heart J. Suppl.* **2010**, *12* (suppl_B), B3–B12. https://doi.org/10.1093/eurheartj/suq003.

(162) *Oral health*. https://www.who.int/news-room/fact-sheets/detail/oral-health (accessed 2024-08-23).

(163) Usui, M.; Onizuka, S.; Sato, T.; Kokabu, S.; Ariyoshi, W.; Nakashima, K. Mechanism of Alveolar Bone Destruction in Periodontitis — Periodontal Bacteria and Inflammation. *Jpn. Dent. Sci. Rev.* **2021**, *57*, 201–208. https://doi.org/10.1016/j.jdsr.2021.09.005.

(164) *Periodontal (Gum) Disease | National Institute of Dental and Craniofacial Research*. https://www.nidcr.nih.gov/research/data-statistics/periodontal-disease (accessed 2024-08-25).

(165) Alqahtani, A. M. Guided Tissue and Bone Regeneration Membranes: A Review of Biomaterials and Techniques for Periodontal Treatments. *Polymers* **2023**, *15* (16), 3355. https://doi.org/10.3390/polym15163355.

(166) Swanson, W. B.; Yao, Y.; Mishina, Y. Novel Approaches for Periodontal Tissue Engineering. *genesis* **2022**, *60* (8–9), e23499. https://doi.org/10.1002/dvg.23499.

(167) Zhu, Y.; Tao, C.; Goh, C.; Shrestha, A. Innovative Biomaterials for the Treatment of Periodontal Disease. *Front. Dent. Med.* **2023**, *4*. https://doi.org/10.3389/fdmed.2023.1163562.

(168) Zong, C.; Bronckaers, A.; Willems, G.; He, H.; Cadenas de Llano-Pérula, M. Nanomaterials for Periodontal Tissue Regeneration: Progress, Challenges and Future Perspectives. *J. Funct. Biomater.* **2023**, *14* (6), 290. https://doi.org/10.3390/jfb14060290.

(169) Galli, M.; Yao, Y.; Giannobile, W. V.; Wang, H.-L. Current and Future Trends in Periodontal Tissue Engineering and Bone Regeneration. *Plast. Aesthetic Res.* **2021**, *8*, 3. https://doi.org/10.20517/2347-9264.2020.176.

(170) Bannunah, A. M. Biomedical Applications of Zirconia-Based Nanomaterials: Challenges and Future Perspectives. *Molecules* **2023**, *28* (14), 5428. https://doi.org/10.3390/molecules28145428.

(171) Yürük, G.; Damla Demir, Y.; Vural, Ş.; Seda Kehr, N. Polymeric Biomaterials for Periodontal Tissue Engineering and Periodontitis. *RSC Appl. Polym.* **2024**, *2* (4), 534–556. https://doi.org/10.1039/D4LP00001C.

(172) Bannunah, A. M. Biomedical Applications of Zirconia-Based Nanomaterials: Challenges and Future Perspectives. *Molecules* **2023**, *28* (14), 5428. https://doi.org/10.3390/molecules28145428.

(173) Hossain, N.; Mobarak, M. H.; Hossain, A.; Khan, F.; Mim, J. J.; Chowdhury, M. A. Advances of Plant and Biomass Extracted Zirconium Nanoparticles in Dental Implant Application. *Heliyon* **2023**, *9* (5), e15973. https://doi.org/10.1016/j.heliyon.2023.e15973.

(174) Theodoridis, K.; Arampatzis, A. S.; Liasi, G.; Tsalikis, L.; Barmpalexis, P.; Christofilos, D.; Assimopoulou, A. N. 3D-Printed Antibacterial Scaffolds for the Regeneration of Alveolar Bone in Severe Periodontitis. *Int. J. Mol. Sci.* **2023**, *24* (23), 16754. https://doi.org/10.3390/ijms242316754.

(175) Ekambaram, R.; Paraman, V.; Raja, L.; Suresh, M. K.; Dharmalingam, S. Design and Development of Electrospun SPEEK Incorporated with Aminated Zirconia and *Curcumin* Nanofibers for Periodontal Regeneration. *J. Mech. Behav. Biomed. Mater.* **2021**, *123*, 104796. https://doi.org/10.1016/j.jmbbm.2021.104796.

(176) Khan, I.; Neumann, C.; Sinha, M. Chapter 24 - Tissue Regeneration and Reprogramming. In *Wound Healing, Tissue Repair, and Regeneration in Diabetes*; Bagchi, D., Das, A., Roy, S., Eds.; Academic Press, 2020; pp 515–534. https://doi.org/10.1016/B978-0-12-816413-6.00024-1.

(177) Singh, M. R.; Patel, S.; Singh, D. Chapter 9 - Natural Polymer-Based Hydrogels as Scaffolds for Tissue Engineering. In *Nanobiomaterials in Soft Tissue Engineering*; Grumezescu, A. M., Ed.; William Andrew Publishing, 2016; pp 231–260. https://doi.org/10.1016/B978-0-323-42865-1.00009-X.

(178) Almeida, H. V.; Sathy, B. N.; Dudurych, I.; Buckley, C. T.; O'Brien, F. J.; Kelly, D. J. Anisotropic Shape-Memory Alginate Scaffolds Functionalized with Either Type I or Type II Collagen for Cartilage Tissue Engineering. *Tissue Eng. Part A* **2017**, *23* (1–2), 55–68. https://doi.org/10.1089/ten.tea.2016.0055.

(179) Lee, K. Y.; Mooney, D. J. Alginate: Properties and Biomedical Applications. *Prog. Polym. Sci.* **2012**, *37* (1), 106–126. https://doi.org/10.1016/j.progpolymsci.2011.06.003.

(180) Roato, I.; Masante, B.; Putame, G.; Massai, D.; Mussano, F. Challenges of Periodontal Tissue Engineering: Increasing Biomimicry through 3D Printing and Controlled Dynamic Environment. *Nanomater. Basel Switz.* **2022**, *12* (21), 3878. https://doi.org/10.3390/nano12213878.

(181) Choe, R. H.; Kuzemchak, B. C.; Kotsanos, G. J.; Mirdamadi, E.; Sherry, M.; Devoy, E.; Lowe, T.; Packer, J. D.; Fisher, J. P. Designing Biomimetic 3D-Printed Osteochondral Scaffolds for Enhanced Load-Bearing Capacity. *Tissue Eng. Part A* **2024**, *30* (13–14), 409–420. https://doi.org/10.1089/ten.TEA.2023.0217.

(182) Ghanbari, M.; Salavati-Niasari, M.; Mohandes, F.; Firouzi, Z.; Mousavi, S.-D. The Impact of Zirconium Oxide Nanoparticles Content on Alginate Dialdehyde-Gelatin Scaffolds in Cartilage Tissue Engineering. *J. Mol. Liq.* **2021**, *335*, 116531. https://doi.org/10.1016/j.molliq.2021.116531.

(183) El-Rashidy, A. A.; El Moshy, S.; Radwan, I. A.; Rady, D.; Abbass, M. M. S.; Dörfer, C. E.; Fawzy El-Sayed, K. M. Effect of Polymeric Matrix Stiffness on Osteogenic Differentiation of Mesenchymal Stem/Progenitor Cells: Concise Review. *Polymers* **2021**, *13* (17), 2950. https://doi.org/10.3390/polym13172950.

(184) Na, J.; Yang, Z.; Shi, Q.; Li, C.; Liu, Y.; Song, Y.; Li, X.; Zheng, L.; Fan, Y. Extracellular Matrix Stiffness as an Energy Metabolism Regulator Drives Osteogenic Differentiation in Mesenchymal Stem Cells. *Bioact. Mater.* **2024**, *35*, 549–563. https://doi.org/10.1016/j.bioactmat.2024.02.003.

(185) Chevalier, J.; Gremillard, L.; Virkar, A. V.; Clarke, D. R. The Tetragonal-Monoclinic Transformation in Zirconia: Lessons Learned and Future Trends. *J. Am. Ceram. Soc.* **2009**, *92* (9), 1901–1920. https://doi.org/10.1111/j.1551-2916.2009.03278.x.

(186) Kunrath, M. F.; Gupta, S.; Lorusso, F.; Scarano, A.; Noumbissi, S. Oral Tissue Interactions and Cellular Response to Zirconia Implant-Prosthetic Components: A Critical Review. *Materials* **2021**, *14* (11), 2825. https://doi.org/10.3390/ma14112825.

(187) Afzal, A. Implantable Zirconia Bioceramics for Bone Repair and Replacement: A Chronological Review. *Mater. Express* **2014**, *4* (1), 1–12. https://doi.org/10.1166/mex.2014.1148.

(188) Yusuf, D.; Maryani, E.; Mardhian, D. F.; Noviyanti, A. R. Evaluation of Structural Stability, Mechanical Properties, and Corrosion Resistance of Magnesia Partially Stabilized Zirconia (Mg-PSZ). *Molecules* **2023**, *28* (16), 6054. https://doi.org/10.3390/molecules28166054.

(189) Mbae, J. K.; Muthui, Z. W. Doping Induced Phase Stabilization and Electronic Properties of Alkaline Earth Metal Doped Zirconium (IV) Oxide: A First Principles Study. *Heliyon* **2023**, *9* (10), e20998. https://doi.org/10.1016/j.heliyon.2023.e20998.

(190) de Souza, E. F.; Appel, L. G. Oxygen Vacancy Formation and Their Role in the CO2 Activation on Ca Doped ZrO2 Surface: An *Ab-Initio* DFT Study. *Appl. Surf. Sci.* **2021**, *553*, 149589. https://doi.org/10.1016/j.apsusc.2021.149589.

(191) *Oxygen vacancy ordering induced displacements of cations in yttria-stabilized zirconia | AIP Advances | AIP Publishing*. https://pubs.aip.org/aip/adv/article/6/9/095113/867717/Oxygen-vacancy-ordering-induced-displacements-of (accessed 2024-08-28).

(192) Karapetrova, E.; Platzer, R.; Gardner, J. A.; Torne, E.; Sommers, J. A.; Evenson, W. E. Oxygen Vacancies in Pure Tetragonal Zirconia Powders: Dependence on the Presence of Chlorine during Processing. *J. Am. Ceram. Soc.* **2001**, *84* (1), 65–70. https://doi.org/10.1111/j.1151-2916.2001.tb00609.x.

(193) Kim, H. S.; Kim, Y.-J.; Son, Y. R.; Pham, V. N.; Kim, K.; Kim, C. W.; Youn, Y.-S.; Kwon, O.-H.; Lee, H. Verifying the Relationships of Defect Site and Enhanced Photocatalytic Properties of Modified ZrO2 Nanoparticles Evaluated by In-Situ Spectroscopy and STEM-EELS. *Sci. Rep.* **2022**, *12* (1), 11295. https://doi.org/10.1038/s41598-022-15557-0.

(194) Safonov, A. A.; Bagatur'yants, A. A.; Korkin, A. A. Oxygen Vacancies in Tetragonal ZrO2: Ab Initio Embedded Cluster Calculations. *Microelectron. Eng.* **2003**, *69* (2), 629–632. https://doi.org/10.1016/S0167-9317(03)00355-1.

(195) Qi, F.; Yang, Z.; Wang, Y.; Qiu, Q.; Li, H. Defects in Black Zirconia Responsible for Solar Energy Harvesting. *J. Mater. Chem. C* **2021**, *9* (46), 16732–16740. https://doi.org/10.1039/D1TC03914H.

(196) Assessment, U. E. N. C. for E. *Sol-gel synthesis of tetragonal ZrO2 nanoparticles stabilized by crystallite size and oxygen vacancies*. https://hero.epa.gov/hero/index.cfm/reference/details/reference_id/2277224 (accessed 2024-08-20).

(197) Shi, R.-J.; Lang, J.-Q.; Wang, T.; Zhou, N.; Ma, M.-G. Fabrication, Properties, and Biomedical Applications of Calcium-Containing Cellulose-Based Composites. *Front. Bioeng. Biotechnol.* **2022**, *10*, 937266. https://doi.org/10.3389/fbioe.2022.937266.

(198) Benetti, F.; de Oliveira, P. H. C.; de Andrade, M. P. B.; Cantiga-Silva, C.; Sivieri-Araújo, G.; Dezan Júnior, E.; Gomes-Filho, J. E.; Diniz, I. M. A.; dos Reis-Prado, A. H.; Souza, M. T.; Zanotto, E. D.; Cintra, L. T. A. Cytotoxicity, Biocompatibility, and Calcium Deposition Capacity of 45S5 Bioglass Experimental Paste and Bio-C Temp: In Vitro and In Vivo Study Using Wistar Rats. *J. Funct. Biomater.* **2024**, *15* (7), 184. https://doi.org/10.3390/jfb15070184.

(199) Matias, M. L.; Carlos, E.; Branquinho, R.; do Valle, H.; Marcelino, J.; Morais, M.; Pimentel, A.; Rodrigues, J.; Monteiro, T.; Fortunato, E.; Martins, R.; Nunes, D. A Comparison between Solution-Based Synthesis Methods of ZrO2 Nanomaterials for Energy Storage Applications. *Energies* **2022**, *15* (17), 6452. https://doi.org/10.3390/en15176452.

(200) 14:00-17:00. *ISO 9277:2010*. ISO. https://www.iso.org/standard/44941.html (accessed 2024-09-03).

(201) Phillippi, C. M.; Mazdiyasni, K. S. Infrared and Raman Spectra of Zirconia Polymorphs. *J. Am. Ceram. Soc.* **1971**, *54* (5), 254–258. https://doi.org/10.1111/j.1151-2916.1971.tb12283.x.

(202) Sinhamahapatra, A.; Jeon, J.-P.; Kang, J.; Han, B.; Yu, J.-S. Oxygen-Deficient Zirconia (ZrO2-x): A New Material for Solar Light Absorption. *Sci. Rep.* **2016**, *6*, 27218. https://doi.org/10.1038/srep27218.

(203) Soares, M. R. N.; Holz, T.; Oliveira, F.; Costa, F. M.; Monteiro, T. Tunable Green to Red ZrO2:Er Nanophosphors. *RSC Adv.* **2015**, *5* (26), 20138–20147. https://doi.org/10.1039/C5RA00189G.

(204) Margueron, S.; Bartasyte, A. Temperature-Dependent Resonant Raman Scattering of Yttria Doped Zirconia Phases in Thermal Barrier Coatings. *J. Eur. Ceram. Soc.* **2024**, *44* (1), 419–425. https://doi.org/10.1016/j.jeurceramsoc.2023.08.046.

(205) Ding, S.; Zhao, J.; Yu, Q. Effect of Zirconia Polymorph on Vapor-Phase Ketonization of Propionic Acid. *Catalysts* **2019**, *9* (9), 768. https://doi.org/10.3390/catal9090768.

(206) Matias, M. L.; Carlos, E.; Branquinho, R.; do Valle, H.; Marcelino, J.; Morais, M.; Pimentel, A.; Rodrigues, J.; Monteiro, T.; Fortunato, E.; Martins, R.; Nunes, D. A Comparison between Solution-Based Synthesis Methods of ZrO_2 Nanomaterials for Energy Storage Applications. *Energies* **2022**, *15(17)* (17), 6452. https://doi.org/10.3390/EN15176452/S1.

(207) Merle, T.; Guinebretiere, R.; Mirgorodsky, A.; Quintard, P. Polarized Raman Spectra of Tetragonal Pure ${\mathrm{ZrO}}_{2}$ Measured on Epitaxial Films. *Phys. Rev. B* **2002**, *65* (14), 144302. https://doi.org/10.1103/PhysRevB.65.144302.

(208) Guo, M.; Wang, G.; Zhao, Y.; Li, H.; Tang, K.; Zhao, Y.; Burgess, K. Preparation of Nano-ZrO2 Powder via a Microwave-Assisted Hydrothermal Method. *Ceram. Int.* **2021**, *47* (9), 12425–12432. https://doi.org/10.1016/j.ceramint.2021.01.099.

(209) Kontoyannis, C. G.; Carountzos, G. Quantitative Determination of the Cubic-to-Monoclinic Phase Transformation in Fully Stabilized Zirconias by Raman Spectroscopy. *J. Am. Ceram. Soc.* **1994**, *77* (8), 2191–2194. https://doi.org/10.1111/j.1151-2916.1994.tb07117.x.

(210) *High Pressure Surface Science and Engineering*; Gogotsi, Y., Domnich, V., Eds.; CRC Press: Boca Raton, 2019. https://doi.org/10.1201/9780429144097.

(211) Kontoyannis, C. G.; Orkoula, M. Quantitative Determination of the Cubic, Tetragonal and Monoclinic Phases in Partially Stabilized Zirconias by Raman Spectroscopy. *J. Mater. Sci.* **1994**, *29* (20), 5316–5320. https://doi.org/10.1007/BF01171541.

(212) Zhou, Z.; Yu, Y.; Ding, Z.; Zuo, M.; Jing, C. Modulating High-Index Facets on Anatase TiO2. *Eur. J. Inorg. Chem.* **2018**, *2018* (6), 683–693. https://doi.org/10.1002/ejic.201701027.

(213) Meng, J.; Lan, Z.; Castelli, I. E.; Zheng, K. Atomic-Scale Observation of Oxygen Vacancy-Induced Step Reconstruction in WO3. *J. Phys. Chem. C* **2021**, *125* (15), 8456–8460. https://doi.org/10.1021/acs.jpcc.1c01577.

(214) Liu, J.; Mir, A. H.; He, G.; Danaie, M.; Hinks, J.; Donnelly, S.; Nordin, H.; Lozano-Perez, S.; Grovenor, C. R. M. In-Situ TEM Study of Irradiation-Induced Damage Mechanisms in Monoclinic-ZrO2. *Acta Mater.* **2020**, *199*, 429–442. https://doi.org/10.1016/j.actamat.2020.08.064.

(215) Courtney-Davies, L.; Ciobanu, C. L.; Verdugo-Ihl, M. R.; Slattery, A.; Cook, N. J.; Dmitrijeva, M.; Keyser, W.; Wade, B. P.; Domnick, U. I.; Ehrig, K.; Xu, J.; Kontonikas-Charos, A. Zircon at the Nanoscale Records Metasomatic Processes Leading to Large Magmatic–Hydrothermal Ore Systems. *Minerals* **2019**, *9* (6), 364. https://doi.org/10.3390/min9060364.

(216) *Control of coordinatively unsaturated Zr sites in ZrO2 for efficient C–H bond activation | Nature Communications*. https://www.nature.com/articles/s41467-018-06174-5 (accessed 2024-09-03).

(217) O'Connell, J. H.; Lee, M. E.; Skuratov, V. A.; Rymzhanov, R. A. SHI Induced Tetragonal Tracks in Natural Zirconia. *Nucl. Instrum. Methods Phys. Res. Sect. B Beam Interact. Mater. At.* **2020**, *473*, 1–5. https://doi.org/10.1016/j.nimb.2020.04.002.

(218) Jiang, J.; Ding, W.; Zhang, W.; Li, H. Defect-Rich ZrO2 Anchored Pd Nanoparticles for Selective Hydrodeoxygenation of Bio-Models at Room Temperature. *Fuel* **2022**, *318*, 123529. https://doi.org/10.1016/j.fuel.2022.123529.

(219) Feng, B.; Kumamoto, A.; Matsui, K.; Tanemura, M.; Yoshiya, M.; Yoshida, H.; Ikuhara, Y. Surface Segregation of 3 Mol % Yttria-Doped Tetragonal Zirconia Particle Studied by Atomic-Resolution Scanning Transmission Electron Microscopy-Energy-Dispersive X-Ray Spectroscopy. *J. Ceram. Soc. Jpn.* **2021**, *129* (9), 561–565. https://doi.org/10.2109/jcersj2.21032.

(220) Behtash, M.; Wong, J.; Jiang, S.; Luo, J.; Yang, K. First-Principles Study of Impurity Segregation in Zirconia, Hafnia, and Yttria-Stabilized-Zirconia Grain Boundaries. *J. Eur. Ceram. Soc.* **2019**, *39* (13), 3812–3820. https://doi.org/10.1016/j.jeurceramsoc.2019.04.039.

(221) Sun, Y.; Hara, S. Atomistic Study of Segregation and Diffusion of Yttrium and Calcium Cations near Electrolyte Surfaces in Solid Oxide Fuel Cells. *J. Eur. Ceram. Soc.* **2015**, *35* (11), 3063–3074. https://doi.org/10.1016/j.jeurceramsoc.2015.04.015.

(222) Prado-Gonjal, J.; Gutiérrez-Seijas, J.; Ansorregui, I. H.; Morán, E.; Terry, I.; Schmidt, R. The Role of Defects in Microwave and Conventionally Synthesized LaCoO3 Perovskite. *J. Eur. Ceram. Soc.* **2016**, *36* (5), 1197–1206. https://doi.org/10.1016/j.jeurceramsoc.2015.12.014.

(223) Gu, W.; Wang, W.; Li, G.; Xie, H.; Wong, P. K.; An, T. Microwave-Assisted Synthesis of Defective Tungsten Trioxide for Photocatalytic Bacterial Inactivation: Role of the Oxygen Vacancy. *Chin. J. Catal.* **2020**, *41* (10), 1488–1497. https://doi.org/10.1016/S1872-2067(19)63409-1.

(224) Kabongo, G.; G, N.; K, O.; S, D. Microwave Irradiation Induces Oxygen Vacancy in Metal Oxides Based Materials and Devices: A Review. In *Journal of Nanosciences: Current Research*; 2018; Vol. 03. https://doi.org/10.4172/2572-0813.1000125.

(225) Yoshida, K.; Sonobe, T.; Zen, H.; Hachiya, K.; Okumura, K.; Mishima, K.; Inukai, M.; Negm, H.; Torgasin, K.; Omer, M.; Kinjo, R.; Kii, T.; Masuda, K.; Ohgaki, H. Effect of Microwave Irradiation on the Electronic Structure of ZnO. *J. Phys. Chem. Solids* **2015**, *83*, 47–51. https://doi.org/10.1016/j.jpcs.2015.03.013.

(226) Li, T.; Shen, Z.; Shu, Y.; Li, X.; Jiang, C.; Chen, W. Facet-Dependent Evolution of Surface Defects in Anatase TiO2 by Thermal Treatment: Implications for Environmental Applications of Photocatalysis. *Environ. Sci. Nano* **2019**, *6* (6), 1740–1753. https://doi.org/10.1039/C9EN00264B.

(227) Singh, S.; Nalwa, H. S. Nanotechnology and Health Safety – Toxicity and Risk Assessments of Nanostructured Materials on Human Health. *J. Nanosci. Nanotechnol.* **2007**, *7* (9), 3048–3070. https://doi.org/10.1166/jnn.2007.922.

(228) Mediouni, N.; Guillard, C.; Dappozze, F.; Khrouz, L.; Parola, S.; Colbeau-Justin, C.; Amara, A. B. H.; Rhaiem, H. B.; Jaffrezic-Renault, N.; Namour, P. Impact of Structural Defects on the Photocatalytic Properties of ZnO. *J. Hazard. Mater. Adv.* **2022**, *6*, 100081. https://doi.org/10.1016/j.hazadv.2022.100081.

(229) Guo, M. Y.; Ng, A. M. C.; Liu, F.; Djurišić, A. B.; Chan, W. K.; Su, H.; Wong, K. S. Effect of Native Defects on Photocatalytic Properties of ZnO. *J. Phys. Chem. C* **2011**, *115* (22), 11095–11101. https://doi.org/10.1021/jp200926u.

(230) Manivasakan, P.; Rajendran, V.; Ranjan Rauta, P.; Bandhu Sahu, B.; Krushna Panda, B. Synthesis of Monoclinic and Cubic ZrO2 Nanoparticles from Zircon. *J. Am. Ceram. Soc.* **2011**, *94* (5), 1410–1420. https://doi.org/10.1111/j.1551-2916.2010.04277.x.

(231) *Iodinated SnO2 Quantum Dots: A Facile and Efficient Approach To Increase Solar Absorption for Visible-Light Photocatalysis | The Journal of Physical Chemistry C*. https://pubs.acs.org/doi/10.1021/acs.jpcc.6b01530 (accessed 2024-09-03).

(232) Kumar, S.; Mir, I. A.; Mathpal, M. C.; Muhammad, Z.; Rehman, S. U.; Hui, K. N.; Zhu, L. One-Step Hydrothermal Synthesis of High Surface Area m-ZrO2 Nanorings with Lower Band Gap, Blue Emission and High Photocatalytic Activity. *J. Mater. Sci. Mater. Electron.* **2019**, *30* (17), 15923–15927. https://doi.org/10.1007/s10854-019-01943-4.

(233) Chen, F.; Hong, Q.; Xu, G.-Q.; Andy Hor, T. S.; Shen, S. DADD-Assisted Hydrothermal Synthesis of t-ZrO2 Nanoparticles. *J. Am. Ceram. Soc.* **2005**, *88* (9), 2649–2651. https://doi.org/10.1111/j.1551-2916.2005.00487.x.

(234) Xu, G.; Zhang, Y.; Liao, C.; Yan, C. Hydrothermal Synthesis of Weakly Agglomerated Nanocrystalline Scandia-Stabilized Zirconia. *J. Am. Ceram. Soc.* **2002**, *85* (4), 995–997. https://doi.org/10.1111/j.1151-2916.2002.tb00207.x.

(235) *Materials | Free Full-Text | Influence of Surface Defects and Size on Photochemical Properties of SnO2 Nanoparticles*. https://www.mdpi.com/1996-1944/11/6/904 (accessed 2024-09-03).

(236) Gaharwar, A. K.; Singh, I.; Khademhosseini, A. Engineered Biomaterials for in Situ Tissue Regeneration. *Nat. Rev. Mater.* **2020**, *5* (9), 686–705. https://doi.org/10.1038/s41578-020-0209-x.

(237) Gonzalez-Vilchis, R. A.; Piedra-Ramirez, A.; Patiño-Morales, C. C.; Sanchez-Gomez, C.; Beltran-Vargas, N. E. Sources, Characteristics, and Therapeutic Applications of Mesenchymal Cells in Tissue Engineering. *Tissue Eng. Regen. Med.* **2022**, *19* (2), 325–361. https://doi.org/10.1007/s13770-021-00417-1.

(238) Kim, Y.-H.; Vijayavenkataraman, S.; Cidonio, G. Biomaterials and Scaffolds for Tissue Engineering and Regenerative Medicine. *BMC Methods* **2024**, *1* (1), 2. https://doi.org/10.1186/s44330-024-00002-7.

(239) Eldeeb, A. E.; Salah, S.; Elkasabgy, N. A. Biomaterials for Tissue Engineering Applications and Current Updates in the Field: A Comprehensive Review. *AAPS PharmSciTech* **2022**, *23* (7), 267. https://doi.org/10.1208/s12249-022-02419-1.

(240) Sahoo, D. R.; Biswal, T. Alginate and Its Application to Tissue Engineering. *SN Appl. Sci.* **2021**, *3* (1), 30. https://doi.org/10.1007/s42452-020-04096-w.

(241) Abka-khajouei, R.; Tounsi, L.; Shahabi, N.; Patel, A. K.; Abdelkafi, S.; Michaud, P. Structures, Properties and Applications of Alginates. *Mar. Drugs* **2022**, *20* (6), 364. https://doi.org/10.3390/md20060364.

(242) Gill, A. S.; Deol, P. K.; Kaur, I. P. An Update on the Use of Alginate in Additive Biofabrication Techniques. *Curr. Pharm. Des.* **2019**, *25* (11), 1249–1264. https://doi.org/10.2174/1381612825666190423155835.

(243) Guillaume, O.; Naqvi, S. M.; Lennon, K.; Buckley, C. T. Enhancing Cell Migration in Shape-Memory Alginate-Collagen Composite Scaffolds: In Vitro and Ex Vivo Assessment for Intervertebral Disc Repair. *J. Biomater. Appl.* **2015**, *29* (9), 1230–1246. https://doi.org/10.1177/0885328214557905.

(244) Guillaume, O.; Daly, A.; Lennon, K.; Gansau, J.; Buckley, S. F.; Buckley, C. T. Shape-Memory Porous Alginate Scaffolds for Regeneration of the Annulus Fibrosus: Effect of TGF-B3 Supplementation and Oxygen Culture Conditions. *Acta Biomater.* **2014**, *10* (5), 1985–1995. https://doi.org/10.1016/j.actbio.2013.12.037.

(245) Saghati, S.; Rahbarghazi, R.; Karkan, S. F.; Nazifkerdar, S.; Khoshfetrat, A. B.; Nasrabadi, H. T. Shape Memory Polymers in Osteochondral Tissue Engineering. *J. Res. Clin. Med.* **2022**, *10* (1), 30–30. https://doi.org/10.34172/jrcm.2022.030.

(246) Zhang, X.; Yang, Y.; Yang, Z.; Ma, R.; Aimaijiang, M.; Xu, J.; Zhang, Y.; Zhou, Y. Four-Dimensional Printing and Shape Memory Materials in Bone Tissue Engineering. *Int. J. Mol. Sci.* **2023**, *24* (1), 814. https://doi.org/10.3390/ijms24010814.

(247) Lyu, J.; Chen, H.; Luo, J.; Lin, S.; Yang, G.; Zhou, M.; Tao, J. Shape Memory and Hemostatic Silk-Laponite Scaffold for Alveolar Bone Regeneration after Tooth Extraction Trauma. *Int. J. Biol. Macromol.* **2024**, *260*, 129454. https://doi.org/10.1016/j.ijbiomac.2024.129454.

(248) Zhang, W.; Yu, M.; Cao, Y.; Zhuang, Z.; Zhang, K.; Chen, D.; Liu, W.; Yin, J. An Anti-Bacterial Porous Shape Memory Self-Adaptive Stiffened Polymer for Alveolar Bone Regeneration after Tooth Extraction. *Bioact. Mater.* **2023**, *21*, 450–463. https://doi.org/10.1016/j.bioactmat.2022.08.030.

(249) Staples, R. J.; Ivanovski, S.; Vaquette, C. Fibre Guiding Scaffolds for Periodontal Tissue Engineering. *J. Periodontal Res.* **2020**, *55* (3), 331–341. https://doi.org/10.1111/jre.12729.

(250) Ashworth, J. C.; Mehr, M.; Buxton, P. G.; Best, S. M.; Cameron, R. E. Optimising Collagen Scaffold Architecture for Enhanced Periodontal Ligament Fibroblast Migration. *J. Mater. Sci. Mater. Med.* **2018**, *29* (11), 166. https://doi.org/10.1007/s10856-018-6175-9.

(251) Oliveira, J. M.; Ribeiro, V. P.; Reis, R. L. Advances on Gradient Scaffolds for Osteochondral Tissue Engineering. *Prog. Biomed. Eng.* **2021**, *3* (3), 033001. https://doi.org/10.1088/2516-1091/abfc2c.

(252) Ghanbari, M.; Salavati-Niasari, M.; Mohandes, F.; Firouzi, Z.; Mousavi, S.-D. The Impact of Zirconium Oxide Nanoparticles Content on Alginate Dialdehyde-Gelatin Scaffolds in Cartilage Tissue Engineering. *J. Mol. Liq.* **2021**, *335*, 116531. https://doi.org/10.1016/j.molliq.2021.116531.

(253) Osorio-Arciniega, R.; García-Hipólito, M.; Alvarez-Fregoso, O.; Alvarez-Perez, M. A. Composite Fiber Spun Mat Synthesis and In Vitro Biocompatibility for Guide Tissue Engineering. *Molecules* **2021**, *26* (24), 7597. https://doi.org/10.3390/molecules26247597.

(254) Weng, W.; Wu, W.; Hou, M.; Liu, T.; Wang, T.; Yang, H. Review of Zirconia-Based Biomimetic Scaffolds for Bone Tissue Engineering. *J. Mater. Sci.* **2021**, *56* (14), 8309–8333. https://doi.org/10.1007/s10853-021-05824-2.

(255) Assal, P. A. The Osseointegration of Zirconia Dental Implants. *Schweiz. Monatsschrift Zahnmed. Rev. Mens. Suisse Odonto-Stomatol. Riv. Mens. Svizzera Odontol. E Stomatol.* **2013**, *123* (7–8), 644–654.

(256) Jeyaraman, M.; Jeyaraman, N.; Nallakumarasamy, A.; Ramasubramanian, S.; Yadav, S. Critical Challenges and Frontiers in Cartilage Tissue Engineering. *Cureus 16* (1), e53095. https://doi.org/10.7759/cureus.53095.

(257) Kashte, S.; Jaiswal, A. K.; Kadam, S. Artificial Bone via Bone Tissue Engineering: Current Scenario and Challenges. *Tissue Eng. Regen. Med.* **2017**, *14* (1), 1–14. https://doi.org/10.1007/s13770-016-0001-6.

(258) Teimouri, A.; Ebrahimi, R.; Emadi, R.; Beni, B. H.; Chermahini, A. N. Nano-Composite of Silk Fibroin–Chitosan/Nano ZrO2 for Tissue Engineering Applications: Fabrication and Morphology. *Int. J. Biol. Macromol.* **2015**, *76*, 292–302. https://doi.org/10.1016/j.ijbiomac.2015.02.023.

(259) Pattnaik, S.; Nethala, S.; Tripathi, A.; Saravanan, S.; Moorthi, A.; Selvamurugan, N. Chitosan Scaffolds Containing Silicon Dioxide and Zirconia Nano Particles for Bone Tissue Engineering. *Int. J. Biol. Macromol.* **2011**, *49* (5), 1167–1172. https://doi.org/10.1016/j.ijbiomac.2011.09.016.

(260) *Development of a Sodium Alginate/Chitosan Nanocomposite Scaffold Incorporating Zircon Nanoparticles-Hydroxyapatite, and Alendronic Acid for Bone Tissue Engineering*. https://www.ijcce.ac.ir/article_708934.html (accessed 2024-09-24).

(261) Shanmugam, B. K.; Rangaraj, S.; Subramani, K.; Srinivasan, S.; Kandhasamy, N.; Arumugam, K.; Periyasamy, M.; Aicher, W. K.; Venkatachalam, R. Biomimetic Development of Chitosan and Sodium Alginate-Based Nanocomposites Contains Zirconia for Tissue Engineering Applications. *J. Biomed. Mater. Res. B Appl. Biomater.* **2022**, *110* (8), 1942–1955. https://doi.org/10.1002/jbm.b.35052.

(262) Singh, A. P.; Kaur, N.; Kumar, A.; Singh, K. L. Preparation of Fully Cubic Calcium-Stabilized Zirconia With 10 Mol% Calcium Oxide Dopant Concentration by Microwave Processing. *J. Am. Ceram. Soc.* **2007**, *90* (3), 789–796. https://doi.org/10.1111/j.1551-2916.2006.01379.x.

(263) Biotteau-Deheuvels, K.; Zych, L.; Gremillard, L.; Chevalier, J. Effects of Ca-, Mg- and Si-Doping on Microstructures of Alumina–Zirconia Composites. *J. Eur. Ceram. Soc.* **2012**, *32* (11), 2711–2721. https://doi.org/10.1016/j.jeurceramsoc.2011.11.011.

(264) Beto, J. A. The Role of Calcium in Human Aging. *Clin. Nutr. Res.* **2015**, *4* (1), 1–8. https://doi.org/10.7762/cnr.2015.4.1.1.

(265) Rathinam, E.; Govindarajan, S.; Rajasekharan, S.; Declercq, H.; Elewaut, D.; De Coster, P.; Martens, L.; Leybaert, L. The Calcium Dynamics of Human Dental Pulp Stem Cells Stimulated with Tricalcium Silicate-Based Cements Determine Their Differentiation and Mineralization Outcome. *Sci. Rep.* **2021**, *11* (1), 645. https://doi.org/10.1038/s41598-020-80096-5.

(266) Aquino-Martínez, R.; Artigas, N.; Gámez, B.; Rosa, J. L.; Ventura, F. Extracellular Calcium Promotes Bone Formation from Bone Marrow Mesenchymal Stem Cells by Amplifying the Effects of BMP-2 on SMAD Signalling. *PLoS ONE* **2017**, *12* (5), e0178158. https://doi.org/10.1371/journal.pone.0178158.

(267) Khalifa, G. M.; Kahil, K.; Addadi, L.; Weiner, S. Calcium Ion and Mineral Pathways in Biomineralization: A Perspective. In *Biomineralization*; Endo, K., Kogure, T., Nagasawa, H., Eds.; Springer: Singapore, 2018; pp 97–103. https://doi.org/10.1007/978-981-13-1002-7_10.

(268) Follet, H.; Boivin, G.; Rumelhart, C.; Meunier, P. J. The Degree of Mineralization Is a Determinant of Bone Strength: A Study on Human Calcanei. *Bone* **2004**, *34* (5), 783–789. https://doi.org/10.1016/j.bone.2003.12.012.

(269) Gorski, J. P. Biomineralization of Bone: A Fresh View of the Roles of Non-Collagenous Proteins. *Front. Biosci. Landmark Ed.* **2011**, *16*, 2598–2621.

(270) Zhang, J.; Wu, L.; Jing, D.; Ding, J. A Comparative Study of Porous Scaffolds with Cubic and Spherical Macropores. *Polymer* **2005**, *46* (13), 4979–4985. https://doi.org/10.1016/j.polymer.2005.02.120.

(271) yadav, P.; Beniwal, G.; Saxena, K. K. A Review on Pore and Porosity in Tissue Engineering. *Mater. Today Proc.* **2021**, *44*, 2623–2628. https://doi.org/10.1016/j.matpr.2020.12.661.

(272) *Alginic acid, sodium salt (Algin) – scipoly.com*. https://scipoly.com/shop/alginic-acid-sodium-salt-2/ (accessed 2024-07-16).

(273) Barbosa, F.; Garrudo, F. F. F.; Alberte, P. S.; Resina, L.; Carvalho, M. S.; Jain, A.; Marques, A. C.; Estrany, F.; Rawson, F. J.; Aléman, C.; Ferreira, F. C.; Silva, J. C. Hydroxyapatite-Filled Osteoinductive and Piezoelectric Nanofibers for Bone Tissue Engineering. *Sci. Technol. Adv. Mater.* **2023**, *24* (1), 2242242. https://doi.org/10.1080/14686996.2023.2242242.

(274) 14:00-17:00. *ISO 10993-12:2021*. ISO. https://www.iso.org/standard/75769.html (accessed 2024-09-05).

(275) 14:00-17:00. *ISO 10993-5:2009*. ISO. https://www.iso.org/standard/36406.html (accessed 2024-09-04).

(276) Adel, I. M.; ElMeligy, M. F.; Elkasabgy, N. A. Conventional and Recent Trends of Scaffolds Fabrication: A Superior Mode for Tissue Engineering. *Pharmaceutics* **2022**, *14* (2), 306. https://doi.org/10.3390/pharmaceutics14020306.

(277) Hefft, D. I.; Adeutnji, C. O. Chapter 8 - Alginate in Food and Beverage Formulations. In *Applications of Seaweeds in Food and Nutrition*; Hefft, D. I., Adetunji, C. O., Eds.; Elsevier, 2024; pp 115–128. https://doi.org/10.1016/B978-0-323-91803-9.00017-2.

(278) Chen, G.; Ushida, T.; Tateishi, T. Scaffold Design for Tissue Engineering. *Macromol. Biosci.* **2002**, *2* (2), 67–77. https://doi.org/10.1002/1616-5195(20020201)2:2<67::AID-MABI67>3.0.CO;2-F.

(279) Jodati, H.; Yılmaz, B.; Evis, Z. A Review of Bioceramic Porous Scaffolds for Hard Tissue Applications: Effects of Structural Features. *Ceram. Int.* **2020**, *46* (10, Part B), 15725–15739. https://doi.org/10.1016/j.ceramint.2020.03.192.

(280) Loh, Q. L.; Choong, C. Three-Dimensional Scaffolds for Tissue Engineering Applications: Role of Porosity and Pore Size. *Tissue Eng. Part B Rev.* **2013**, *19* (6), 485–502. https://doi.org/10.1089/ten.teb.2012.0437.

(281) Zhang, Y.; Fan, W.; Ma, Z.; Wu, C.; Fang, W.; Liu, G.; Xiao, Y. The Effects of Pore Architecture in Silk Fibroin Scaffolds on the Growth and Differentiation of Mesenchymal Stem Cells Expressing BMP7. *Acta Biomater.* **2010**, *6* (8), 3021–3028. https://doi.org/10.1016/j.actbio.2010.02.030.

(282) Guagnini, B.; Medagli, B.; Zumbo, B.; Cannillo, V.; Turco, G.; Porrelli, D.; Bellucci, D. Alginate-Sr/Mg Containing Bioactive Glass Scaffolds: The Characterization of a New 3D Composite for Bone Tissue Engineering. *J. Funct. Biomater.* **2024**, *15* (7), 183. https://doi.org/10.3390/jfb15070183.

(283) Soleimani, M.; Asgharzadeh Salmasi, A.; Asghari, S.; Joneidi Yekta, H.; Kamyab Moghadas, B.; Shahriari, S.; Saber-Samandari, S.; Khandan, A. Optimization and Fabrication of Alginate Scaffold for Alveolar Bone Regeneration with Sufficient Drug Release. *Int. Nano Lett.* **2021**, *11* (3), 295–305. https://doi.org/10.1007/s40089-021-00342-0.

(284) Peter, M.; Binulal, N. S.; Nair, S. V.; Selvamurugan, N.; Tamura, H.; Jayakumar, R. Novel Biodegradable Chitosan–Gelatin/Nano-Bioactive Glass Ceramic Composite Scaffolds for Alveolar Bone Tissue Engineering. *Chem. Eng. J.* **2010**, *158* (2), 353–361. https://doi.org/10.1016/j.cej.2010.02.003.

(285) Savić Gajić, I. M.; Savić, I. M.; Svirčev, Z. Preparation and Characterization of Alginate Hydrogels with High Water-Retaining Capacity. *Polymers* **2023**, *15* (12), 2592. https://doi.org/10.3390/polym15122592.

(286) Kesharwani, P.; Bisht, A.; Alexander, A.; Dave, V.; Sharma, S. Biomedical Applications of Hydrogels in Drug Delivery System: An Update. *J. Drug Deliv. Sci. Technol.* **2021**, *66*, 102914. https://doi.org/10.1016/j.jddst.2021.102914.

(287) Zhai, N.; Wang, B. Preparation of Fast-Swelling Porous Superabsorbent Hydrogels with High Saline Water Absorbency under Pressure by Foaming and Post Surface Crosslinking. *Sci. Rep.* **2023**, *13*, 13815. https://doi.org/10.1038/s41598-023-40563-1.

(288) Li, Z.; Sun, X.; Chen, X.; Wang, H.; Li, D.; Shang, T.; Qi, L.; Yan, H.; Lin, Q. Effects of TiO2 Nanoparticles on the Physicochemical and Biological Properties of Oxidized Sodium Alginate/Polyacrylamide-Gelatin Composite Hydrogels Fabricated by Interpenetrating Network Approach. *React. Funct. Polym.* **2023**, *191*, 105679. https://doi.org/10.1016/j.reactfunctpolym.2023.105679.

(289) Babić Radić, M. M.; Vukomanović, M.; Nikodinović-Runić, J.; Tomić, S. Gelatin-/Alginate-Based Hydrogel Scaffolds Reinforced with TiO2 Nanoparticles for Simultaneous Release of Allantoin, Caffeic Acid, and Quercetin as Multi-Target Wound Therapy Platform. *Pharmaceutics* **2024**, *16* (3), 372. https://doi.org/10.3390/pharmaceutics16030372.

(290) Kessler, M.; Yuan, T.; Kolinski, J. M.; Amstad, E. Influence of the Degree of Swelling on the Stiffness and Toughness of Microgel-Reinforced Hydrogels. *Macromol. Rapid Commun.* **2023**, *44* (16), 2200864. https://doi.org/10.1002/marc.202200864.

(291) Cheung, H.-Y.; Lau, K.-T.; Lu, T.-P.; Hui, D. A Critical Review on Polymer-Based Bio-Engineered Materials for Scaffold Development. *Compos. Part B Eng.* **2007**, *38* (3), 291–300. https://doi.org/10.1016/j.compositesb.2006.06.014.

(292) Madhavan Nampoothiri, K.; Nair, N. R.; John, R. P. An Overview of the Recent Developments in Polylactide (PLA) Research. *Bioresour. Technol.* **2010**, *101* (22), 8493–8501. https://doi.org/10.1016/j.biortech.2010.05.092.

(293) Karchoubi, F.; Afshar Ghotli, R.; Pahlevani, H.; Baghban Salehi, M. New Insights into Nanocomposite Hydrogels; a Review on Recent Advances in Characteristics and Applications. *Adv. Ind. Eng. Polym. Res.* **2024**, *7* (1), 54–78. https://doi.org/10.1016/j.aiepr.2023.06.002.

(294) Liebschner, M.; Bucklen, B.; Wettergreen, M. Mechanical Aspects of Tissue Engineering. *Semin. Plast. Surg.* **2005**, *19* (3), 217–228. https://doi.org/10.1055/s-2005-919717.

(295) Vincent, L.; Engler, A. J. 5.504 - Effect of Substrate Modulus on Cell Function and Differentiation. In *Comprehensive Biomaterials*; Ducheyne, P., Ed.; Elsevier: Oxford, 2011; pp 51–63. https://doi.org/10.1016/B978-0-08-055294-1.00158-6.

(296) Parfenyuk, E. V.; Dolinina, E. S. Silica Hydrogel Composites as a Platform for Soft Drug Formulations and Cosmetic Compositions. *Mater. Chem. Phys.* **2022**, *287*, 126160. https://doi.org/10.1016/j.matchemphys.2022.126160.

(297) Gaharwar, A. K.; Peppas, N. A.; Khademhosseini, A. Nanocomposite Hydrogels for Biomedical Applications. *Biotechnol. Bioeng.* **2014**, *111* (3), 441–453. https://doi.org/10.1002/bit.25160.

(298) Luo, T.; Tan, B.; Zhu, L.; Wang, Y.; Liao, J. A Review on the Design of Hydrogels With Different Stiffness and Their Effects on Tissue Repair. *Front. Bioeng. Biotechnol.* **2022**, *10*. https://doi.org/10.3389/fbioe.2022.817391.

(299) Trujillo, S.; Seow, M.; Lueckgen, A.; Salmeron-Sanchez, M.; Cipitria, A. Dynamic Mechanical Control of Alginate-Fibronectin Hydrogels with Dual Crosslinking: Covalent and Ionic. *Polymers* **2021**, *13* (3), 433. https://doi.org/10.3390/polym13030433.

(300) Schulz, A.; Gepp, M. M.; Stracke, F.; von Briesen, H.; Neubauer, J. C.; Zimmermann, H. Tyramine-conjugated Alginate Hydrogels as a Platform for Bioactive Scaffolds. *J. Biomed. Mater. Res. A* **2019**, *107* (1), 114–121. https://doi.org/10.1002/jbm.a.36538.

(301) Doyle, S. E.; Snow, F.; Duchi, S.; O'Connell, C. D.; Onofrillo, C.; Di Bella, C.; Pirogova, E. 3D Printed Multiphasic Scaffolds for Osteochondral Repair: Challenges and Opportunities. *Int. J. Mol. Sci.* **2021**, *22* (22), 12420. https://doi.org/10.3390/ijms222212420.

(302) Benazzi, S.; Nguyen, H. N.; Kullmer, O.; Hublin, J.-J. Unravelling the Functional Biomechanics of Dental Features and Tooth Wear. *PLoS ONE* **2013**, *8* (7), e69990. https://doi.org/10.1371/journal.pone.0069990.

(303) Sefton, M. V.; Uludag, H.; Babensee, J.; Roberts, T.; Horvath, V.; De Boni, U. 22 - Microencapsulation of Cells in Thermoplastic Copolymer (Hydroxyethyl Methacrylate–Methyl Methacrylate). In *Methods in Neurosciences*; Flanagan, T. R., Emerich, D. F., Winn, S. R., Eds.; Providing Pharmacological Access to the Brain; Academic Press, 1994; Vol. 21, pp 371–386. https://doi.org/10.1016/B978-0-12-185291-7.50028-X.

(304) Ghasemi, M.; Turnbull, T.; Sebastian, S.; Kempson, I. The MTT Assay: Utility, Limitations, Pitfalls, and Interpretation in Bulk and Single-Cell Analysis. *Int. J. Mol. Sci.* **2021**, *22* (23), 12827. https://doi.org/10.3390/ijms222312827.

(305) *In Vitro Cytotoxicity Assay on Gold Nanoparticles with Different Stabilizing Agents - Vijayakumar - 2012 - Journal of Nanomaterials - Wiley Online Library*. https://onlinelibrary.wiley.com/doi/10.1155/2012/734398 (accessed 2024-08-07).

(306) Kong, B.; Seog, J. H.; Graham, L. M.; Lee, S. B. Experimental Considerations on the Cytotoxicity of Nanoparticles. *Nanomed.* **2011**, *6* (5), 929–941. https://doi.org/10.2217/nnm.11.77.

(307) Gruber, S.; Nickel, A. Toxic or Not Toxic? The Specifications of the Standard ISO 10993-5 Are Not Explicit Enough to Yield Comparable Results in the Cytotoxicity Assessment of an Identical Medical Device. *Front. Med. Technol.* **2023**, *5*, 1195529. https://doi.org/10.3389/fmedt.2023.1195529.

(308) *Polymers | Free Full-Text | The Preliminary Assessment of New Biomaterials Necessitates a Comparison of Direct and Indirect Cytotoxicity Methodological Approaches*. https://www.mdpi.com/2073-4360/14/21/4522 (accessed 2024-08-07).

(309) Theiszová, M.; Jantová, S.; Dragúnová, J.; Grznárová, P.; Palou, M. Comparison the Cytotoxicity of Hydroxyapatite Measured by Direct Cell Counting and MTT Test in Murine Fibroblast NIH-3T3 Cells. *Biomed. Pap. Med. Fac. Univ. Palacky Olomouc Czechoslov.* **2005**, *149* (2), 393–396.

(310) McLaughlin, M.; J. Earle, M.; A. Gîlea, M.; F. Gilmore, B.; P. Gorman, S.; R. Seddon, K. Cytotoxicity of 1-Alkylquinolinium Bromide Ionic Liquids in Murine Fibroblast NIH 3T3 Cells. *Green Chem.* **2011**, *13* (10), 2794–2800. https://doi.org/10.1039/C0GC00813C.

(311) Sun, J.; Tan, H. Alginate-Based Biomaterials for Regenerative Medicine Applications. *Materials* **2013**, *6* (4), 1285–1309. https://doi.org/10.3390/ma6041285.

(312) Wang, J.; Yin, W.; He, X.; Wang, Q.; Guo, M.; Chen, S. Good Biocompatibility and Sintering Properties of Zirconia Nanoparticles Synthesized via Vapor-Phase Hydrolysis. *Sci. Rep.* **2016**, *6* (1), 35020. https://doi.org/10.1038/srep35020.

(313) Bannunah, A. M. Biomedical Applications of Zirconia-Based Nanomaterials: Challenges and Future Perspectives. *Molecules* **2023**, *28* (14), 5428. https://doi.org/10.3390/molecules28145428.

(314) Al-Nasiry, S.; Geusens, N.; Hanssens, M.; Luyten, C.; Pijnenborg, R. The Use of Alamar Blue Assay for Quantitative Analysis of Viability, Migration and Invasion of Choriocarcinoma Cells. *Hum. Reprod.* **2007**, *22* (5), 1304–1309. https://doi.org/10.1093/humrep/dem011.

(315) Gloeckner, H.; Jonuleit, T.; Lemke, H.-D. Monitoring of Cell Viability and Cell Growth in a Hollow-Fiber Bioreactor by Use of the Dye Alamar Blue™. *J. Immunol. Methods* **2001**, *252* (1), 131–138. https://doi.org/10.1016/S0022-1759(01)00347-7.

(316) Tsiapalis, D.; Ribeiro, S.; De Pieri, A.; Sallent, I.; Guillaumin, S.; Gaspar, D.; Korntner, S.; Bayon, Y.; Gomes, M. E.; Reis, R. L.; Zeugolis, D. I. Designing Microenvironments for Optimal Outcomes in Tissue Engineering and Regenerative Medicine: From Biopolymers to Culturing Conditions. In *Encyclopedia of Tissue Engineering and Regenerative Medicine*; Reis, R. L., Ed.; Academic Press: Oxford, 2019; pp 119–130. https://doi.org/10.1016/B978-0-12-801238-3.11140-7.

(317) Silva, J. C.; Meneses, J.; Garrudo, F. F. F.; Fernandes, S. R.; Alves, N.; Ferreira, F. C.; Pascoal-Faria, P. Direct Coupled Electrical Stimulation towards Improved Osteogenic Differentiation of Human Mesenchymal Stem/Stromal Cells: A Comparative Study of Different Protocols. *Sci. Rep.* **2024**, *14* (1), 5458. https://doi.org/10.1038/s41598-024-55234-y.

(318) Yousefi, A.-M.; James, P. F.; Akbarzadeh, R.; Subramanian, A.; Flavin, C.; Oudadesse, H. Prospect of Stem Cells in Bone Tissue Engineering: A Review. *Stem Cells Int.* **2016**, *2016* (1), 6180487. https://doi.org/10.1155/2016/6180487.

(319) Bernardo, M. E.; Emons, J. A. M.; Karperien, M.; Nauta, A. J.; Willemze, R.; Roelofs, H.; Romeo, S.; Marchini, A.; Rappold, G. A.; Vukicevic, S.; Locatelli, F.; Fibbe, W. E. Human Mesenchymal Stem Cells Derived from Bone Marrow Display a Better Chondrogenic Differentiation Compared with Other Sources. *Connect. Tissue Res.* **2007**, *48* (3), 132–140. https://doi.org/10.1080/03008200701228464.

(320) Tomokiyo, A.; Wada, N.; Maeda, H. Periodontal Ligament Stem Cells: Regenerative Potency in Periodontium. *Stem Cells Dev.* **2019**, *28* (15), 974–985. https://doi.org/10.1089/scd.2019.0031.

(321) Serrano-Lotina, A.; Portela, R.; Baeza, P.; Alcolea-Rodriguez, V.; Villarroel, M.; Ávila, P. Zeta Potential as a Tool for Functional Materials Development. *Catal. Today* **2023**, *423*, 113862. https://doi.org/10.1016/j.cattod.2022.08.004.

(322) Declercq, H. A.; Desmet, T.; Dubruel, P.; Cornelissen, M. J. The Role of Scaffold Architecture and Composition on the Bone Formation by Adipose-Derived Stem Cells. *Tissue Eng. Part A* **2014**, *20* (1–2), 434–444. https://doi.org/10.1089/ten.tea.2013.0179.

(323) Lee, M.; Wu, B. M.; Dunn, J. C. Y. Effect of Scaffold Architecture and Pore Size on Smooth Muscle Cell Growth. *J. Biomed. Mater. Res. A* **2008**, *87A* (4), 1010–1016. https://doi.org/10.1002/jbm.a.31816.

(324) Chan, B. P.; Leong, K. W. Scaffolding in Tissue Engineering: General Approaches and Tissue-Specific Considerations. *Eur. Spine J.* **2008**, *17* (Suppl 4), 467–479. https://doi.org/10.1007/s00586-008-0745-3.

(325) Dechant, R.; Peter, M. Nutrient Signals Driving Cell Growth. *Curr. Opin. Cell Biol.* **2008**, *20* (6), 678–687. https://doi.org/10.1016/j.ceb.2008.09.009.

(326) Tatapudy, S.; Aloisio, F.; Barber, D.; Nystul, T. Cell Fate Decisions: Emerging Roles for Metabolic Signals and Cell Morphology. *EMBO Rep.* **2017**, *18* (12), 2105–2118. https://doi.org/10.15252/embr.201744816.

(327) Hojat, N.; Gentile, P.; Ferreira, A. M.; Šiller, L. Automatic Pore Size Measurements from Scanning Electron Microscopy Images of Porous Scaffolds. *J. Porous Mater.* **2023**, *30* (1), 93–101. https://doi.org/10.1007/s10934-022-01309-y.

(328) Muthukumar, T.; Song, J. E.; Khang, G. Biological Role of Gellan Gum in Improving Scaffold Drug Delivery, Cell Adhesion Properties for Tissue Engineering Applications. *Molecules* **2019**, *24* (24), 4514. https://doi.org/10.3390/molecules24244514.

(329) Assunção, M.; Dehghan-Baniani, D.; Yiu, C. H. K.; Später, T.; Beyer, S.; Blocki, A. Cell-Derived Extracellular Matrix for Tissue Engineering and Regenerative Medicine. *Front. Bioeng. Biotechnol.* **2020**, *8*. https://doi.org/10.3389/fbioe.2020.602009.

(330) Carlson, B. M. Chapter 2 - Tissues. In *The Human Body*; Carlson, B. M., Ed.; Academic Press, 2019; pp 27–63. https://doi.org/10.1016/B978-0-12-804254-0.00002-8.

(331) Koch, M.; Włodarczyk-Biegun, M. K. Faithful Scanning Electron Microscopic (SEM) Visualization of 3D Printed Alginate-Based Scaffolds. bioRxiv March 20, 2020, p 2020.03.18.997668. https://doi.org/10.1101/2020.03.18.997668.

(332) Kamada, R.; Tano, F.; Kudoh, F.; Kimura, N.; Chuman, Y.; Osawa, A.; Namba, K.; Tanino, K.; Sakaguchi, K. Effective Cellular Morphology Analysis for Differentiation Processes by a Fluorescent 1,3a,6a-Triazapentalene Derivative Probe in Live Cells. *PLoS ONE* **2016**, *11* (8), e0160625. https://doi.org/10.1371/journal.pone.0160625.

(333) Paluch, E.; Heisenberg, C.-P. Biology and Physics of Cell Shape Changes in Development. *Curr. Biol.* **2009**, *19* (17), R790–R799. https://doi.org/10.1016/j.cub.2009.07.029.

(334) Pazmino Betancourt, B. A.; Florczyk, S. J.; Simon, M.; Juba, D.; Douglas, J. F.; Keyrouz, W.; Bajcsy, P.; Lee, C.; Simon, C. G. Effect of the Scaffold Microenvironment on Cell Polarizability and Capacitance Determined by Probabilistic Computations. *Biomed. Mater. Bristol Engl.* **2018**, *13* (2), 025012. https://doi.org/10.1088/1748-605X/aa9650.

(335) Zhao, X.; Li, Q.; Guo, Z.; Li, Z. Constructing a Cell Microenvironment with Biomaterial Scaffolds for Stem Cell Therapy. *Stem Cell Res. Ther.* **2021**, *12* (1), 583. https://doi.org/10.1186/s13287-021-02650-w.

(336) Park, J. S.; Chu, J. S.; Tsou, A. D.; Diop, R.; Tang, Z.; Wang, A.; Li, S. The Effect of Matrix Stiffness on the Differentiation of Mesenchymal Stem Cells in Response to TGF-β. *Biomaterials* **2011**, *32* (16), 3921–3930. https://doi.org/10.1016/j.biomaterials.2011.02.019.

(337) Zhu, L.; Luo, D.; Liu, Y. Effect of the Nano/Microscale Structure of Biomaterial Scaffolds on Bone Regeneration. *Int. J. Oral Sci.* **2020**, *12*, 6. https://doi.org/10.1038/s41368-020-0073-y.

(338) Kladko, D. V.; Falchevskaya, A. S.; Serov, N. S.; Prilepskii, A. Y. Nanomaterial Shape Influence on Cell Behavior. *Int. J. Mol. Sci.* **2021**, *22* (10), 5266. https://doi.org/10.3390/ijms22105266.

(339) Berniak, K.; Ura, D. P.; Piórkowski, A.; Stachewicz, U. Cell–Material Interplay in Focal Adhesion Points. *ACS Appl. Mater. Interfaces* **2024**, *16* (8), 9944–9955. https://doi.org/10.1021/acsami.3c19035.

(340) Ciobanasu, C.; Faivre, B.; Le Clainche, C. Actin Dynamics Associated with Focal Adhesions. *Int. J. Cell Biol.* **2012**, *2012*, 941292. https://doi.org/10.1155/2012/941292.

(341) *Mechanosensors in integrin signaling: The emerging role of p130Cas - ScienceDirect*. https://www.sciencedirect.com/science/article/pii/S0171933514000673 (accessed 2024-07-30).

(342) *Using biomaterials to study stem cell mechanotransduction, growth and differentiation - McMurray - 2015 - Journal of Tissue Engineering and Regenerative Medicine - Wiley Online Library*. https://onlinelibrary.wiley.com/doi/full/10.1002/term.1957 (accessed 2024-07-30).

(343) *The Bumpy Road to Stem Cell Therapies: Rational Design of Surface Topographies to Dictate Stem Cell Mechanotransduction and Fate | ACS Applied Materials & Interfaces*. https://pubs.acs.org/doi/full/10.1021/acsami.1c22109 (accessed 2024-07-30).

(344) *Synergistic Effect of Cell-Derived Extracellular Matrices and Topography on Osteogenesis of Mesenchymal Stem Cells | ACS Applied Materials & Interfaces*. https://pubs.acs.org/doi/10.1021/acsami.0c05012 (accessed 2024-07-30).

(345) *Mechanism of regulation of stem cell differentiation by matrix stiffness | Stem Cell Research & Therapy*. https://link.springer.com/article/10.1186/s13287-015-0083-4 (accessed 2024-07-31).

(346) Trivedi, S.; Srivastava, K.; Gupta, A.; Saluja, T. S.; Kumar, S.; Mehrotra, D.; Singh, S. K. A Quantitative Method to Determine Osteogenic Differentiation Aptness of Scaffold. *J. Oral Biol. Craniofacial Res.* **2020**, *10* (2), 158–160. https://doi.org/10.1016/j.jobcr.2020.04.006.

(347) Yang, L.; Ge, L.; Zhou, Q.; Mokabber, T.; Pei, Y.; Bron, R.; van Rijn, P. Biomimetic Multiscale Hierarchical Topography Enhances Osteogenic Differentiation of Human Mesenchymal Stem Cells. *Adv. Mater. Interfaces* **2020**, *7* (14), 2000385. https://doi.org/10.1002/admi.202000385.

(348) Chen, Y.; Long, S.; Liu, Z.; Wang, W.; Yuan, P.; Yang, Z.; Yang, Z.; Shi, Y.; He, F. Effects of Electrospun Membrane Surface Morphology on Cellular Behaviours and Osteogenesis of Bone Marrow Mesenchymal Stem Cells. *Mater. Res. Express* **2023**, *10* (6), 065005. https://doi.org/10.1088/2053-1591/ace02c.

(349) Pawelec, K. M.; Confalonieri, D.; Ehlicke, F.; van Boxtel, H. A.; Walles, H.; Kluijtmans, S. G. J. M. Osteogenesis and Mineralization of Mesenchymal Stem Cells in Collagen Type I-Based Recombinant Peptide Scaffolds. *J. Biomed. Mater. Res. A* **2017**, *105* (7), 1856–1866. https://doi.org/10.1002/jbm.a.36049.

(350) Estes, B. T.; Guilak, F. Three-Dimensional Culture Systems to Induce Chondrogenesis of Adipose-Derived Stem Cells. In *Adipose-Derived Stem Cells: Methods and Protocols*; Gimble, J. M., Bunnell, B. A., Eds.; Humana Press: Totowa, NJ, 2011; pp 201–217. https://doi.org/10.1007/978-1-61737-960-4_15.

(351) Kohli, N.; Wright, K. T.; Sammons, R. L.; Jeys, L.; Snow, M.; Johnson, W. E. B. An In Vitro Comparison of the Incorporation, Growth, and Chondrogenic Potential of Human Bone Marrow versus Adipose Tissue Mesenchymal Stem Cells in Clinically Relevant Cell Scaffolds Used for Cartilage Repair. *CARTILAGE* **2015**, *6* (4), 252–263. https://doi.org/10.1177/1947603515589650.

(352) Iwata, T.; Kaneda-Ikeda, E.; Takahashi, K.; Takeda, K.; Nagahara, T.; Kajiya, M.; Sasaki, S.; Ishida, S.; Yoshioka, M.; Matsuda, S.; Ouhara, K.; Fujita, T.; Kurihara, H.; Mizuno, N. Regulation of Osteogenesis in Bone Marrow-Derived Mesenchymal Stem Cells via Histone Deacetylase 1 and 2 Co-Cultured with Human Gingival Fibroblasts and Periodontal Ligament Cells. *J. Periodontal Res.* **2023**, *58* (1), 83–96. https://doi.org/10.1111/jre.13070.

(353) Queiroz, A.; Albuquerque-Souza, E.; Gasparoni, L. M.; de França, B. N.; Pelissari, C.; Trierveiler, M.; Holzhausen, M. Therapeutic Potential of Periodontal Ligament Stem Cells. *World J. Stem Cells* **2021**, *13* (6), 605–618. https://doi.org/10.4252/wjsc.v13.i6.605.

(354) Khaw, J. S.; Xue, R.; Cassidy, N. J.; Cartmell, S. H. Electrical Stimulation of Titanium to Promote Stem Cell Orientation, Elongation and Osteogenesis. *Acta Biomater.* **2022**, *139*, 204–217. https://doi.org/10.1016/j.actbio.2021.08.010.

(355) Liu, N.; Zhou, M.; Zhang, Q.; Yong, L.; Zhang, T.; Tian, T.; Ma, Q.; Lin, S.; Zhu, B.; Cai, X. Effect of Substrate Stiffness on Proliferation and Differentiation of Periodontal Ligament Stem Cells. *Cell Prolif.* **2018**, *51* (5), e12478. https://doi.org/10.1111/cpr.12478.

Supplementary Data

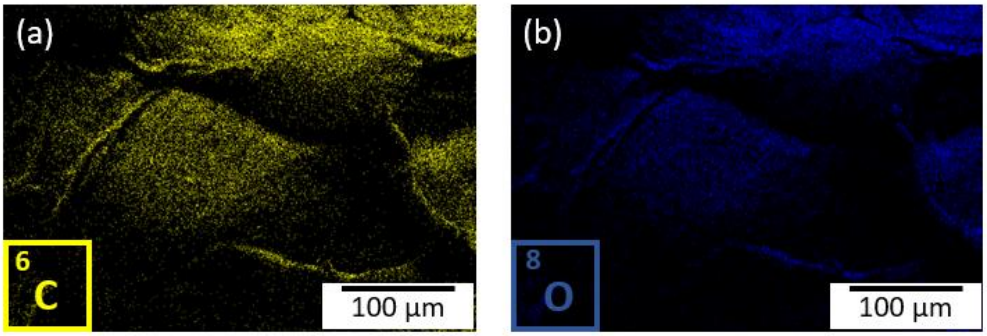

Figure S1: Complementary EDS analysis. Corresponding EDS maps of C **(a)** and O **(b)**

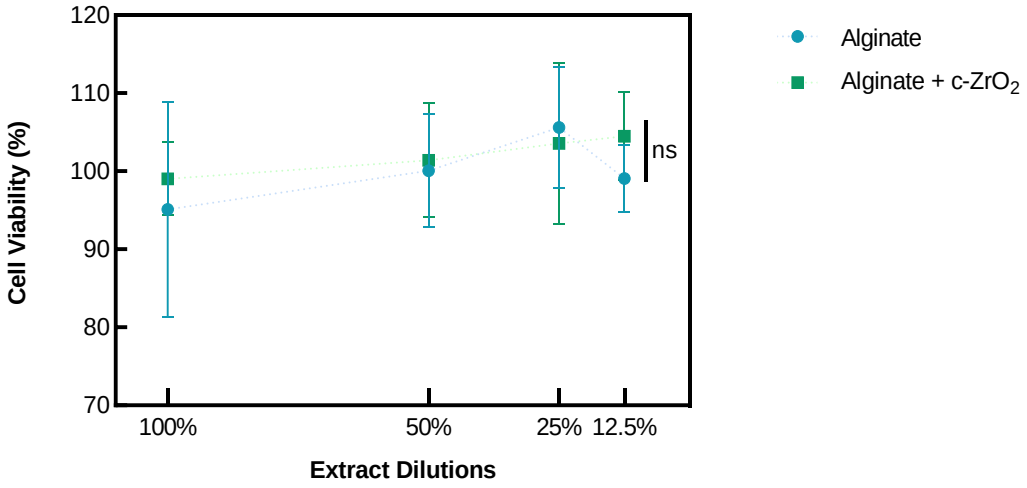

Figure S2: Cell viability determination using the MTT assay on alginate scaffolds with and without c-ZrO_2 nanoparticles, after 24 hours for all-extract dilutions. Two-way ANOVA test, (ns) not significant. All data presented as plot individual values, mean ± SD (N=3).

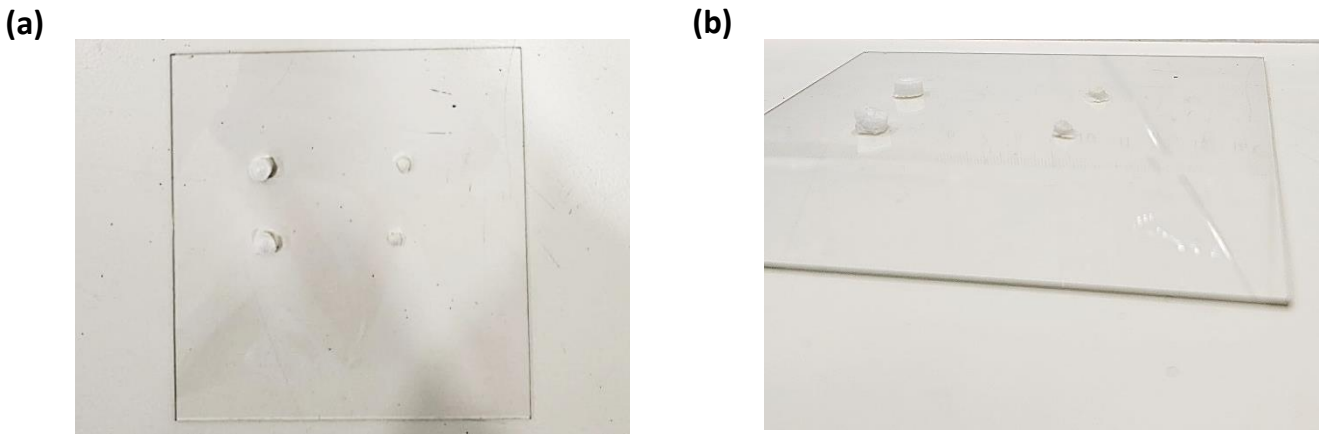

Figure S3: Scaffolds' dimensions for the Almar Blue assay. **(a)** View from Above. The samples on the right represent the alginate scaffolds, while those on the left show the alginate scaffolds after the incorporation of the nanoparticles. **(b)** Side perspective. Similarly, the samples on the right represent the alginate scaffolds, while those on the left show the alginate scaffolds after the incorporation of the nanoparticles.

Table S1: Scaffolds' dimensions for the Alamar Blue assay. All data are presented as mean ± SD. (N=3)

	Alginate	**Alginate+ c-ZrO_2**
Diameter (cm)	0.64 ± 0.03	0.37 ± 0.02
Height (cm)	0.35 ± 0.03	0.17 ± 0.03
Cross-sectional area (cm^2)	0.32 ± 0.03	0.11 ± 0.01
Volume (cm^3)	0.11 ± 0.01	0.02 ± 0.01